
HOMO RES SACRA

ՀԱՅ-ՌՈՒՍԱԿԱՆ ՀԱՄԱԼՍԱՐԱՆ

ԼՐԱԲԵՐ

ՀԱՅ-ՌՈՒՍԱԿԱՆ ՀԱՄԱԼՍԱՐԱՆԻ

ՍԵՐԻԱ

ՖԻԶԻԿԱՄԱԹԵՄԱՏԻԿԱԿԱՆ
ԵՎ ԲՆԱԿԱՆ ԳԻՏՈՒԹՅՈՒՆՆԵՐ

№ 1

ՀՌՀ Հրատարակչություն

Երևան 2020

РОССИЙСКО-АРМЯНСКИЙ УНИВЕРСИТЕТ

В Е С Т Н И К

РОССИЙСКО-АРМЯНСКОГО УНИВЕРСИТЕТА

СЕРИЯ:

ФИЗИКО-МАТЕМАТИЧЕСКИЕ И ЕСТЕСТВЕННЫЕ НАУКИ

№ 1

Издательство РАУ

Ереван 2020

Печатается по решению Ученого совета РАУ

Вестник РАУ, № 1. – Ер.: Изд-во РАУ, 2020. – 116 с.

Журнал входит в перечень периодических изданий,
зарегистрированных ВАК РА и РИНЦ

Российско-Армянский университет, 2020 г.

ISBN 1829-0450

МАТЕМАТИКА И ИНФОРМАТИКА

УДК 514.7

Поступила: 13.11.2019г.
Сдана на рецензию: 19.11.2019г.
Подписана к печати: 27.02.2020г.

ON THE RADIUS OF A CLOSED BALL INCLUDED IN THE MULTIBROTAND MULTICORN SETS

D. Dumitru, G. Dallakyan

Spiru Haret University of Bucharest, Russian-Armenian University

dandumitru2011@gmail.com, dallakyangurgen@gmail.com

ABSTRACT

The aim of this article is to compute a radius of a closed ball included in the multibrot and multicorn sets. Considering$w \in \mathbb{C}$ as a solution of the equation $z^{k-1} = -1$, we compute a radius $r > 0$ such that $\bar{B}(w, r) = \{z \in \mathbb{C} \mid |z - w| \leq r\}$ is included in the multibrot sets$\mathcal{M}_k$ for every $k \geq 2$. Considering$w \in \mathbb{C}$ as a solution of the equation $z^{k+1} = -1$, we compute a radius $r > 0$ such that $\bar{B}(w, r)$ is included in the multicorn sets$\mathcal{M}_k^*$for every $k \geq 2$.

Keywords: mandelbrot set, multibrot set, multicorn set.

1. Introduction

Generalizations of the classical Mandelbrot set to multibrot and multicorn sets can be found in ([2], [3], [4]). The intersections of a multibrot set $\mathcal{M}_k$ with the rays of the form $\mathbb{R}^+ w$, where$w^{k-1} = 1$ or $w^{k-1} = -1$ with

$k \geq 2$ were computed in [1]. The intersections of the multibrot sets with the real axis were established in [2] and [4]. Similarly, the intersections of a multicorn set $\mathcal{M}_k^*$ with the rays of the form $\mathbb{R}^+ w$, where $w^{k+1} = 1$ or $w^{k+1} = -1$ with $k \geq 2$ were computed in [6]. Also in [6] there were established the intersections with the real axis of a multicorn set.

We have the following well-known definitions.

Definition 1.1. Let $g_k: \mathbb{C} \longrightarrow \mathbb{C}$ be the polynomial defined by $g_k(z) = z^k + c$ with $c \in \mathbb{C}$ and $k \in \mathbb{N}$, $k \geq 2$. The *multibrot set* is defined by

$$\mathcal{M}_k = \left\{c \in \mathbb{C} \mid \left(g_k^{(n)}(0)\right)_{n\geq 1} \text{ is bounded}\right\},$$

where $g_k^{(1)}(x) = g_k(x)$ and $g_k^{(n)}(x) = g_k^{(n-1)}\left(g_k(x)\right)$ is the n-th iterate of the function g_k. Moreover, if we consider the sequence of complex numbers $(Q_n)_{n\geq 1}$ satisfying the reccurence $Q_{n+1} = Q_n^k + c$ for every $n \geq 1$ with $Q_1 = c$, then the multibrot set can also be given by

$$\mathcal{M}_k = \{c \in \mathbb{C} \mid (Q_n)_{n\geq 1} \text{is bounded}\}.$$

For $k = 2$ we have a *Mandelbrot* set.

Definition 1.2. Let $h_k: \mathbb{C} \longrightarrow \mathbb{C}$ be the polynomial defined by $h_k(z) = \bar{z}^k + c$ with $c \in \mathbb{C}$ and $k \in \mathbb{N}$, $k \geq 2$. The *multicorn set* is defined by

$$\mathcal{M}_k^* = \left\{c \in \mathbb{C} \mid \left(h_k^{(n)}(0)\right)_{n\geq 1} \text{ is bounded}\right\},$$

where $h_k^{(1)}(x) = h_k(x)$ and $h_k^{(n)}(x) = h_k^{(n-1)}\left(h_k(x)\right)$ is the n-th iterate of the function h_k.

We make the following notations: $\alpha_k = \begin{cases} \frac{1}{4} & \text{, for } k = 2 \\ \frac{k-1}{k\left(\sqrt[k-1]{k}\right)} & \text{, for } k \geq 3 \end{cases}$,

$\beta_k = \begin{cases} 2 & \text{, for } k = 2 \\ \sqrt[k-1]{2} & \text{, for } k \geq 3 \end{cases}$ and $\gamma_k = \frac{1}{k\left(\sqrt[k-1]{k}\right)}[\sinh(k\xi_k) + k\sinh(\xi_k)]$

where ξ_k is the unique positive root of the equation $\cosh(k\xi_k) = k\cosh(\xi_k)$ for every $k \geq 3$ (in particular $\gamma_3 = \sqrt{\frac{32}{27}} \cong 1.088$). Moreover, if we consider w a solution of one of the equations $z^{k\pm 1} = \pm 1$, then we denote

by $\mathbb{R}^+ w = \{tw \mid 0 \le t < w\}$ an axis that passes through the origin and has the direction of w.

The following results are known:

Theorem 1.1. *([2], [3], [4]) Let $\mathcal{M}_k$ be the multibrot set for every $k \ge 2$.*

a). If w is a solution of the equation $z^{k-1} = 1$, then $\mathcal{M}_k \cap \mathbb{R}^+ w = \{tw \mid 0 \le t \le \alpha_k\}$ for every $k \ge 2$.

b). If w is a solutionof the equation $z^{k-1} = -1$ and k is even, then $\mathcal{M}_k \cap \mathbb{R}^+ w = \{tw \mid 0 \le t \le \beta_k\}$ for every $k \ge 2$.

Theorem 1.2. *([1]) Let $\mathcal{M}_k$ be the multibrot set for every $k \ge 3$.If w is a solution of the equation $z^{k-1} = -1$ and k is odd, then $\mathcal{M}_k \cap \mathbb{R}^+ w = \{tw \mid 0 \le t \le \gamma_k\}$ for every $k \ge 3$.*

Theorem 1.3. *([6]) Let $\mathcal{M}_k^*$ be the multicorn set for every $k \ge 2$.*

a). If w is a solution of the equation $z^{k+1} = 1$, then $\mathcal{M}_k^* \cap \mathbb{R}^+ w = \{tw \mid 0 \le t \le \alpha_k\}$ for every $k \ge 2$.

b). If w is a solutionof the equation $z^{k+1} = -1$ and k is even, then $\mathcal{M}_k^* \cap \mathbb{R}^+ w = \{tw \mid 0 \le t \le \beta_k\}$ for every $k \ge 2$.

c). For every $k \ge 3$, if w is a solution of the equation $z^{k+1} = -1$ and k is odd, then $\mathcal{M}_k^* \cap \mathbb{R}^+ w = \{tw \mid 0 \le t \le \gamma_k\}$.

2. Main results

A. Preliminary lemmas

In this section we will prove some preliminary lemmas.

Lemma 2.1. *Let $k \ge 4$and the recurrence $Q_{n+1} = Q_n^k + c$ for every $n \ge 1$ where $Q_1 = c$. We suppose that $|c - w| \le \alpha$ with $\alpha \in (0,1)$ where w is a solution of the equation $z^{k-1} = -1$. Then $|Q_2| \le (\alpha + 1)^k - (\alpha + 1)$.*

Proof: From the hypothesis we obtain that $|c| \le \alpha + 1$and we consider w a solution of the equation $z^{k-1} = -1$. Then we have

$$|Q_2| = \left|Q_1^k + c\right| = |c^k + c| = |c||c^{k-1} + 1| = |c||c^{k-1} - w^{k-1}| =$$
$$|c||(c-w)(c^{k-2} + c^{k-3}w + \cdots + cw^{k-3} + w^{k-2})| =$$
$$|c||c-w||c^{k-2} + c^{k-3}w + \cdots + cw^{k-3} + w^{k-2}| \leq$$
$$\leq |c||c-w|(|c|^{k-2} + |c|^{k-1} + \cdots + |c| + 1)$$
$$\leq (\alpha+1)\alpha[(\alpha+1)^{k-2} + \cdots + (\alpha+1) + 1] =$$
$$= (\alpha+1)\alpha\frac{(\alpha+1)^{k-1} - 1}{(\alpha+1) - 1} = (\alpha+1)^k - (\alpha+1)$$

Lemma 2.2. *Let the conditions of Lemma 2.1 be fulfilled. If there exists* $R > 1$ *such that* $|Q_2| \leq (\alpha+1)^k - (\alpha+1) < \frac{1}{R}$*, then*

a). $|Q_4| \leq \left(\alpha + 1 + \frac{1}{R^k}\right)^k - (\alpha+1)$

b). If $|Q_4| \leq \left(\alpha + 1 + \frac{1}{R^k}\right)^k - (\alpha+1) < \frac{1}{R}$ *then* $|Q_{2n}| \leq \left(\alpha + 1 + \frac{1}{R^k}\right)^k - (\alpha+1) < \frac{1}{R}$ *for every* $n \geq 2$.

Proof: a). Denote by $Q_2^k = q \in \mathbb{C}$. From conditions of lemma we have $|c| \leq \alpha + 1$ and $|Q_2| = \left|Q_1^k + c\right| = \left|c^k + c\right| \leq (\alpha+1)^k - (\alpha+1) < \frac{1}{R}$. Therefore $|q| < \frac{1}{R^k}$ and

$$|Q_4| = \left|Q_3^k + c\right| = \left|\left(Q_2^k + c\right)^k + c\right| =$$
$$= |(q+c)^k + c| = |(q+c)^k - c^k + c^k + c|$$
$$\leq |(q+c)^k - c^k| + |c^k + c| =$$
$$= \left|q[(q+c)^{k-1} + (q+c)^{k-2}c + \cdots + (q+c)c^{k-2} + c^{k-1}]\right| + \left|c^k + c\right| \leq$$
$$\leq |q|[(|q| + |c|)^{k-1} + (|q| + |c|)^{k-2}|c| + \cdots + (|q| + |c|)|c|^{k-2}$$
$$+ |c|^{k-1}] + |c^k + c| <$$
$$\frac{1}{R^k}\left[\left(\frac{1}{R^k} + \alpha + 1\right)^{k-1} + \left(\frac{1}{R^k} + \alpha + 1\right)^{k-2}(\alpha+1) + \cdots + (\alpha+1)^{k-1}\right]$$
$$+ (\alpha+1)^k - (\alpha+1) =$$
$$= \left(\alpha + 1 + \frac{1}{R^k}\right)^k - (\alpha+1)$$

b). Let $|Q_4| \leq \left(\alpha + 1 + \frac{1}{R^k}\right)^k - (\alpha + 1) < \frac{1}{R}$ is true by the assumption. Suppose also that $|Q_{2n}| \leq \left(\alpha + 1 + \frac{1}{R^k}\right)^k - (\alpha + 1) < \frac{1}{R}$. We shall prove that $|Q_{2n+2}| \leq \left(\alpha + 1 + \frac{1}{R^k}\right)^k - (\alpha + 1) < \frac{1}{R}$. Denote by $Q_{2n}^k = p \in \mathbb{C}$. Since $|Q_{2n+2}| = \left|Q_{2n+1}^k + c\right| = \left|\left(Q_{2n}^k + c\right)^k + c\right| = |(p + c)^k + c|$ so by analogous to the point a), taking in account that $|q| < \frac{1}{R^k}$ we obtain $|Q_{2n+2}| < \left(\alpha + 1 + \frac{1}{R^k}\right)^k - (\alpha + 1) < \frac{1}{R}$. Thus by mathematical induction we have that $|Q_{2n}| \leq \left(\alpha + 1 + \frac{1}{R^k}\right)^k - (\alpha + 1) < \frac{1}{R}$ for every $n \geq 2$.

Lemma 2.3. *Let $k \geq 4$ and the recurrence $R_{n+1} = \bar{R}_n^k + c$ holds for every $n \geq 1$ where $R_1 = c$. We suppose that $|c - w| \leq \alpha$ with $\alpha \in (0,1)$ where w is a solution of the equation $z^{k+1} = -1$. Then $|R_2| \leq (\alpha + 1)^k + \alpha - 1$.*

Proof: i). Let $k = 2p + 1 \geq 4$ and $t := w^{2p} \in \mathbb{C}$, where w is a solution of the equation $z^{k+1} = -1$. Then $t = -\frac{1}{w} = -\frac{\bar{w}}{\bar{w}w} = -\bar{w}$ and $t^{2p} = \left(-\frac{1}{w}\right)^{2p} = -w$. Let $|c - w| \leq \alpha$ for $\alpha \in (0,1)$. Therefore $|c + t^{2p}| = |c - w| = |\bar{c} - \bar{w}| = |\bar{c} + t| \leq \alpha$. Hence, taking into consideration lemma 2.2, we obtain the following:

$$|R_2| = \left|\bar{R}_1^k + c\right| = |\bar{c}^{2p} + c| =$$

$$\left|(\bar{c} + t)^{2p} - C_{2p}^1 t(\bar{c} + t)^{2p-1} + C_{2p}^2 t^2(\bar{c} + t)^{2p-2} - \cdots \right.$$

$$\left. - C_{2p}^{2p-1} t^{2p-1}(\bar{c} + t) + t^{2p} + c\right| \leq$$

$$|\bar{c} + t|^{2p} + C_{2p}^1|\bar{c} + t|^{2p-1} + \cdots + C_{2p}^{2p-1}|\bar{c} + t| + |c + t^{2p}| \leq$$

$$\alpha^{2p} + C_{2p}^1\alpha^{2p-1} + \cdots + C_{2p}^{2p-1}\alpha + \alpha = (\alpha + 1)^{2p} + \alpha - 1$$

$$= (\alpha + 1)^k + \alpha - 1$$

ii). Let $k = 2p \geq 4$, w a solution of the equation $z^{k+1} = z^{2p+2} = -1$ and $|c - w| \leq \alpha$ with $\alpha \in (0,1)$. We denote by $t = w^{2p+1} \in \mathbb{C}$. Then $|c| \leq \alpha + 1$, $|w| = |t| = 1, w^{2p+1} = -\bar{w}, t^{2p+1} = (w^{2p+1})^{2p+1} =$

$\left(-\frac{1}{w}\right)^{2p+1} = -\frac{1}{w^{2p+1}} = w$, so $\overline{c-w} = \bar{c} - \bar{w} = \bar{c} - (-t) = \bar{c} + t$ and thus $|c - t^{2p+1}| = |c - w| = |\bar{c} - \bar{w}| = |\bar{c} + t| \leq \alpha$. Hence, taking into consideration lemma 2.3, we obtain the following:

$$|R_2| = \left|\bar{R}_1^k + c\right| = |\bar{c}^{2p+1} + c| =$$
$$\left|(\bar{c}+t)^{2p+1} - C_{2p+1}^1 t(\bar{c}+t)^{2p} + C_{2p+1}^2 t^2(\bar{c}+t)^{2p-1} - \cdots\right.$$
$$\left. + C_{2p+1}^{2p} t^{2p}(\bar{c}+t) - t^{2p+1} + c\right| \leq$$
$$|\bar{c}+t|^{2p+1} + C_{2p+1}^1|\bar{c}+t|^{2p} + \cdots + C_{2p+1}^{2p}|\bar{c}+t| + |c - t^{2p+1}| \leq$$
$$\alpha^{2p+1} + C_{2p+1}^1\alpha^{2p} + \cdots + C_{2p+1}^{2p}\alpha + \alpha = (\alpha+1)^{2p+1} + \alpha - 1$$
$$= (\alpha+1)^k + \alpha - 1$$

Hence we conclude that if w is a solution of the equation $z^{k+1} = -1$ and $|c - w| \leq \alpha \in (0,1)$ then $|R_2| \leq (\alpha+1)^k + \alpha - 1$ for every $k \geq 4$.

Lemma 2.4. *Let $k \geq 4$ and the recurrence $R_{n+1} = \overline{R_n}^k + c$ holds for every $n \geq 1$ where $R_1 = c$. We suppose that $|c - w| \leq \alpha$ with $\alpha \in (0,1)$ where w is a solution of the equation $z^{k+1} = -1$. If there exists $R > 1$ such that $|R_2| \leq (\alpha+1)^k + \alpha - 1 < \frac{1}{R}$, then*

a). $|R_4| \leq \left(\alpha + 1 + \frac{1}{R^k}\right)^k + \alpha - 1$

b). If $|R_4| \leq \left(\alpha + 1 + \frac{1}{R^k}\right)^k + \alpha - 1 < \frac{1}{R}$ then $|R_{2n}| \leq \left(\alpha + 1 + \frac{1}{R^k}\right)^k + \alpha - 1 < \frac{1}{R}$ for every $n \geq 2$.

Proof: a). From conditions of lemma we have $|R_2| = \left|\overline{R_1}^k + c\right| = |\bar{c}^k + c| \leq (\alpha+1)^k + \alpha - 1 < \frac{1}{R}$. Denote by $R_2^k = r$. From here we have

$$|R_4| = \left|\overline{R_3}^k + c\right| = \left|\left(R_2^k + \bar{c}\right)^k + c\right| =$$
$$= |(r+\bar{c})^k + c| \leq |(r+\bar{c})^k - \bar{c}^k| + |\bar{c}^k + c| =$$
$$=|r[(r+\bar{c})^{k-1} + (r+\bar{c})^{k-2}\bar{c} + \cdots + (r+\bar{c})\bar{c}^{k-2} + \bar{c}^{k-1}]| + |\bar{c}^k + c| \leq$$
$$\leq |r|[(|r|+|\bar{c}|)^{k-1} + (|r|+|\bar{c}|)^{k-2}|\bar{c}| + \cdots + (|r|+|\bar{c}|)|\bar{c}|^{k-2}$$
$$+ |\bar{c}|^{k-1}] + |\bar{c}^k + c| <$$

$$\frac{1}{R^k}\left[\left(\frac{1}{R^k}+\alpha+1\right)^{k-1}+\left(\frac{1}{R^k}+\alpha+1\right)^{k-2}(\alpha+1)+\cdots+(\alpha+1)^{k-1}\right]$$
$$+(\alpha+1)^k-(\alpha+1)=$$
$$=\left(\alpha+1+\frac{1}{R^k}\right)^k-(\alpha+1)$$

b). For $n=2$ we have $|R_4|\leq\left(\alpha+1+\frac{1}{R^k}\right)^k+\alpha-1<\frac{1}{R}$. We suppose now that $|R_{2n}|\leq\left(\alpha+1+\frac{1}{R^k}\right)^k+\alpha-1<\frac{1}{R}$ and we prove that $|R_{2n+2}|\leq\left(\alpha+1+\frac{1}{R^k}\right)^k+\alpha-1<\frac{1}{R}$. Denote by $R_{2n}^k=r$. We have $|R_{2n+2}|=\left|\overline{R_{2n+1}}^k+c\right|=\left|\left(R_{2n}^k+\bar{c}\right)^k+c\right|=|(r+\bar{c})^k+c|$.

Conducting similar reasoning, we obtain $|R_{2n+2}|<\left(\alpha+1+\frac{1}{R^k}\right)^k+\alpha-1<\frac{1}{R}$. Thus by mathematical induction we have that $|R_{2n}|\leq\left(\alpha+1+\frac{1}{R^k}\right)^k+\alpha-1<\frac{1}{R}$ for every $n\geq 2$.

B. Applications to multibrot and multicorn sets

Theorem 2.1. *Let $\mathcal{M}_k$ be the multibrot set for every $k\geq 2$. Then:*

a). $\bar{B}\left(-1,\frac{1}{10}\right)\subset\mathcal{M}_2$.

b). $\bar{B}\left(w,\frac{1}{12}\right)\subset\mathcal{M}_3$ where w is a solution of the equation $z^2=-1$.

c). $\bar{B}\left(w,\frac{1}{5k}\right)\subset\mathcal{M}_k$ where w is a solution of the equation $z^{k-1}=-1$ for every $k\geq 4$.

Proof: For this proof we will use the recurrence $Q_{n+1}=Q_n^k+c$ for every $n\geq 1$ where $Q_1=c$ and $k\geq 2$.

a). For $k=2$ we have $Q_{n+1}=Q_n^2+c$ for every $n\geq 1$ where $Q_1=c$ and let $w=-1$. For $|c-w|=|c+1|\leq\frac{1}{10}$ we have $|Q_1|=|c|\leq\frac{11}{10}$. Thus we obtain

$$|Q_2| = |Q_1^2 + c| = |c^2 + c| = |c(c+1)| = |c||c+1| \leq \left(\frac{1}{10}\right)\left(\frac{11}{10}\right)$$
$$= \frac{11}{100} = 0.11 < 0.2 = \frac{1}{5}$$

Moreover

$$|Q_4| = |(Q_2^2 + c)^2 + c| = |Q_2^4 + 2cQ_2^2 + c^2 + c| \leq$$
$$|Q_2|^4 + 2|c||Q_2|^2 + |c^2 + c| < \left(\frac{1}{5}\right)^4 + 2\left(\frac{11}{10}\right)\left(\frac{1}{5}\right)^2 + \frac{11}{100} \cong 0.1996$$
$$< 0.2 = \frac{1}{5}$$

Hence by lemma 2.2, point b), we have $|Q_{2n}| < \frac{1}{5}$ for every $n \geq 1$ and thus $Q_n \nrightarrow \infty$ when $n \longrightarrow \infty$. So we obtain that $\bar{B}\left(-1, \frac{1}{10}\right) \subset \mathcal{M}_2$.

b). For $k = 3$ we have $Q_{n+1} = Q_n^3 + c$ for every $n \geq 1$ where $Q_1 = c$ and let $w^2 = -1$ which implies $w \in \{i, -i\}$. Let $w = -i$ and consider $|c - w| = |c + i| \leq \frac{1}{12}$.Then we have $|Q_1| = |c| \leq \frac{13}{12}$and thus

$$|Q_2| = |Q_1^3 + c| = |c^3 + c| = |c(c^2 + 1)| \leq |c[(c+i)^2 - 2i(c+i)]| =$$
$$|c||(c+i)^2 - 2i(c+i)| \leq |c|(|c+i|^2 + 2|c+i|) \leq$$
$$\left(\frac{13}{12}\right)\left[\frac{1}{144} + 2\left(\frac{1}{12}\right)\right] = \frac{325}{1728} \cong 0.1880 < 0.25 = \frac{1}{4}$$

Moreover

$$|Q_4| = |(Q_2^3 + c)^3 + c| = |Q_2^9 + 3cQ_2^6 + 3c^2Q_2^3 + c^3 + c| \leq$$
$$|Q_2|^9 + 3|c||Q_2|^6 + 3|c|^2|Q_2|^3 + |c^3 + c| <$$
$$\left(\frac{1}{4}\right)^9 + 3\left(\frac{13}{12}\right)\left(\frac{1}{4}\right)^6 + 3\left(\frac{13}{12}\right)^2\left(\frac{1}{4}\right)^4 + \frac{325}{1728} \cong 0.2436 < 0.25 = \frac{1}{4}$$

Hence by lemma 2.2, point b), we have $|Q_{2n}| < \frac{1}{4}$ for every $n \geq 1$ and thus $Q_n \nrightarrow \infty$ when $n \longrightarrow \infty$. Thus $\bar{B}\left(-i, \frac{1}{12}\right) \subset \mathcal{M}_3$. There is similar proof for $w = i$. Hence $\bar{B}\left(w, \frac{1}{12}\right) \subset \mathcal{M}_3$ where w is a solution of the equation $z^2 = -1$.

c). Let $k \geq 4$ and we make first the following remarks:

i). For $R > 1.25$ the sequence $(\varepsilon_k)_{k\geq 4}$ where $\varepsilon_k = \frac{k}{R^k}$ for every $k \geq 4$ is decreasing. (Indeed, we have that $\frac{\varepsilon_{k+1}}{\varepsilon_k} = \left(\frac{k+1}{R^{k+1}}\right)\left(\frac{R^k}{k}\right) = \frac{k+1}{kR} < 1 \Leftrightarrow k + 1 < Rk \Leftrightarrow 1 < k(R-1)$ which is true for $R > 1.25$ and $k \geq 4$. Hence we obtain that $0 < \varepsilon_k \leq \varepsilon_4 = \frac{4}{\mathrm{R}^4}$ for every $k \geq 4$).

ii). According to ([5]), for every $r > 0$ and $x > -1$ we have a generalized version of Bernoulli's inequality that is

$$1 + rx \leq (1+x)^r \leq e^{rx}.$$

We return to our proof.Suppose now that w is a solution of the equation $z^{k-1} = -1$ and $|c - w| \leq \frac{1}{5k} = \alpha$. Then from lemma 2.1 we have

$$|Q_2| \leq (\alpha+1)^k - (\alpha+1) \leq e^{k\alpha} - (\alpha+1) = e^{1/5} - (\alpha+1)$$

$$< e^{1/5} - 1 \cong 0.2214 < \frac{1}{4} = \frac{1}{\mathbf{R}}$$

Thus we obtain $\mathbf{R} = 4$ and the sequence $\varepsilon_k = \frac{k}{4^k}$ for every $k \geq 4$ verifies $0 < \varepsilon_k \leq \varepsilon_4 = \frac{1}{64}$. Then from lemma 2.2. we have

$$|Q_4| \leq \left(\frac{1}{4^k} + \alpha + 1\right)^k - (\alpha+1) \leq e^{k\left(\alpha + \frac{1}{4^k}\right)} - (\alpha+1)$$

$$= e^{k\left(\frac{1}{5k} + \frac{1}{4^k}\right)} - (\alpha+1) =$$

$$e^{\left(\frac{1}{5} + \frac{k}{4^k}\right)} - (\alpha+1) < e^{\left(\frac{1}{5} + \frac{4}{4^4}\right)} - (\alpha+1) < e^{\left(\frac{1}{5} + \frac{1}{64}\right)} - 1 \cong 0.2400 < 0.25$$

$$= \frac{1}{4} = \frac{1}{\mathbf{R}}$$

Hence by lemma 2.2, point b), we have that $|Q_{2n}| < \frac{1}{4}$ for every $n \geq 1$ and thus $Q_n \nrightarrow \infty$ when $n \longrightarrow \infty$. Thus $\bar{B}\left(w, \frac{1}{5k}\right) \subset \mathcal{M}_k$ where w is a solution of the equation $z^{k-1} = -1$ for every $k \geq 4$.

Theorem 2.2. *Let $\mathcal{M}_k^*$be the multicorn set for every $k \geq 2$. Then:*

a). $\bar{B}\left(w, \frac{1}{27}\right) \subset \mathcal{M}_2^*$where w is a solution of the equation $z^3 = -1$.

b). $\bar{B}\left(w, \frac{1}{23}\right) \subset \mathcal{M}_3^*$where w is a solution of the equation $z^4 = -1$.

c). $\bar{B}\left(w,\frac{1}{6k}\right) \subset \mathcal{M}_k^*$ where w is a solution of the equation $z^{k+1} = -1$ for every $k \geq 4$.

Proof: For this proof we will use the recurrence $R_{n+1} = \overline{R_n}^k + c$ for every $n \geq 1$ where $R_1 = c$ and $k \geq 2$.

a). For $k = 2$ we have $R_{n+1} = \overline{R_n}^2 + c$ for every $n \geq 1$ where $R_1 = c$.Suppose that w is a solution of the equation $z^3 = -1$and$|c - w| \leq \frac{1}{27}$. Then$|R_1| = |c| \leq \frac{28}{27}$. Thus we obtain

$$|R_2| = \left|\overline{R_1}^2 + c\right| = |\bar{c}^2 + c| = |(\bar{c} + w)^2 - 2w^2(\bar{c} + w^2) + w^2 + c| =$$
$$|(\bar{c} + w)^2 - 2w^2(\bar{c} + w^2) + c - w| \leq |\bar{c} + w^2|^2 + 2|\bar{c} + w^2| + |c - w|$$
$$\leq$$
$$\left(\frac{1}{27}\right)^3 + 3\left(\frac{1}{27}\right) = \frac{2188}{19683} = 0.1111 < 0.2 = \frac{1}{5}$$

Moreover

$$|R_4| = \left|\overline{R_3}^2 + c\right| = |(R_2^2 + \bar{c})^2 + c| = |R_2^4 + 2\bar{c}R_2^2 + \bar{c}^2 + c| \leq$$
$$|R_2|^4 + 2|\bar{c}||R_2|^2 + |\bar{c}^2 + c| \leq \left(\frac{1}{5}\right)^4 + 2\left(\frac{28}{27}\right)\left(\frac{1}{5}\right)^2 + \frac{2188}{19683} \cong 0.1970$$
$$< 0.2 = \frac{1}{5}$$

Hence by lemma 2.5, point b), we have $|R_{2n}| < \frac{1}{5}$ for every $n \geq 1$ and thus $R_n \nrightarrow \infty$ when $n \longrightarrow \infty$. So we obtain that $\bar{B}\left(w,\frac{1}{27}\right) \subset \mathcal{M}_2^*$ where w is a solution of the equation $z^3 = -1$.

b). For $k = 3$ we have $R_{n+1} = \overline{R_n}^3 + c$ for every $n \geq 1$ where $R_1 = c$. Suppose that w is a solution of the equation $z^4 = -1$ and $|c - w| \leq \frac{1}{23}$. Then $|R_1| = |c| \leq \frac{24}{23}$ and $|\bar{c} + w^3| \leq \frac{1}{23}$. Thus we obtain

$$|R_2| = \left|\overline{R_1}^3 + c\right| = |\bar{c}^3 + c|$$
$$= |(\bar{c} + w^3)^3 - 3w^3(\bar{c} + w^3)^2 + 3w^6(\bar{c} + w^3) - w + c| \leq$$
$$|\bar{c} + w^3|^3 + 3|\bar{c} + w^3|^2 + 3|\bar{c} + w^3| + |c - w| \leq$$

$$\left(\frac{1}{23}\right)^3+3\left(\frac{1}{23}\right)^2+4\left(\frac{1}{23}\right)=\frac{2186}{12167}\cong 0.1796<\frac{1}{4}$$

Moreover

$$|R_4|=\left|\overline{R_3}^3+c\right|=|(R_2^2+\bar{c})^3+c|=|R_2^9+3\bar{c}R_2^6+3\bar{c}^2R_2^3+\bar{c}^3+c|\leq$$

$$|R_2|^9+3|\bar{c}||R_2|^6+3|\bar{c}|^2|R_2|^3+|\bar{c}^3+c|\leq$$

$$\left(\frac{1}{4}\right)^9+3\left(\frac{24}{23}\right)\left(\frac{1}{4}\right)^6+3\left(\frac{24}{23}\right)^2\left(\frac{1}{4}\right)^3+\frac{2186}{12167}\cong 0.2314<0.25=\frac{1}{4}$$

Hence by lemma 2.5, point b), we have $|R_{2n}|<\frac{1}{4}$ for every $n\geq 1$ and thus $R_n \nrightarrow \infty$ when $n\longrightarrow\infty$. Thus $\bar{B}\left(w,\frac{1}{23}\right)\subset\mathcal{M}_3^*$where w is a solution of the equation $z^4=-1$.

c). Let $k\geq 4$ and for the sake of the completion of the paper we remindthe following remarks similar to point c) of theorem 2.1:

i). For $R>1.25$ the sequence $(\varepsilon_k)_{k\geq 4}$ where $\varepsilon_k=\frac{k}{R^k}$ for every $k\geq 4$ is decreasing.

ii). According to ([5]), for every $r>0$ and $x>-1$ we have a generalized version of Bernoulli's inequality that is $1+rx\leq(1+x)^r\leq e^{rx}$.

We return to our proof. Suppose now that w is a solution of the equation $z^{k+1}=-1$ and $|c-w|\leq\frac{1}{6k}=\alpha$. Then from lemma 2.4 we have

$$|R_2|\leq(\alpha+1)^k+\alpha-1\leq e^{k\alpha}+\alpha-1=e^{1/6}+\frac{1}{6k}-1$$

$$<e^{1/6}+\frac{1}{24}-1\cong 0.2230<\frac{1}{4}$$

Thus we obtain $R=4$ and the sequence $\varepsilon_k=\frac{k}{4^k}$ for every $k\geq 4$ verifies $0<\varepsilon_k\leq\varepsilon_4=\frac{1}{64}$. Then from lemma 2.5. we have

$$|R_4|\leq\left(\frac{1}{4^k}+\alpha+1\right)^k+\alpha-1\leq e^{k\left(\alpha+\frac{1}{4^k}\right)}+\alpha-1=e^{k\left(\frac{1}{6k}+\frac{1}{4^k}\right)}+\alpha-1$$

$$=$$

$$e^{\left(\frac{1}{6}+\frac{k}{4^k}\right)}+\frac{1}{6k}-1<e^{\left(\frac{1}{6}+\frac{4}{4^4}\right)}+\frac{1}{24}-1\cong 0.2416<0.25=\frac{1}{4}=\frac{1}{R}$$

Hence by lemma 2.5, point b), we have that $|R_{2n}| < \frac{1}{4}$ for every $n \geq 1$ and thus $R_n \nrightarrow \infty$ when $n \longrightarrow \infty$. Thus $\bar{B}\left(w, \frac{1}{6k}\right) \subset \mathcal{M}_k^*$ where w is a solution of the equation $z^{k+1} = -1$ for every $k \geq 4$.

REFERENCES

1. *Baribeau L., Ransford T.* Cross-sections of multibrot set, The Journal of Analysis, vol. 24, issue 1, June 2016, 95–101.
2. *Parisé P.O., Rochon D.* A study of dynamics of the tricomplex polynomial $\eta^p + c$, Nonlinear Dynamics, vol. 82, issue 1–2, October 2015, 157–171.
3. *Parisé P.O., Rochon D.* Tricomplex dynamical systems generated by polynomials of odd degree, Fractals, vol. 25, no. 3, 1750026, 2017.
4. *Parisé P.O., Ransford T., Rochon D.* Tricomplex dynamical systems generated by polynomials of even degree, Chaotic modeling and simulation (CMSIM), vol. 1, 37–48, 2017.
5. *Li Y.C., Yeh C.C.* Some equivalent forms of Bernoulli's inequality: a survey, Applied Mathematics, vol. 4, 1070–1093, 2013.
6. *Zhang X.* Cross-sections of the multicorns, Proceedings-Mathematical Sciences, Published by the Indian Academy of Science, April 2019, vol. 129, issue 2, Article ID 0028.

О РАДИУСЕ ЗАМКНУТОГО ШАРА, ВКЛЮЧЕННОГО В МНОГОБРОТНЫЕ И МНОГОКОРНЕВЫЕ МНОЖЕСТВА

Д. Думитру, Г. Даллакян

АННОТАЦИЯ

Целью данной статьи является вычисление радиуса замкнутого шара, включенного в многобротные и многокорневые множества. Рассматривая $w \in \mathbb{C}$ как решение уравнения $z^{k-1} = -1$, мы вычисляем радиус $r > 0$ такой, что $\bar{B}(w, r) = \{z \in \mathbb{C} \mid |z - w| \leq r\}$ содержится в многобротных множествах $\mathcal{M}_k$ для каждого $k \geq 2$. Рассматривая $w \in \mathbb{C}$ как решение уравнения $z^{k+1} = -1$, мы вычисляем радиус $r > 0$ такой, что $\bar{B}(w, r)$ содержится в многокорневых множествах $\mathcal{M}_k^*$ для каждого $k \geq 2$.

Ключевые слова: множество Мандельброта, многобротное множество, многокорневое множество.

УДК 512.6

Поступила: 09.03.2020г.
Сдана на рецензию: 16.03.2020г.
Подписана к печати: 15.04.2020г.

HYPERIDENTITIES WITH PERMUTATIONS LEADING TO THE LINEARITY OF INVERTIBLE BINARY ALGEBRAS

S. Davidov, D. Shahnazaryan

Department of Mechanics and Mathematics,
Yerevan State University

davidov@ysu.am, shahnazaryan94@gmail.com

ABSTRACT

In this paper, using the second-order formulas, we obtained characterizations of invertible binary algebras with different types of linearity. MSC2010: 03C85, 20N05, 20N99.

Keywords: invertible algebra, linear invertible algebra, second-order formula, hyperidentity, hyperidentity with permutations, isotopy.

1. Introduction

A binary algebra $(Q;\Sigma)$is called an invertible algebra or system of quasigroups if each operation in Σ is a quasigroup operation. Invertible algebras with second-order formulas were first considered by Shaufler [1] in connection with coding theory. He pointed out that the resulting message would be more difficult to decode by an unauthorized receiver than in the case when a single operation is used for calculation. Later such algebras

were investigated by J. Aczel [2], V. Belousov [3, 4], A. Sade [5], Yu. Movsisyan [6]–[10] and others.

It is well known [11] that with each quasigroup A the next five quasigroups are connected:

$$A^{-1}, \quad {}^{-1}A, \quad {}^{-1}(A^{-1}), (\quad {}^{-1}A)^{-1}, \ A^{*},$$

where $A^{*} \ (x,y) = A(y,x)$. These quasigroups are called inverse quasigroups or parastrophes. Like this, with each invertible algebra $(Q;\Sigma)$ the next five invertible algebras are connected:

$$(Q;\ \Sigma^{-1}), (Q;{}^{-1}\Sigma), (Q; \quad {}^{-1}(\Sigma^{-1})), (Q; (\quad {}^{-1}\Sigma)^{-1}), (Q;\ \Sigma^{*}),$$

where

$$\Sigma^{-1} = \{A^{-1} |\ A \in \Sigma\},$$
$${}^{-1}\Sigma = \{ \quad {}^{-1}A |\ A \in \Sigma\},$$
$${}^{-1}(\Sigma^{-1}) = \{ \quad {}^{-1}(A^{-1}) |\ A \in \Sigma\},$$
$$(\quad {}^{-1}\Sigma)^{-1} = \{(\quad {}^{-1}A)^{-1} |\ A \in \Sigma\},$$
$$\Sigma^{*} = \{ A^{*} |\ A \in \Sigma\}.$$

Each of these invertible algebras is called parastrophies of the algebra $(Q;\Sigma)$.

Let us recall that the following absolutely closed second-order formula:

$$\forall X_1,\ldots,X_m \forall x_1,\ldots,x_n \quad (\omega_1 = \omega_2),$$
$$\forall X_1,\ldots,X_k \exists X_{k+1},\ldots,X_m \forall x_1,\ldots,x_n \quad (\omega_1 = \omega_2),$$

where ω_1, ω_2 are words written in the functional variables, $X_1,\ldots,X_m$, and in the objective variables, $x_1,\ldots,x_n$, are called $\forall(\forall)$-identity or hyperidentity and $\forall\exists(\forall)$-identity. For details about such formulas see [7].

An important role in the theory of quasigroups is played by the concept of isotopy. The groupoid $Q(A)$ is called isotopic to the groupoid $Q(B)$ if there exist three maps α,β,γ of Q to Q such that

$\gamma B(x,y) = A(\alpha x,\beta y)$ for all $x,y \in Q$. The isotopy of the form $T = (\alpha,\beta,\epsilon)$, where ϵ is the identity map, is called principal isotopy.

Quasigroups isotopic to the groups or their different subclasses and identities generating them were studied by many authors. The concept of linear and left (right) linear quasigroups was introduced by Belousov in [4]. Later there were defined linear and left (right) linear invertible algebras, which were characterized by second-order formulas [12, 13, 8]. In the [14] they bring in the notion of identity with permutations, with which they characterize identities bringing to the isotopy of quasigroups to groups or linearity of the quasigroup. By analogy with [14] we introduced the notion of the hyperidentities with permutations at [15].

We will consider second-order formulas (calling them hyperidentities with permutations or hyperidentities in $(Q;\Sigma)$) of the following form:

$$\beta_1^{A,B} A(\beta_2^{A,B} B(\beta_3^{A,B} x, \beta_4^{A,B} y), \beta_5^{A,B} z) = B(\beta_6^{A,B} x, \beta_7^{A,B} A(\beta_8^{A,B} y, \beta_9^{A,B} z)),$$

where x,y,z are objective variables, $\beta_i^{A,B}$ (i = 1, ..., 9) are permutations on Q dependent on $A, B \in \Sigma$. By performance of parameter replacements those second-order formulas may be transformed to second-order formulas with less number of parameters:

$$\alpha_1^{A,B} A(\alpha_2^{A,B} B(x,y), z) = B(\alpha_3^{A,B} x, \alpha_4^{A,B} A(\alpha_5^{A,B} y, \alpha_6^{A,B} z)).$$

In this paper, we obtained characterizations of linear invertible algebras.

2. Auxiliary concepts and results

In this section we present some concepts and results, which are necessary for further considerations.

Definition 2.1. An invertible algebra $(Q;\Sigma)$ is called left (right) linear over a group $(Q;+)$, if every operation $A\in\Sigma$ has the form:

$$A(x,y) = \phi_A x + \beta_A y \quad (A(x,y) = \alpha_A x + \psi_A y),$$

where β_A (respectively α_A) is a permutation of the set Q, and ϕ_A (respectively is ψ_A) is an automorphism of the group $(Q;+)$.

An invertible algebra is called left (right) linear if it is left(right) linear over some group $(Q;+)$.

Definition 2.2. The triplet $T=(\alpha,\beta,\gamma)$ of permutations of the set Q is called an autotopy of the groupoid $Q(\cdot)$, if the following identity:

$$\gamma(x\cdot y) = \alpha x\cdot\beta y$$

is true for $\forall x,y\in Q$.

Consequently, the concept of autotopy is the particular case of the concept of isotopy. It is sufficient to state that $A=B$. If $T=(\alpha,\beta,\gamma)$ is an autotopy of the groupoid $Q(A)$, then we write $A^T=A$. In case if $\alpha=\beta=\gamma$, then the triplet $T=(\alpha,\alpha,\alpha)$ is an automorphism of the groupoid $Q(\cdot)$. It is easy to see that the set of autotopies of $Q(\cdot)$ forms a group.

Definition 2.3. The third component γ of the autotopy $T=(\alpha,\beta,\gamma)$ of the groupoid $Q(\cdot)$ is called quasi-automorphism of the groupoid $Q(\cdot)$. In other words, a permutation $\gamma: Q\to Q$ is called quasi-automorphism of the groupoid $Q(\cdot)$, if there exist permutations $\alpha,\beta: Q\to Q$ such that

$$\gamma(x\cdot y) = \alpha x\cdot \beta y,$$

i.e. $T=(\alpha,\beta,\gamma)$ is an autotopy of the groupoid $Q(\cdot)$.

In the case of groups, quasi-automorphisms have an easy construction.

Lemma 2.1. [4] Any quasi-automorphism γ of a group $Q(\cdot)$ has the form:

$$\gamma = \hat{R}_s\gamma_0, \quad (\gamma = \hat{L}_s\delta_0) \tag{2.1}$$

where $\gamma_0(\delta_0)$ is an automorphism of the group $Q(\cdot)$, $\hat{R}_s x = x \cdot s(\hat{L}_s x = s \cdot x),\ s \in Q$ and, reversely, the map γ defined by the equality (2.1) is a quasi-automorphism of the group $Q(\cdot)$.

Theorem 2.1. [4] Let the nonempty set Q form a quasigroup under four operations $A_i(i = 1,2,3,4)$. If these operations satisfy the following identity:

$$A_1(A_2(x,y),z) = A_3(x,A_4(y,z)), \qquad (2.2)$$

then there exists an operation $(\cdot)$ under which Q forms a group isotopic to all these four quasigroups.

Theorem 2.2. [13]

The invertible algebra $(Q;\Sigma)$ is a left linear if and only if for all $A,B \in \Sigma$ the following second-order formula

$$A(B(x,B^{-1}(u,y)),z) = A(B(x,B^{-1}(u,u)),A^{-1}(u,A(y,z))),$$

is valid in the algebra $(Q;\ \Sigma \cup \Sigma^{-1})$.

Theorem 2.3. [13]

The invertible algebra $(Q;\Sigma)$ is a right linear if and only if for all $A,B \in \Sigma$ the following second-order formula

$$A(x,B({}^{-1}B(y,u),z)) = A(\quad {}^{-1}A(A(x,y),u),B({}^{-1}B(u,u),z)),$$

is valid in the algebra $(Q;\ \Sigma \cup \quad {}^{-1}\Sigma\quad)$.

3. Left and right linear invertible algebras

Theorem 3.1. If the second-order formula

$$A(B(x,y),z) = A(\alpha_1^{A,B}x,\alpha_2^{A,B}A(\ \alpha_3^{A,B}y,z)) \qquad (3.1)$$

is valid in the invertible algebra $(Q;\ \Sigma)$for all $A,B \in \Sigma$ and for some permutations $\alpha_i^{A,B}(i = 1,2,3)$, then the algebra $(Q;\ \Sigma)$ is left linear.

Conversely, if the invertible algebra $(Q;\ \Sigma)$ is left right linear, then for all $A,B \in \Sigma$ exists $\alpha_i^{A,B}(i = 1,2,3)$ such that the second-order formula (3.1) is valid in the algebra $(Q;\ \Sigma)$.

Proof. Let (3.1) hold in $(Q;\ \Sigma)$ for all $A, B \in \Sigma$ and for some permutations $\alpha_i^{A,B}\ (i = 1,2,3)$. The identity (3.1) is a particular case of the associativity equation (2.2), where

$$A_1(x,y) = A(x,y), \qquad A_2(x,y) = B(x,y),$$
$$A_3(x,y) = A(\alpha_1^{A,B}x, y), \qquad A_4(x,y) = \alpha_2^{A,B}A(\alpha_3^{A,B}x, y).$$

According to Theorem 2.1, the quasigroups A_1, A_2, A_3, A_4 are isotopic to the same group $Q(\cdot)$, hence the operations A, B are isotopic to $Q(\cdot)$. Since the operations $A$and B are arbitrary, we obtain that all operations from Σ are isotopic to this group.

For every $X \in \Sigma$, let us define the operation:

$$x +_X y = X(R_{X,a}^{-1}x, L_{X,b}^{-1}y), \tag{3.2}$$

where a, b are some fixed elements from Q.

The operation $+_X$ is a loop operation with the identity element $0_X = X(b,a)$. Obviously, $(Q, +_X)$ is a loop isotopic to the group $Q(\cdot)$. Hence, by Albert's theorem, it is a group. For every $X \in \Sigma$ each $(Q, +_X)$ is a group. So, (3.1) can be rewritten in the form:

$$R_{A,a}(R_{B,a}x +_B L_{B,b}y) +_A L_{A,b}z = R_{A,a}\alpha_1^{A,B}x +_A L_{A,b}\alpha_2^{A,B}(R_{A,a}\alpha_3^{A,B}y +_X L_{A,b}z).$$

Taking $z = L_{A,b}^{-1}0_A$ in the last equality, we have

$$R_{A,a}(R_{B,a}x +_B L_{B,b}y) = R_{A,a}\alpha_1^{A,B}x +_A L_{A,b}\alpha_2^{A,B}R_{A,a}\alpha_3^{A,B}y.$$
$$R_{A,a}(x +_B y) = \alpha_{A,B}x +_A \beta_{A,B}y, \tag{3.3}$$

where $\alpha_{A,B} = R_{A,a}\alpha_1^{A,B}R_{B,a}^{-1}, \beta_{A,B} = L_{A,b}\alpha_2^{A,B}R_{A,a}\alpha_3^{A,B}L_{B,b}^{-1}$

are permutations of the set Q. Since the operations A and B are arbitrary we can take $A = B$ in (3.3). Hence

$$R_{A,a}(x +_A y) = \alpha_{A,A}x +_A \beta_{A,A}y \tag{3.4}$$

From (3.3) and (3.4) we have

$$\alpha_{A,B}^{-1}x +_B \beta_{A,B}^{-1} y = \alpha_{A,A}^{-1}x +_A \beta_{A,A}^{-1} y,$$

$$x +_A y = \gamma_{A,B}x +_B \delta_{A,B}\, y, \tag{3.5}$$

where $\gamma_{A,B} = \alpha_{A,B}^{-1}\alpha_{A,A}$ and $\delta_{A,B} = \beta_{A,B}^{-1}\beta_{A,A}$ are permutations of the set Q Hence, according to (3.5) we get

$$R_{A,a}(x +_B y) = \gamma_{A,B}\,\alpha_{A,B}x +_B \delta_{A,B}\,\beta_{A,B}y,$$

i.e. $R_{A,a}$ is a quasiautomorphism of the group $(Q; +_B)$. Since A is arbitrary we have that $R_{A,a}$ is a quasiautomorphism of the group $(Q; +_B)$ for all operations $A \in \Sigma$.

According to (3.2) we have

$$A(x,y) = R_{A,a} +_A L_{A,b}y.$$

This, according to (3.5), gives:

$$A(x,y) = \theta_{A,B}^1\; x +_B \theta_{A,B}^2\; y, \tag{3.6}$$

where $\theta_{A,B}^1 = \gamma_{A,B}R_{A,a}$ and $\theta_{A,B}^2 = \delta_{A,B}L_{A,b}$ are permutations of the set Q. Thus, we can represent every operation from Σ by the operation $+_B$.

Let $+ = +_B$. We prove that $\theta_{A,B}^1$ is a quasiautomorphism of the group $(Q;+)$. To do it, we take $z = (\theta_{A,B}^2)^{-1}0_B$ in (3.1) and rewrite this quality in the form:

$$\theta_{A,B}^1(R_{B,a}x + L_{B,b}y) + \theta_{A,B}^2 z = \theta_{A,B}^1\alpha_1^{A,B}x + \theta_{A,B}^2\alpha_2^{A,B}(\theta_{A,B}^1\alpha_3^{A,B}y + \theta_{A,B}^2 z),$$

$$\theta_{A,B}^1(R_{B,a}x + L_{B,b}y) = \theta_{A,B}^1\alpha_1^{A,B}x + \theta_{A,B}^2\alpha_2^{A,B}\theta_{A,B}^1\alpha_3^{A,B}y.$$

The last equality shows that $\theta_{A,B}^1$ is a quasiautomorphism of the group $(Q;+)$. According to Lemma 2.1 we have

$$\theta_{A,B}^1 x = \phi_A x + s_A,$$

where ϕ_A is an automorphism of the group $(Q; +)$ and s_A is some element of the set Q. Hence, it follows from (3.6) that

$$A(x,y) = \phi_A x + \beta_A y, \tag{3.7}$$

where $\beta_A y = s_A + \theta^2_{A,B} y$. Since A is an arbitrary operation we obtain that all operations from Σ can be represented in the form (3.7), i.e., the algebra $(Q; \Sigma)$ is left linear.

Conversely, if the invertible algebra is a left linear, then the following formula is valid in that algebra Theorem 2.2:

$$A(B(x,B^{-1}(u,y)),z) = A(B(x,B^{-1}(u,u)),A^{-1}(u,A(y,z)))$$

Having into consideration the following equalities:

$$B^{-1}(x,y) = L^{-1}_{B,x} y$$

$$A(x,y) = R_{A,y} x$$

the formula may be re-written in the following form:

$$A(B(x,y),z) = A(R_{B,B^{-1}(u,u)} x, L^{-1}_{A,u} A(L_{B,u} y, z)).$$

By taking $u = a$ where a is a fixed element from the Q we are getting the identity (3.1), where

$$\alpha_1^{A,B} = R_{B,B^{-1}(a,a)}, \alpha_2^{A,B} = L^{-1}_{A,u}, \alpha_3^{A,B} = L_{B,a}.$$

Corollary 3.1. [14] The class of left linear quasigroups is characterized by the following identity with permutations

$$xy \cdot z = R_{a \backslash a} x \cdot L_a^{-1}(L_a y \cdot z)$$

for some fixed element $a \in Q$.

Similarly, we can prove the following theorem.

Theorem 3.2. If the identity

$$A(x,B(y,z)) = A(\alpha_1^{A,B} A(x,\alpha_2^{A,B} y), \alpha_3^{A,B} z) \tag{3.8}$$

is valid in the invertible algebra $(Q; \Sigma)$ for all $A, B \in \Sigma$ and for some permutations $\alpha_i^{A,B}$ $(i = 1,2,3)$, then the algebra $(Q; \Sigma)$ is right linear.

Conversely, if the invertible algebra $(Q;\ \Sigma)$ is right linear, then for all $A, B \in \Sigma$ there exists $\alpha_i^{A,B}\ (i = 1,2,3)$ such that the identity (3.8) is valid in the algebra $(Q;\ \Sigma)$.

Corollary 3.2. [14] The class of right linear quasigroups is characterized by the following identity with permutations

$$x(yz) = R_a^{-1}(x \cdot R_a y) \cdot L_{a/a} z$$

for some fixed element $a \in Q$.

REFERENCES

1. *Schauffler R.* Die Assoziativitat im Ganzen Besonders bei Quasigruppen, Math. Zeitschr., vol. 67, n. 5. PP. 428–435, 1957.
2. *Aczel J.* Yorlensungen uiber Funktionalgleichungen und ihre Anwendungem, Berlin, VEB Deutsch. Verl.Wiss, 1961.
3. *Belousov V.D.* Balanced identities on quasigroups, Mat. Sb., vol. 70(112), n. 1. PP. 55–97, 1966 (Russian).
4. *Belousov V.D.* Globaly associative systems of quasigroups, Mat. Sb., vol. 55(97), n. 2. PP. 221–236, 1961 (Russian).
5. *Sade.* Theorie des systemes demosiens de groupoids, Pacif. J. Math., vol. 10, n. 2. PP. 625–660, 1960.
6. *Movsisyan Yu.M.* Hyperidentities and Related Concepts 1, Armenian Journal of Mathematics, vol. 9, n. 2. PP.146–222, 2017.
7. *Movsisyan Yu. M.* Introduction to the Theory of Algebras with Hyperidentities, Yerevan State University press, 1986 (Russian).
8. *Movsisyan Yu.M., Davidov S.S.* Algebras that are nearly quasigroups, Moscow, URSS, 2018 (Russian).
9. *Movsisyan Yu.M.* Hyperidentities in algebras and varieties, Russian Mathematical Surveys, vol. 53, n. 1. PP. 57–108, 1988.
10. *Movsisyan Yu. M.* Biprimitive classes of second order algebras, Mat. Issled, n. 9. PP. 70–82, 1974 (Russian).
11. *Belousov V.D.* Foundations of the Theory of Quasigroups and Loops, Nauka, 1967 (Russian).
12. *Davidov S.S.* A characterization of binary invertible algebras linear over a group, Quasigroups and Related Systems, vol. 19. PP. 207–222, 2011.

13. *Davidov S.S.* A characterization of binary invertible algebras of various type of linearity, Quasigroups and Related Systems, vol. 20. PP.169–176, 2012.
14. *Belyavskaya G.B., Tabarov A. Kh.* Identities with permutations leading to linearity of a quasigroup, Discrete Math. Appl. 19. PP.172–190, 2009.
15. *Davidov S.S., Shahnazaryan D.A.* Hyperidentities with permutations leading to the isotopy of invertible binary algebras to a group, Quasigroups and Related Systems, 2020 (to be printed).

СВЕРХТОЖДЕСТВА С ПОДСТАНОВКАМИ, ПРИВОДЯЩИМИ К ЛИНЕЙНОСТИ ОБРАТИМЫХ БИНАРНЫХ АЛГЕБР

С.С. Давидов, Д.А. Шахназарян

В данной работе с использованием формул второго порядка получены характеристики обратимых бинарных алгебр с различными типами линейности.

Ключевые слова: обратимая алгебра, линейная обратимая алгебра, формула второго порядка, сверхтождество, сверхтождество с подстановками, изотопия.

УДК 539.3

Поступила: 14.01.2020г.
Сдана на рецензию: 20.01.2020г.
Подписана к печати: 21.02.2020г.

LOVE'S TYPE WAVES IN THE SYSTEM OF THE CUBIC SYMMETRY PIEZOELECTRIC LAYER AND HALF-SPACE

A. Berberyan, V. Garakov

Institute of Mechanics, NAS, Armenia

slavia555@yahoo.com5nn, garakov@ yandex.com

ABSTRACT

The present work deals with the case where the layer has a piezoelectric property of cubic symmetry. The effect of boundary conditions on the outer boundary of the layer is investigated. Conditions of surface waves appearance are determined.

Keywords: piezoelectric, cubic symmetry, surface wave, elastic layer.

There is extensive literature on the propagation of elastic waves in piezoactive environments. These works can be found, in particular, in monographs [1-4]. A number of problems have also been investigated on shear surface waves in a layer-half-space system (Lyava-type waves), in the case where the layer material has a piezoactive property of hexagonal symmetry crystals of class 6mm [4-6]. In a rectangular Cartesian coordinate system (x, y, z), the piezoactive elastic layer occupies an area $-\infty < x < \infty, -h \le y \le 0, -\infty < z < \infty$.

The half-space $-\infty < x < 0,\ 0 \le y < \infty, -\infty < z < \infty$ is an elastic, electrically inactive (insensitive) material.

It is assumed that the material of the layer has the property of piezoelectric property of cubic symmetry, for which the equations of propagation of shear electroelastic waves in quasistatic approximation are true [1, 2].

$$C_{44}\vartriangle W+2e_{14}\frac{\partial^2\varphi}{\partial x\partial y}=\rho\frac{\partial^2 w}{\partial t^2},\varepsilon\vartriangle\varphi-2e_{14}\frac{\partial^2 w}{\partial x\partial y}=0 \qquad (1.1)$$

In (1.1) C_{44} is shear modulus, e_{14} is piezoelectric interaction coefficient , ε is permittivity, ρ isdensity of material layer, $w\ (x,y,t)$ is shear displacement function, $\varphi\ (x,y,t)$ is electric potential function, $\vartriangle$ is dimetric Laplace operator.

The equation of pure shear wave propagation is used for half-space

$$C_{tz}^2\vartriangle w_2=\frac{\partial^2 w_2}{\partial t^2},\ C_{tz}^2=\frac{G}{\rho_2} \qquad (1.2)$$

Here C_{tz} is the shear wave propagation rate, G is the module of shear, ρ_2 is the density of the half-space material.

Fade Condition Required

$$\lim_{y\to\infty} w_2=0 \qquad (1.3)$$

Conditions of continuity of movement, tangential voltage and conditions of electric field grounding are accepted on the contact of surface of layer and half-space connection

$$\omega_2=\omega,\ \sigma_{yz}^{(2)}=\sigma_{yz},\ \varphi=0 \text{ when } y=0 \qquad (1.4)$$

Different options for boundary conditions will be considered at the outer boundary of the layer $y=-h$.

The solution of the system of equations (1.1) is presented in the form of harmonic waves

$$w=f(y)\exp i(\omega t-kx),\ \varphi=g(y)\exp i(\omega t-kx) \qquad (1.5)$$

Substitution (1.5) in (1.1) results in the solution of the following system of ordinary differential equations

$$f'' + k^2\beta_1^2 f - 2ik\frac{e_{14}}{C_{44}}g' = 0 \tag{1.6}$$

$$g'' - k^2 g + 2ik\frac{e_{14}}{\varepsilon}f' = 0$$

where

$$\beta_1 = \sqrt{\frac{\omega^2}{k^2C_{t1}^2} - 1},\ C_{t1}^2 = \frac{C_{44}}{\rho} \tag{1.7}$$

Given that steady-state waves (oscillations) are considered, it is possible to determine f' from the second equation of the system (1.6) and substituting in the first equation, having previously been determined. As a result, we get the ordinary differential equation of the fourth degree

$$g^{IV} + k^2\left(\beta_1^2 - 1 - \chi\right)g^{II} - k^4\beta_1^2 g = 0 \tag{1.8}$$

where

$$\chi = 4\frac{e_{15}^2}{\varepsilon C_{44}} \tag{1.9}$$

is a coefficient of electromechanical coupling of piezocrystals of cubic symmetry.

The solution of equation (1.8) is represented by

$$g(y) = Be^{kpy} \tag{1.10}$$

Substitution (1.10) into (1.8) results in a solution to the biquadrate equation with respect to a parameter p that will have two (plus and minus) imaginary roots and two imputable ones. The general solution of equation (1.8) is written as follows:

$$g = B_1\sin kp_1 y + B_2\cos kp_1 y + B_3\,\mathrm{s}\,hkp_2 y + B_4 chkp_2 y \tag{1.11}$$

where

$$p_{1,2} = \frac{1}{\sqrt{2}}\left[\sqrt{(\beta_1^2 - 1 - \chi)^2 + 4\beta_1^2} \pm \left(\beta_1^2 - 1 - \chi\right)\right]^{1/2} \tag{1.12}$$

The solution for the function f is from the second equation of the system (1.6) taking into account (1.12)

$$f = \frac{i\varepsilon}{2e_{14}}\left[\frac{p_1^2+1}{p_1}\left(B_1\cos kp_1y - B_2\sin kp_1y\right) + \frac{p_2^2-1}{p_2}\left(B_3 chkp_2y + B_4 shkp_2y\right)\right] \quad (1.13)$$

Corresponding solution of equation (1.2) in the half-plane satisfying the damping condition (1.3) will be

$$w_2 = f_2(y)\exp i(\omega t - kx) \quad (1.14)$$

where

$$f_2(y) = Ae^{-k\beta_2 y},\ \beta_2 = \sqrt{1-\frac{\omega^2}{k^2c_{t2}^2}} \quad (1.15)$$

2. Taking into account the material equations

$$\sigma_{yz} = C_{44}\frac{\partial w}{\partial y} + e_{14}\frac{\partial\varphi}{\partial x},\ \sigma_{yz}^{(2)} = G\frac{\partial w}{\partial y} \quad (2.1)$$

and representations of solutions of equations in the form of (1.5) and (1.14) boundary conditions on contact surface (1.4) are obtained in the form of

$$f_2 = f_1,\ Gf_2' = C_{44}f',\ g = 0 \text{ at } y = 0 \quad (2.2)$$

Requirements that the functions (1.11), (1.13) and (1.14) satisfy the boundary conditions (2.2) result in the following connections between arbitrary permanent

$$A = \frac{i\varepsilon}{2e_{14}}\left(\frac{p_1^2+1}{p_1}B_1 + \frac{p_2^2-1}{p_2}B_3\right),$$

$$\beta_2 GA = \frac{i\varepsilon}{2e_{14}}\left[\left(p_1^2+1\right)B_2 - \left(p_2^2-1\right)B_4\right], \quad (2.3)$$

$$B_4 + B_2 = 0$$

By excluding an arbitrary constant A, the system (2.3) is replaced by equations

$$\rho_2 G\left(\frac{p_1^2+1}{p_1}B_1 + \frac{p_1^2-1}{p_2}B_3\right) = C_{44}\left(p_1^2+p_2^2\right)B_2,\ B_4 = -B_2 \quad (2.4)$$

Let conditions be set on the outer boundary of the layer

$$\sigma_{yz} = 0,\ \varphi = 0 \text{ at } y = -h \quad (2.5)$$

Requiring that the solutions obtained above satisfy the boundary conditions (2.5) and considering $B_4=-B_2$ that we obtain an equation regarding arbitrary constants B_1, B_2, B_3

$$B_1 \operatorname{sinkp}_1 h - B_2\left(\operatorname{coskp}_1 h - ch\,\mathrm{kp}_2 h\right) + B_3 \operatorname{shkp}_2 h = 0 \tag{2.6}$$

$$\left(p_1^2+1\right)B_1 \operatorname{sinkp}_1 h - B_2\left[\left(p_1^2+1\right)\cos kp_1 h - \left(p_2^2-1\right)\operatorname{chkp}_2 h - \left(p_2^2-1\right)\mathrm{B}_3 \operatorname{shkp}_2 h\right] = 0$$

Equation (2.6) together with the first equation from (2.4) makes up a system of three homogeneous algebraic equations with respect to arbitrary constants B_1, B_2, B_3. The condition that the determinant of this system is equal to zero gives an equation that determines the phase velocities of surface waves

Equality of zero determinant of the system of equations (2.4), (2.6) after some transformations is given to

$$\begin{gathered}\left(p_1^2+p_2^2\right)\operatorname{sinp}_1 kh\,sh\,\mathrm{p}_2 kh + S_3\left(p_1^2-p_2^2+2\right)\operatorname{sinp}_1 kh\,ch\,\mathrm{p}_2 kh - \\ -S_1 sh\,\mathrm{p}_2 kh\left[2\left(p_1^2-1\right)ch\,\mathrm{p}_2 kh - \left(p_1^2+p_2^2\right)\operatorname{cosp}_1 kh\right] = 0\end{gathered} \tag{2.7}$$

where

$$S_1 = \frac{\beta_2 G\left(p_1^2+1\right)}{C_{44}\left(p_1^2+p_2^2\right)p_1},\quad S_2 = \frac{\beta_2 G\left(p_2^2-1\right)}{C_{44}\left(p_1^2+p_2^2\right)p_2} \tag{2.8}$$

In particular case of absence of piezoeffect $(\chi=0)$, equation (2.7) is given to known equation of Love surface wave problem [7].

$$tg\beta_1 kh = \frac{\beta_2 G}{C_{44}\beta_1} \tag{2.9}$$

As is known, equation (2.9) $\beta_2=0\left(\varpi^2/k^2=C_{t2}^2\right)$ determines at what kh time the n-th mode of the Love's wave will appear.

$$kh = \left(\frac{C_t^2}{C_{t1}^2}-1\right)^{-\frac{1}{2}} n\pi,\ (n=0,1,2....) \tag{2.10}$$

Similarly to the Love's task, from equation (2.7) for the *n*-th mode if we take into account the piezoeffect, it is obtained

$$kh = \gamma n\pi \qquad (2.11)$$

where

$$\gamma = \sqrt{2}\left[\sqrt{\left(\frac{C_t^2}{C_{t1}^2}-2-\chi\right)^2+4\left(\frac{C_t^2}{C_{t1}^2}-1\right)}+\left(\frac{C_t^2}{C_{t1}^2}-2-\chi\right)\right]^{-\frac{1}{2}} \qquad (2.12)$$

The table shows the meaning of γ for the case $C_t^2 = 2Ct_{t1}^2$

χ	0,00	0,1	0,2	0,3	0,4	0,5
γ	1,00	1,026	1,051	1,078	1,105	1,131

It follows that the larger the electromechanical coupling coefficient is, the larger the next surface wave mode appears for larger values kh.

3. In this paragraph another variant of boundary conditions at the outer boundary of the layer is considered

$$w = 0, D_2 = 0 \ \text{at}\ y = -h \qquad (3.1)$$

Taking into account the material eguation for the induction of an electric field

$$D_2 = -\varepsilon\frac{\partial\varphi}{\partial y} + e_{14}\frac{\partial\omega}{\partial x} \qquad (3.2)$$

and (1.5), the boundary conditions lead to

$$f = 0, g' = 0 \ \text{at}\ y = -h \qquad (3.3)$$

The requirement that (1.11), (1.13) satisfy (3.3) leads to the following algebraic equation for arbitrary constants B_i.

$$\begin{aligned}&\frac{p_1^2+1}{p_1^2}\left(B_1\cos kp_1h + B_2\sin kp_1h\right)+\frac{p_2^2-1}{p_2}\left(B_3chk\,\mathrm{p}_2\,h - B_4shk\,\mathrm{p}_2\,h\right)=0\\&p_1B_1\cos kp_1h - p_1B_2\sin kp_1h + \mathrm{p}_2\,B_3chk\,\mathrm{p}_2\,h - \mathrm{p}_2\,B_4shk\,\mathrm{p}_2\,h = 0\end{aligned} \qquad (3.4)$$

The equation (3.4) with (2.4) makes up a homogeneous system of equations for the four sought constants $B_i\,(i=1,2,3,4)$. The condition that

the determinant of this system is equal to zero after some transformations leads to the following dispersion equation

$$p_1p_2\left(p_2^2-p_1^2\right)\cos kp_1h+\beta_2\frac{G}{C_{44}}\left[p_2\left(p_1^2+1\right)\sin kp_1h+p_1\left(p_2^2-1\right)\mathrm{s}\,hkp_2h\right]=0 \quad (3.5)$$

The condition for the appearance of a surface wave of n -mode of Love type, as in the previous case, is seen from the equation (3.5), considering $\beta_2=0$

$$\cos kp_1h=0\,(3.6)\text{ or}$$

$$kh=\gamma\left(\frac{\pi}{2}+n\pi\right) \quad (3.7)$$

In (3.7) γ can be determinedby (2.13). Comparison of (2.12) and (3.7) shows that appearance of modes differ by $\pi/2$.

Based on equation (3.5), particularly

$$\left(kp_1h\right)^2<<1,\left(kp_2h\right)^2<<1 \quad (3.8)$$

we consider the following equation

$$L\left(\omega_1kh\right)\equiv\left(\beta_2\frac{G}{C_{44}}-1\right)\left(\beta_1^2-1-\kappa\right)^2+4\beta_1^2=0 \quad (3.9)$$

Conclusion. A generalized Love problem has been investigated in the case where the material is a class 6mm piezoelectric. The dispersion equation of the problem is obtained. Conditions of surface wave modes appearance depending on electromechanical coupling coefficient are determined.

REFERENCES

1. *Balakirev M.K., Gilinsky I.A.* Waves in piezocrystals. Novosibirsk, Science, 1982, 239c.
2. *Parton V.Z., Kudryavtsev B.A.* Electromag notoelastic of piezoelectric electrically conductive bodies M.Nauk, 1988, 472p.

3. *Bardzokas D.I., Kudryavtsev B.A., Senik N.A.* Wave propagation in electro elastic environments M.Ediotoriya.URSS, 2003, 336p.
4. *Bagdasaryan G.E., Danoyan Z.N.* Electro magneto elastic waves. Yerevan, Ed. YSU. 2006, 492p.
5. *Avetisyan A.S., Kamalyan A.A.* On Propagation of Electroe lastic Shear Signal in Non-Uniform.
6. Piezoelectric Layer of Class 6 mm//Dockl. NAN of Armenia, 2014, № 2. PP.108–115.
7. *Belubekyan V.M., Belubekyan M.V.* Surface electroelastic waves in piezoelectric system layer half-space//Scientists notes of the ECU, 2006, № 3. PP. 25–30.
8. *Novatski V.* Theory of elasticity. M.: Mir, 1975, 872p.

ВОЛНЫ ТИПА ЛЯВА В СИСТЕМЕ КУБИЧЕСКАЯ СИММЕТРИЯ-ПЬЕЗОЭЛЕКТРИЧЕСКИЙ СЛОЙ-ПОЛУПРОСТРАНСТВО

А.Х. Берберян, В.Г. Гараков

АННОТАЦИЯ

В настоящей работе рассматривается вариант, когда слой обладает пьезоэлектрическим свойством кубической симметрии. Исследуется влияние граничных условий на внешней границе слоя. Определяются условия появления поверхностных волн.

Ключевые слова: пьезоэлектрик, кубическая симметрия, поверхностная волна, эластический слой.

УДК 004.852

ON THE TRADEOFF BETWEEN ACCURACY AND FAIRNESS IN REPRESENTATION LEARNING

T. Galstyan, H. Khachatrian

YerevaNN
Yerevan State University

tigran@yerevann.com, hrant@yerevann.com

ABSTRACT

In many applications of machine learning, it is desirable to have models which not only have good accuracy on the prediction task but are also “fair” with respect to some protected variable. One approach to achieving fairness is to learn an invariant representation of the data with respect to that variable and then learn the predictor on top of the representation. Recently, an information-theoretic approach called DSF (Discovery and Separation of Features) was introduced, which demonstrated strong results on several datasets where the label and the protected variable are independent. In this paper we extend the model to work in cases when the protected variable is correlated with the label. We perform experiments on a small image classification dataset and show that our model enables significantly better tradeoffs between accuracy and fairness.

Keywords: machine learning, representation learning, information theory.

1. Introduction

Learning “fair” or “invariant” representations of data with respect to some protected variable is an important task in machine learning. In supervised learning, the goal is to find a function which can predict an

unknown variable y from the given variable x. In some applications, it is also necessary to guarantee the function does not depend on a specified variable c, which might be correlated with x and/or y. For example, the training data might have biases, which can result in functions that discriminate against certain groups of people [1]. One general approach to obtain functions with such guarantees is to learn a "fair" representation of data which attempts to simultaneously satisfy two constraints: it should not contain information about the protected variable (e.g. race of the person), but it should also keep enough information about x so that it is possible to predict the desired variable [2].

In the context of neural networks, fair representations have been achieved by extending variational autoen coders [3], by using adversarial techniques (e.g. when an adversarial classifier attempts to predict the protected information from the representation) [4], and by modifying the objective of the variational information bottleneck [5].

In [6], the method based on information bottleneck was extended into a full representation learning system, which can automatically discover the features relevant for the main prediction task (predicting y) and separate them from the rest of the features available in the data. The method is called DSF (discovery and separation of features). Experiments have showed that DSF learns a representation which is good enough for predicting the label, and at the same time it cannot be used for predicting the protected variable c. These experiments were designed under the assumption that y and c are independent. In this paper we discuss the case when there is some dependency between $y$and c. We still want to obtain a representation which has no information about the protected variable, even if it decreases the accuracy of predicting the label y.

In Section 2, we will describe the DSF model and will show its limitations when y and c are not independent. Section 3 will describe our proposed modifications to the algorithm. Section 4 will describe the experimental setup and Section 5 will present the results of our experiments.

2. DSF model and its limitations

We follow the notation from [7]. We will use upper case letters such as X for random variables, and lower case letters such as x for realizations. We assume the data comes from an unknown $P(X,Y,C)$ joint distribution. For simplicity, we assume the support for random variables C and Y (denoted by Ω_C and Ω_Y, respectively) are finite. For $(x,y,c) \sim P(X,Y,C)$, the goal is to learn a representation of x, $z = f_z(x)$, such that it is possible to learn a predictor $\hat{y} = f_y(z)$ with high accuracy, while z has no information about c.

The DSF model attempts to achieve the goal by solving the following constrained optimization problem:

$$\begin{aligned} \max \quad & \alpha I(Z_p\colon Y) + I(X\colon\{Z_p,Z_n\}) \\ \text{s.t.} \quad & I(Z_p\colon X) \le I_c \\ & I(Z_p\colon Z_n) = 0 \end{aligned} \tag{1}$$

Here $I(\cdot\colon\cdot)$ is Shannon mutual information between two random variables; Z_p and Z_n are representations of X. The authors attempt to solve (1) by maximizing the following objective:

$$J \;= \alpha I(Z_p\colon Y) + I(X\colon\{Z_p,Z_n\}) - \lambda I(Z_p\colon X) - \gamma I(Z_p\colon Z_n) \tag{2}$$

The first two terms are maximized using their variational lower bounds from [8]. The third term is directly optimized using a recently introduced technique based on “echo-noise” [9]. For the fourth term, two approaches are studied.

The first approach (called DSF-H) attempts to minimize the fourth term of (2) by Hilbert-Schmidt independence criterion [10], so the objective function becomes:

$$\begin{aligned} \hat{J}_{\mathrm{DSF-H}} = \quad & \alpha\mathbb{E}\log p(y|z_p) + \mathbb{E}\log p(x|\{z_p,z_n\}) \\ & +\lambda\mathbb{E}\log|\det S_p(x)| - \gamma \mathrm{HSIC}(z_p,z_n) \end{aligned} \tag{3}$$

The second approach (called DSF-C) represents the fourth term as a sum of three other mutual information terms, and ends up with the following training objective:

$$\begin{aligned} \hat{J}_{\mathrm{DSF-C}} = \quad & \alpha\mathbb{E}\log p(y|z_p) + (1+\gamma)\mathbb{E}\log p(x|\{z_p,z_n\}) \\ & +(\lambda+\gamma)\mathbb{E}\log|\det S_p(x)| + \gamma\mathbb{E}\log|\det S_n(x)| \end{aligned} \tag{4}$$

The authors of DSF perform several experiments with these two variants. In particular, they use a dataset called MNIST-ROT [11], which contains MNIST digits randomly (but uniformly) rotated by $\alpha \in \Omega_C = \{-45, -22.5, 0, 22.5, 45\}$ degrees. The goal is to predict the original label Y ($\Omega_Y = \{0, 1, \dots, 9\}$), while the learned representation should have no information about the rotation angle. Both DSF-C and DSF-H learn to predict Y with more than 98% accuracy from a learned representation Z_p, while ensuring that a multi-layer perceptron trained to predict C from Z_p does not get more than 20% of accuracy. Note that $p(C|Y = y)$ is uniform for all $y \in \Omega_Y$ in this dataset, which implies y and c are independent.

The next proposition shows that if $p(C|Y = y)$ is not uniform, then a representation that allows perfect classification of Y will contain at least some information about C.

Proposition 1. If there exists a classifier f with $acc(Y|f(X)) = 1$, then there exists a classifier

$$f_C \text{ s.t. } acc(C|f_C(X)) = \sum_{y \in \Omega_Y} p\,(y) \max_{c \in \Omega_C} p(c|y).$$

Proof. Suppose we have a perfect classifier f with $acc(Y|f(X)) = 1$. We define a simple classifier f_C for predicting C from X. For each x, denote the prediction of $f(x)$ by $\hat{y} = f(x)$.

We define $f_C(x) \triangleq \arg\max_{c \in \Omega_C} p(c|\,\hat{y})$ for every x. Basically, $f_C(x)$ predicts the most probable c for its predicted label $\hat{y}$, where $\hat{y} = y$, as $f(x)$ is a perfect classifier. The predicted $\hat{c} = f_C(x)$ will be correct with probability $\max_{c \in \Omega_C} p(c|\,\hat{y})$. The accuracy of $f_C(x)$ will be this probability weighted by the probabilities of $y \in \Omega_Y$ across the entire dataset. Note that if $p(C|y)$ is uniform for each y, and $p(Y)$ is also uniform, this accuracy equals to $\frac{1}{|\Omega_C|}$.

3. Proposed modifications to DSF

We are interested in the case when Y and C are not independent. In particular, we consider the case when the marginal distribution $p(C)$ is

uniform, but $p(C|Y=y)$ is not necessarily uniform for each $y \in \Omega_Y$. This allows non-zero mutual information between $Y$and C.

It is easy to see that the optimization problem (1) can have solutions for which $I(Z_p:Y) = H(Y)$. In such solutions, Z_p will contain at least some information about C, as $I(Y:C) > 0$. To avoid such solutions, we suggest two modifications to DSF.

First, we note that maximizing $I(Z_p:Y)$ will push Z_p to contain more information about Y. We want to modify that term such that it can be maximized without increasing mutual information between $Z_p$and C. We suggest to maximize $I(Z_p:Y|C)$ instead of $I(Z_p:Y)$.

The intuition behind the second modification is that the original DSF model does not have a mechanism to move the entire information about C from Z_p to Z_n if C and Y are not independent. So, we suggest to add additional constraints on Z_p and Z_n to have no mutual information with C. As a result of this, X cannot be fully represented with a concatenation of Z_p and Z_n anymore. So we also modify the second term in DSF's objective to maximize mutual information between X and the triplet $\{Z_p, Z_n, C\}$. The resulting optimization problem becomes:

$$\begin{aligned} \max \quad & \alpha I(Z_p:Y|C) + I(X:\{Z_p, Z_n, C\}) \\ \text{s.t.} \quad & I(Z_p:X) \leq I_c \\ & I(Z_p:Z_n) = I(Z_p:C) = I(Z_n:C) = 0 \end{aligned} \tag{5}$$

This problem can be solved by maximizing the following objective function:

$$\begin{aligned} J_{\text{sDSF}} \quad &= \alpha I(Z_p:Y|C) + I(X:\{Z_p, Z_n, C\}) - \lambda I(Z_p:X) \\ &- \gamma I(Z_p:Z_n) - \gamma I(Z_p:C) - \gamma I(Z_n:C) \end{aligned} \tag{6}$$

We call this model *supervised* DSF (sDSF), as we have access to supervision signal on C. To maximize the first term in (6), we first note that $I(Z_p:Y|C) = I(Y:\{C, Z_p\}) - I(Y:C)$, where $I(Y:C)$ is constant and $I(Y:\{C, Z_p\})$ can be approximated by the log-likelihood of a predictor which predicts Y from Z_p and C. The second term can be maximized using a "decoder", similar to the one used in DSF. The third term can be optimized

using the technique based on echo noise [9]. For the remaining three terms we try two approaches, following the original implementation of DSF. The first approach uses Hilbert-Schmidt independence criterion for all three terms. The training objective becomes:

$$\begin{aligned}\hat{J}_{\mathrm{sDSF-H}} = \quad & \alpha \mathbb{E}\log p(Y|Z_p, C) + \mathbb{E}\log p(X|\{Z_p, Z_n, C\}) + \lambda \mathbb{E}\log|\det S_p(X)| \\ & -\gamma_1 \mathrm{HSIC}(Z_p, Z_n) - \gamma_2 \mathrm{HSIC}(Z_p, C) - \gamma_3 \mathrm{HSIC}(Z_n, C)\end{aligned} \quad (7)$$

The second approach follows the "independence through compression" strategy. To make it work, we replace the second constraint of (5) with an equivalent constraint $I(Z_p:\{Z_n, C\}) + I(Z_n:C) = 0$. Thus, the objective becomes:

$$\begin{aligned}J_{\mathrm{sDSF-C}} = \quad & \alpha I(Z_p:Y|C) + I(X:\{Z_p, Z_n, C\}) - \lambda I(z_p:x) \\ & -\gamma(I(Z_p:\{Z_n, C\}) + I(Z_n:C)) \\ = \quad & \alpha I(Z_p:Y) + (1+\gamma) I(X:\{Z_p, Z_n, C\}) - (\lambda+\gamma) I(z_p:x) \\ & -\gamma I(Z_n:X) - \gamma I(X:C)\end{aligned} \quad (8)$$

The latter equality follows from the following lemma.

Lemma 1. If Z_p and Z_n depend only on X, then $I(Z_p:\{Z_n, C\}) + I(Z_n:C) = I(Z_p:X) + I(Z_n:X) + I(X:C) - I(X:\{Z_p, Z_n, C\})$.

Proof. We will use the following information-theoretic identities:

$$I(X:Y) = I(X:Z) - I(X:Z|Y) + I(X:Y|Z) \quad (9)$$

$$I(X:Y|Z) = I(Y:\{X, Z\}) - I(Z:Y) \quad (10)$$

As Z_n depends only on X, we have that $I(Z_n:C|X) = 0$. Then,

$$\begin{aligned}I(Z_n:C) & = I(Z_n:X) - I(Z_n:X|C) + I(Z_n:C|X) && (using\ (9)) \\ & = I(Z_n:X) - I(Z_n:X|C) && (as\ I(Z_n:C|X) = 0) \\ & = I(Z_n:X) - I(X:\{Z_n, C\}) + I(C:X) && (using\ (10))\end{aligned} \quad (11)$$

Another application of (9) gives:

$$I(Z_p:X) = I(Z_p:\{Z_n, C\}) - I(Z_p:\{Z_n, C\}|X) + I(Z_p:X|\{Z_n, C\}) \quad (12)$$

As Z_p also depends only on X, we have that $I(z_p:\{z_n, c\}|X) = 0$. So,

$$\begin{aligned}I(Z_p:\{Z_n, C\}) & = I(Z_p:X) + I(Z_p:\{Z_n, C\}|X) - I(Z_p:X|\{Z_n, C\}) \ (from\ (12)) \\ & = I(Z_p:X) - I(Z_p:X|\{Z_n, C\}) \\ & = I(Z_p:X) - I(X:\{Z_p, Z_n, C\}) + I(X:\{Z_n, C\}) \quad (using\ (10))\end{aligned}$$

By adding this identity to (11), we complete the proof.

To optimize (8), we note that $I(X\colon C)$ is constant, and $I(Z_n\colon X)$ can be minimized the same way as $I(Z_p\colon X)$. Hence, the training objective becomes:

$$\begin{aligned}\hat{J}_{\mathrm{sDSF-C}} = \quad & \alpha\mathbb{E}\log p(Y|Z_p, C) + (1+\gamma)\mathbb{E}\log p(X|\{Z_p, Z_n, C\}) \\ & -(\lambda+\gamma)\mathbb{E}\log|\det S_p(X)| - \gamma\mathbb{E}\log|\det S_n(X)|\end{aligned} \quad (13)$$

4. Experimental Setup

For our experiments we use modified version of MNIST-ROT dataset. We keep only two digits, $\Omega_Y = \{4,9\}$ and use larger rotation angles $\Omega_C = \{0, \pm 45, \pm 90\}$, as MNIST digits already have small inherent variability in rotation angles. The rotation angles are not uniformly distributed for each digit. In particular, $p(C|Y=4) = (0.3,0.25,0.2,0.15,0.1)$ and $p(C|Y=9) = (0.1,0.15,0.2,0.25,0.3)$. This ensures the marginal distribution $p(C)$ is uniform, but a model with a perfect accuracy on Y will have at least 30% accuracy according to Proposition 1. Training, validation and test sets contain 7594, 1903 and 2294 samples, respectively.

Following [6], we optimize (13) and (7) using three neural networks: an encoder, a decoder and a classifier. The encoder consists of two different neural networks which produce independent representations $Z_p$and Z_n. Both representations are produced using echo sampling procedure [9]. The decoder takes these representations along with one-hot embedding of C, and attempts to reconstruct the input image. Both encoders and the decoder are fully convolutional networks. The classifier is a linear layer with softmax activation. Its input is the concatenation of Z_p and one-hot embedding of C.

We perform experiments with six models: regular DSF-C, two versions of supervised DSF: sDSF-C, sDSF-H, and three ablated version of sSDF-C to examine the importance of its components.

We trained every model for 1000 epochs using Adam optimizer with learning rate of 0.001. For each version of our models, we performed grid search over $\lambda \in \{0.1,0.3,0.6,0.9,1.2\}$ and $\gamma \in \{0.1,0.3,0.5,0.7,0.9\}$. We used $\alpha = 1$ everywhere. For all experiments we set batch size to 150, size

of Z_p and Z_n to 5 and 100, respectively. This difference is motivated by the fact that Z_p should only contain few bits of information relevant for predicting Y, while Z_n should contain enough information to reconstruct X. For each choice of hyperparameters, we take six checkpoints (on epochs 100, 200, 400, 600, 800 and 1000). We evaluate each checkpoint by training two separate classifiers on the test set, one for predicting C from Z_p and one for predicting Y from Z_p, and measuring accuracies of these two classifiers. The goal is to find a model, for which $acc(C|Z_p)$ is close to random (which is 20% in our setup) while $acc(Y|Z_p)$ is as high as possible.

5. Results

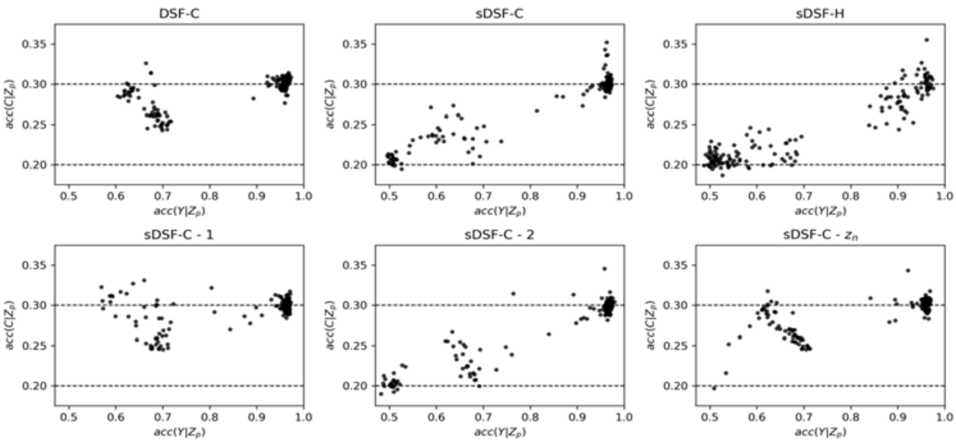


Figure 1. Results of the six models on modified MNIST-ROT. Horizontal and vertical axes show $acc(Y|Z_p)$ and $acc(C|Z_p)$, respectively.

Fig. 1 shows our results. Each plot corresponds to one of the six models described in the previous section. The points correspond to all checkpoints of all hyperparameter choices. The coordinates of the points in the plot show accuracies of predicting Y and C from the Z_p at the specified checkpoint.

The first plot shows the results of our baseline: plain DSF-C from [6]. Surprisingly, all the points are concentrated in three clusters. One cluster corresponds to near-perfect accuracies for Y, but has around 30% accuracy for C, as predicted by Proposition 1. The checkpoints from the second cluster predict C with around 25% accuracy but sacrifice $acc(Y|Z_p)$ down to around 70%. The third cluster is even worse with $acc(Y|Z_p)$ around 65% and $acc(C|Z_p)$ around 28%.

The second and third plots of Fig.1show the versions of our models: sDSF-C and sDSF-H. It can be seen that there are a few sDSF-C checkpoints which have around 22% accuracy for predicting C, while $acc(Y|Z_p)$ is around 70%. These are already superior to the baseline models. On the other hand, sDSF-C checkpoints with less than 20.5% $acc(C|Z_p)$ appear only with $acc(Y|Z_p) < 55\%$, which means they have almost no information about the label. sDSF-H is slightly better than sDSF-C by two aspects. First, the best checkpoints with $acc(C|Z_p) = 25\%$ get around 85% $acc(Y|Z_p)$. Second, the best checkpoints with $acc(C|Z_p) \leq 20\%$ have around 67% accuracy for predicting Y.

We perform an ablation study on sDSF-C. The second row of Fig. 1 shows that our first improvement on top of DSF models (maximizing $I(Y: Z_p|C)$ instead of $I(Y: Z_p)$) is critical. If we remove it from sDSF-C, the plot becomes very similar to the baseline plot. On the other hand, removal of our second improvement (the constraint of having no information about C in $Z_p$and Z_n) is not helpful (the fifth plot in Fig. 1). Finally, we see that even though Z_n does not directly participate in the measurements of $acc(C|Z_p)$and $acc(Y|Z_p)$, it has a critical role in sDSF-C. Without Z_n, the decoder forces the encoder to store more information about C in Z_p. Tables 1 and 2 summarize the results.

Table 1.

The best models according to $acc(Y|Z_p)$, when $acc(C|Z_p)$ is constrained. Hyperparameters of the best model are shown in parentheses.

	The best $acc(Y\|Z_p)$	The best $acc(Y\|Z_p)$
	if $acc(C\|Z_p) \leq 0.25$	if $acc(C\|Z_p) \leq 0.21$
DSF-C	0.71 ($\lambda = 1.2$, $\gamma = 0.5$, 400 ep.)	0.50 (N/A)
sDSF-C	0.74 ($\lambda = 0.6$, $\gamma = 0.9$, 400 ep.)	0.68 ($\lambda = 1.2$, $\gamma = 0.7$, 400 ep.)
sDSF-H	0.90 ($\lambda = 0.1$, $\gamma = 0.5$, 800 ep.)	0.68 ($\lambda = 1.2$, $\gamma = 0.3$, 800 ep.)
sDSF-C - 1	0.71 ($\lambda = 1.2$, $\gamma = 0.9$, 400 ep.)	0.50 (N/A)
sDSF-C - 2	0.76 ($\lambda = 0.6$, $\gamma = 0.9$, 400 ep.)	0.69 ($\lambda = 1.2$, $\gamma = 0.9$, 800 ep.)
sDSF-C - z_n	0.71 ($\lambda = 1.2$, $\gamma = 0.9$, 600 ep.)	0.51 ($\lambda = 0.3$, $\gamma = 0.3$, 100 ep.)

Table 2.

The best models according to $acc(C|Z_p)$, when $acc(Y|Z_p)$ is at least some threshold. Hyperparameters of the best model are shown in parentheses.

	The lowest $acc(C\|Z_p)$	The lowest $acc(C\|Z_p)$
	if $acc(Y\|Z_p) \geq 0.69$	if $acc(Y\|Z_p) \geq 0.85$
DSF-C	0.24 ($\lambda = 1.2$, $\gamma = 0.7$, 400 ep.)	0.28 ($\lambda = 0.1$, $\gamma = 0.5$, 600 ep.)
sDSF-C	0.21 ($\lambda = 1.2$, $\gamma = 0.9$, 600 ep.)	0.27 ($\lambda = 1.2$, $\gamma = 0.1$, 400 ep.)

sDSF-H	0.24 ($\lambda = 1.2$, $\gamma = 0.0$, 400 ep.)	0.24 ($\lambda = 0.1$, $\gamma = 0.5$, 800 ep.)
sDSF-C - 1	0.25 ($\lambda = 1.2$, $\gamma = 0.7$, 400 ep.)	0.28 ($\lambda = 0.6$, $\gamma = 0.7$, 400 ep.)
sDSF-C - 2	0.20 ($\lambda = 1.2$, $\gamma = 0.9$, 800 ep.)	0.28 ($\lambda = 1.2$, $\gamma = 0.7$, 800 ep.)
sDSF-C - z_n	0.25 ($\lambda = 1.2$, $\gamma = 0.9$, 400 ep.)	0.28 ($\lambda = 0.9$, $\gamma = 0.9$, 600 ep.)

Acknowledgement

We would like to thank Aram Galstyan and Greg Ver Steeg for valuable comments, discussions and support.

REFERENCES

1. *Kamiran F., Calders T.* Classifying without discriminating, 2nd international conference on computer, control and communication, IEEE, 1–6, 2009.
2. *Zemel R., Wu., Swersky K., et al.* Learning fair representations, International conference on machine learning, 325–333, 2013.
3. *Zemel Y., Louizos C., Swersky K.* The variational fair autoencoder, Proceedings of the international conference on learning representations, 2016.
4. *Xie Q., Dai Z., Du Y., et al.* Controllable invariance through adversarial feature learning, Advances in neural information processing systems, 585–596, 2017.
5. *Moyer D., Gao S., Brekelmans R., et al.* Invariant representations without adversarial training, Advances in neural information processing systems, 9084–9093, 2018.
6. *Jaiswal A., Brekelmans R., Moyer D., et al.* Discovery and separation of features for invariant representation learning. arXiv preprint arXiv:191200646, 2019.
7. *Meyen S.* Relation between classification accuracy and mutual information in equally weighted classification tasks, 2016.
8. *Alemi A., Fischer I., Dillon J., et al.* Deep variational information bottleneck, 2017.
9. *Brekelmans R., Moyer D., Galstyan A., et al.* Exact rate-distortion in autoencoders via echo noise, Advances in neural information processing systems, 3884–3895, 2019.

10. *Gretton A., Fukumizu K., Teo C., et al.* A kernel statistical test of independence, Advances in neural information processing systems, 585–592, 2008.
11. *Jaiswal A., Wu R., Abd-Almageed W., et al.* Unsupervised Adversarial Invariance. Advances in neural information processing systems 31, Curran Associates, Inc., 5097–5107, 2018.

О КОМПРОМИССЕ МЕЖДУ ТОЧНОСТЬЮ И СПРАВЕДЛИВОСТЬЮ В ОБУЧЕНИИ ПРЕДСТАВЛЕНИЙ

Т. Галстян, Г. Хачатрян

АННОТАЦИЯ

Во многих приложениях машинного обучения желательно иметь модели, которые не только обладают хорошей точностью предсказания, но и являются «справедливым» по отношению к какой-то защищенной переменной. Одним из подходов к достижению справедливости является обучение инвариантному представлению данных относительно этой переменной, а затем обучение модели сверх этого представления. Недавно был представлен информационно-теоретический подход DSF (Discovery and Separation of Features), который продемонстрировал хорошие результаты для нескольких наборов данных, где метка и защищенная переменная независимы. В данной статье мы рассматриваем случай, когда есть корреляция между меткой и защищенной переменной. Проведенные эксперименты на наборах данных для классификации небольших изображений показали, что наша модель позволяет значительно улучшить компромисс между точностью и справедливостью.

Ключевые слова: машинное обучение, обучение представлений, теория информации.

ФИЗИКО-ТЕХНИЧЕСКИЕ НАУКИ

УДК621.396.673

Поступила: 13.03.2020г.
Сдана на рецензию: 19.03.2020г.
Подписана к печати: 14.04.2020г.

РАЗРАБОТКА ДИСКОНУСНОЙ АНТЕННЫ С КОПЛАНАРНЫМ ВОЛНОВОДОМ

А.Г. Степанян[1], С.Г. Эйрамджян[2]

[1]Национальный политехнический университет Армении
[2]Российско-Армянский университет

araratstepanyan9@gmail.com, *eyrsuren@gmail.com*

АННОТАЦИЯ

С развитием телекоммуникационных систем использование всенаправленных антенн становится все более важным и актуальным. Используемая сейчас ширина частотной полосы увеличивается, поэтому необходимо создавать новые антенны, которые будут иметь широкий диапазон рабочих частот. Была исследована и разработа дисконусная антенна, на основе которой была создана копланарная конструкция антенны. Проектирование реализовано в программной среде FEKO. Результаты расчетов представлены в виде графиков. Дано сравнение результатов расчетов двух антенн.

Ключевые слова: всенаправленная антенна, широкополосная антенна, дисконусная антенна, программная среда FEKO.

Введение. Дисконусные антенны являются распространенным типом всенаправленных антенн и характеризуются симметрично ориентированной диаграммой в широком частотном диапазоне. Антенна содержит излучающий (принимающий) диск, коническую плоскость заземления и изолятор между ними. На Рис. 1 показана структура антенны. Входное сопротивление обычно составляет около 50 Ом в широком диапазоне частот и не содержит реактивных компонент, поэтому коаксиальную линию передачи можно подключить к антенне без дополнительных согласователей [1].

В современных радиотехнических системах широкое применение нашли копланарные антенны, которые в основном устанавливаются на диэлектриках. Данные антенны имеют малые габариты, легко интегрируются в радиотехнические системы. Цепью питания такой конструкции антенн является копланарная волноводная линия.

Постановка задачи

Была спроектирована дисконусная антенна, геометрическая структура которой представлена на Рис. 1. Расчет проводился для диапазона частот от 1 ГГц до 5 ГГц $f_{мин}$= 1 ГГц, $f_{макс}$= 5 ГГц, f_0 = 3 ГГц (центральная частота). Расчет геометрической структуры антенны проводился по следующим формулам [2]:

1. диаметр диска $D_d = K\frac{\lambda_{макс}}{4}$, где$K = \frac{f_{min}}{f_0} \Rightarrow D_d = 52\, мм$;

2. длина конуса $H = \frac{\lambda_{макс}}{4} = 75\, мм$;

3. был выбран оптимальный угол между образующей и осью конуса $\theta = 30°$;

4. фидер питания представляет собой коаксиальный кабель диаметром $2R = 0{,}6\, мм$;

5. расстояние между диском и конусом $S = 0{,}2\, мм$;

6. был выбран оптимальный диаметр верха конуса` $D_{c2} = 3\, мм$;

7. диаметр основания конуса $D_{c1} = D_{c2} + 2H sin\theta = 77\, мм$.

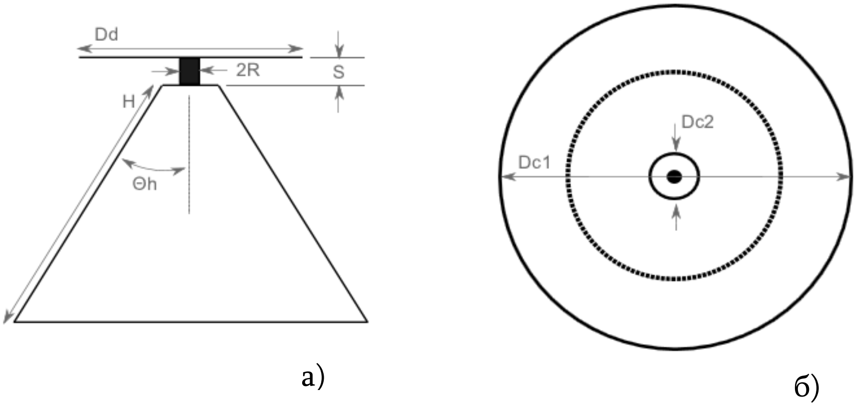


Рис. 1. Структура дисконусной антенны: а) сбоку; б) сверху.

На Рис. 2 представлена копланарная дисконусная антенна. Излучающая поверхность установлена на диэлектрике марки FR4 с диэлектрической проницаемостью $\varepsilon_r = 4{,}6$ и толщиной $h = 1{,}6$ *мм.* Размеры диэлектрика $W_д = 49$ *мм,* $L_д = 53$ *мм*; диаметр диска $a = \frac{D_д}{2} = 24{,}8$ *мм.* Цепь питания копланарной волноводной линия с волновым сопротивлением 50*Ом*, толщиной $w = 1{,}5$*мм*, боковая длина плоскости заземления$H = \frac{\lambda_{макс}}{4\sqrt{\varepsilon_{эф}}} = 47{,}84$мм; был выбран оптимальный угол между образующей и осью конуса $\theta = 30°$.

Результаты исследования

Проектирование реализовано в программной среде FEKO [3].

На Рис. 3 представлен график зависимости коэффициента стоячей волны по напряжению (КСВН) дисконусной антенны от частоты. Как можно заметить из графика, в диапазоне частот 1,25....6 ГГц, КСВН меньше 2.

На Рис. 4 представлена диаграмма направленности (ДН) антенны для частот 1,25; 2; 3 и 4 ГГц. ДН симметрично всенаправленна только

в диапазоне частот 1,25...4 ГГц; начиная с 4ГГц ДН антенны искажается. Коэффициент усиления (КУ) антенны в диапазоне частот 1,25...4 ГГц в направлении главного лепестка колеблется в диапазоне 0,5...1,7дБ.

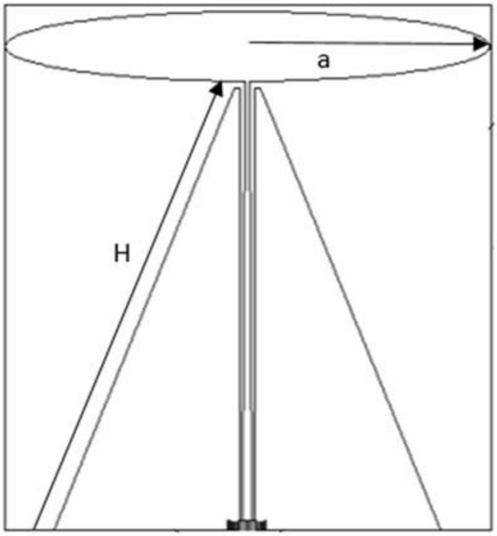


Рис. 2. Структура копланарной дисконусной антенны.

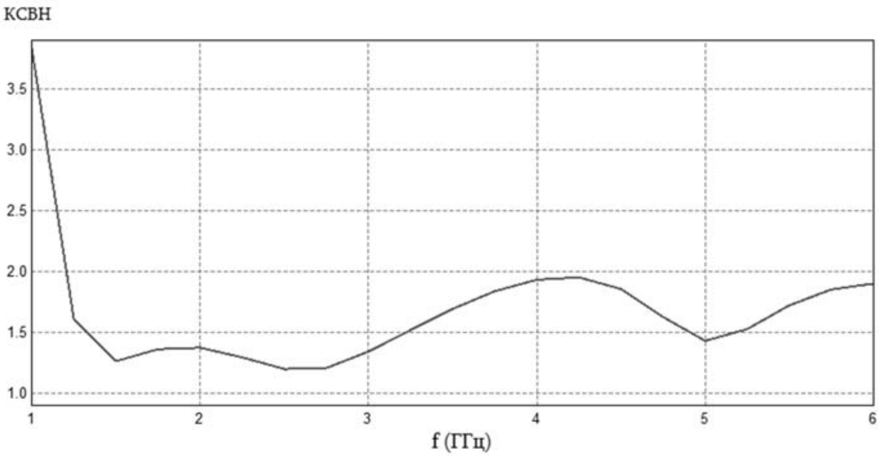


Рис. 3. Зависимость КСВН дисконусной антенны от частоты.

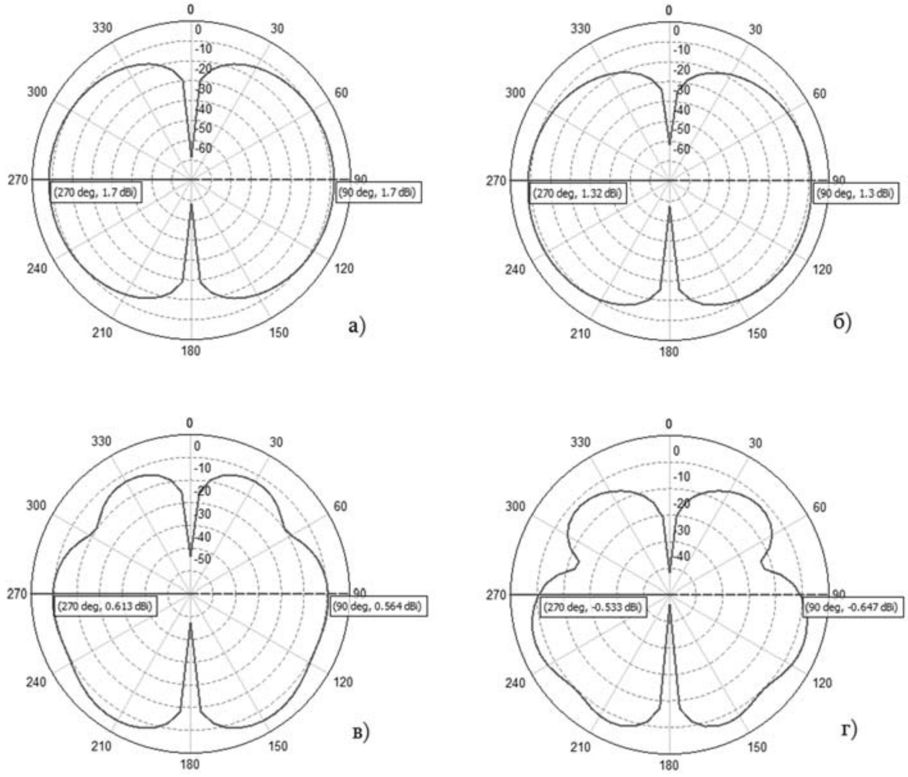


Рис. 4. ДН дисконусной антенны для частот:
а) 1,25 ГГц; б) 2 ГГц; в) 3 ГГц; г) 4 ГГц.

На Рис. 5 представлена зависимость КСВН копланарной дисконусной антенны от частоты. Как можно заметить из графика, в диапазоне частот 1,75...5,27 ГГц КСВН меньше 2.

На Рис. 6 и 7 представлены ДН антенны, соответственно, в плоскостях Е и Н для частот 1,75; 2,75; 3,75, и 5 ГГц. ДН всенаправленна только в диапазоне частот 1,75...5 ГГц, начиная с 5 ГГц ДН антенны, искажается. КУ антенны в вертикальной плоскости колеблется в диапазоне 0,1...2,1 дБ, а в горизонтальной плоскости: -0,1...1,57 дБ.

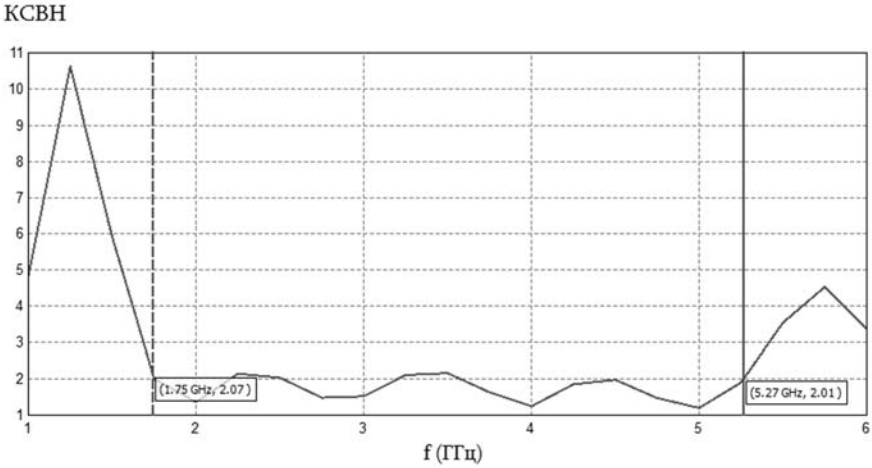


Рис. 5. Зависимость КСВН-копланарной дисконусной антенны от частоты.

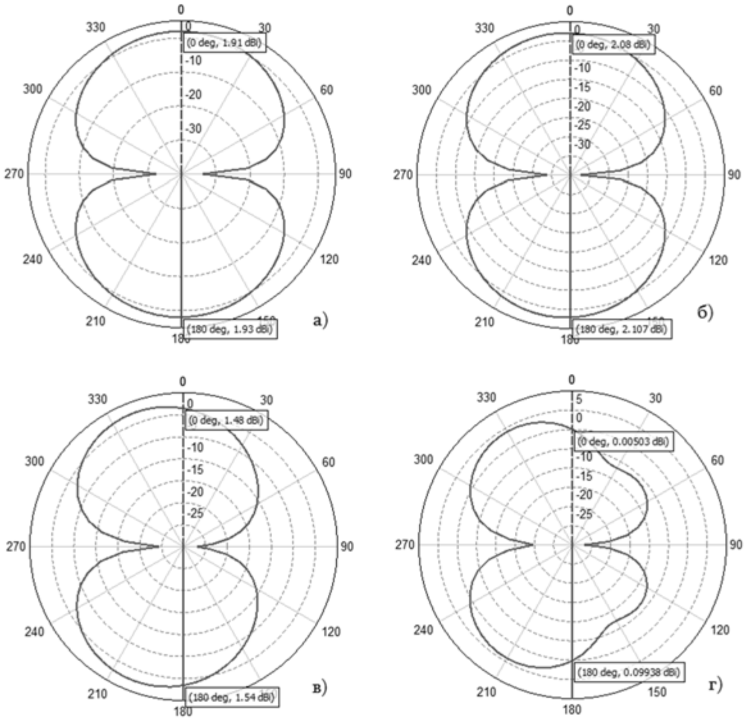


Рис. 6. ДН копланарной дисконусной антенны в вертикальной плоскости
для частот: а) 1,75; б) 2,75; в) 3,75; г) 5 ГГц.

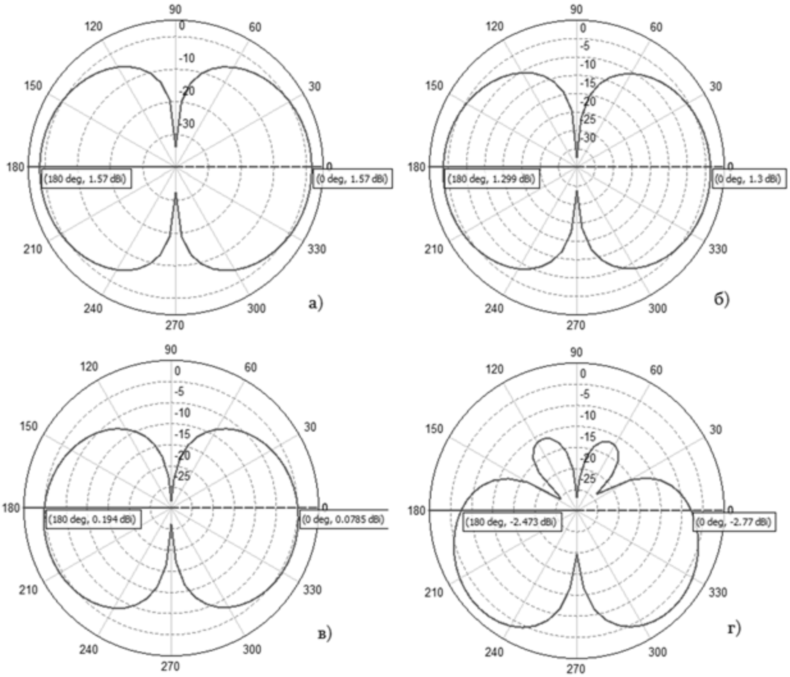


Рис. 7. ДН копланарной дисконусной антенны в горизонтальной плоскости для частот: а) 1,75; б) 2,75; в) 3,75; г) 5 ГГц.

Заключение

1. Разработана и исследована дисконусная антенна, на основе которой была создана копланарная дисконусная антенна с улучшенными параметрами.

2. В диапазоне частот 1,75...5 ГГц КСВН меньше 2.

3. КУ в направлении максимального излучения в диапазоне частот 1,75…5 ГГц в вертикальной плоскости колеблется 0,1…2,1 дБ, а в горизонтальной плоскости: 0,1...1,57 дБ.

4. Данная антенна применяется в радиотехнических системах, таких как стандарты Bluetooth, WIFI, в системах глобального позиционирования, в радиолокации и в антенных измерительных системах.

5. Преимущество данной антенны: ДН симметрична на более широком диапазоне частот, малые габаритные размеры легко интегрируются в радиотехнические системы.

ЛИТЕРАТУРА

1. 1.*Constantine A. Balanis.* Modern Antenna Handbook. -1st edition, John Wiley & Sons-2008. 409p.
2. *Tiwari A., Ashish Kr. Roy* Antenna for RFI Monitoring // researchgate.com.
3. 3.*Atef Z. Elsherbeni, Nayeri P., Reddy C.J.* Antenna Analysis and Design Using FEKO Electromagnetic Simulation Software //SciTech Publishing, Edison, NJ. 2014.

DESIGNING OF CPW DISCONE ANTENNA

A. Stepanyan, S. Eyramjyan

ABSTRACT

With the development of telecommunications systems,usage of omnidirectional antennas has become increasingly relevant today. The current frequency bandwidth is increasing so there is a need to create new antennas with a wideband frequency range. A discone antenna wasexplored and developed on the basis of which a coplanar antenna was made. The design was implemented in FEKO software environment. The calculation results are presented in graphs. The computational results of the two antennas are compared.

Keywords: omnidirectional antenna, wideband antenna, discone antenna, FEKO software environment.

УДК 621.317.7.023

Поступила: 19.04.2020г.
Сдана на рецензию: 23.04.2020г.
Подписана к печати: 29.04.2020г.

ТЕСТИРОВАНИЕ ИНТЕГРАЛЬНОЙ СХЕМЫ АВТОМОБИЛЬНОГО РАДАРА НЕПРЕРЫВНОГО ИЗЛУЧЕНИЯ С ЧАСТОТНОЙ МОДУЛЯЦИЕЙ СИГНАЛА С ЧАСТОТОЙ В 77 ГГц

Л.Р. Мовсисян, Г.А. Цатурян, С.В. Антонян

Национальный политехнический университет Армении

lia.movsesyan@gmail.com, grigor.tsaturyan99@gmail.com, samwellantonyan@gmail.com

АННОТАЦИЯ

Как известно, в автомобильных радиолокационных системах широко используется принцип непрерывного излучения с частотной модуляцией сигнала (FMCW). В основе идеи радара FMCW лежит генерация сигнала с линейно изменяющейся частотой. Решение об определении расстояния до объекта принимается на основании частотной разницы между генерированным и отраженным от объекта сигналами. Для однозначного определения скорости используется информация, полученная от нескольких генерированных сигналов с линейно изменяющейся частотой [1].

В рамках данной статьи предлагается система тестирования, которая дает возможность проводить скалярные и векторные измерения в частотном диапазоне 76–77 ГГц. Была протестирована являющаяся основой радара интегральная схема (ИС) производства фирмы “Analog Devices International (ADI)”. Тестирование было проведено с целью предоставления фирме-производителю технических характеристик ИС для сравнения их с ожидаемыми результатами. В

итоге тестирования ИС были получены амплитудно-частотные характеристики (АЧХ) передающих трактов. Также была предложена система тестирования, с помощью которой возможно измерить разницу в фазовых набегах сигнала в линиях передачи ИС. Преимущество предлагаемого способа тестирования заключается в том, что измерения можно проводить с помощью одноканального анализатора с использованием единого тактового генератора для анализатора и ИС.

Ключевые слова: Тестирование интегральной схемы автомобильного радара, FMCW радар, измерение разницы в фазовых набегах сигнала одноканальным анализатором.

Введение

Системы с различными видами частотной модуляции (ЧМ) находят широкое применение в различных радиотехнических устройствах. Особое место среди ЧМ систем занимают системы, которые используются в ситуациях с быстроменяющимися процессами, характерными для разных применений, в том числе в измерительных и локационных системах ближнего действия, работающих обычно в режиме непрерывного излучения, в широкополосных цифровых приемниках.

В ряде случаев анализ таких систем тесно связан с их динамическими свойствами, когда необходимо учитывать быстрые изменения параметров наблюдаемых объектов, например, быстрое движение автомобилей, двигающихся по пересекающимся траекториям. В таких ситуациях анализ переходных и быстроменяющихся процессов и сигналов в системе является принципиальным. Тестирование ИС таких систем должно быть одновременно точным, эффективным и использующим как можно меньше ресурсов.

Принцип работы FMCW радара

FMCW радар передает сигнал, частота которого линейно повышается в зависимости от времени (Рис. 1). Такой сигнал называется *линейно-частотно модулированным* (ЛЧМ) [2]. ЛЧМ характеризуется

начальной частотой f_c, полосой качания B, периодом частотной модуляции T_c и крутизной S, характеризующей скорость изменения частоты.

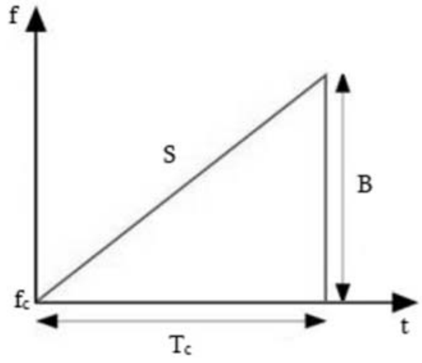


Рис. 1. ЛЧМ-сигнал.

Вид ЛЧМ сигналов, передаваемых (TX) и отраженных от объекта (RX)представлен на Рис. 2.

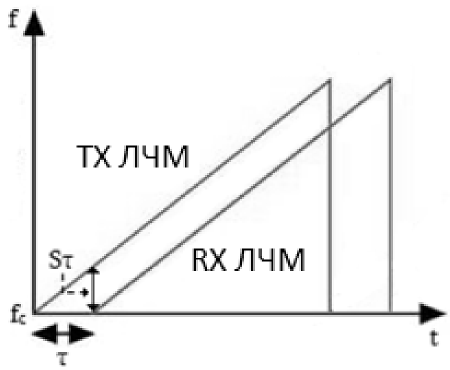


Рис. 2. Передаваемый и отраженный ЛЧМ-сигналы.

Отраженный сигнал является вариантом передаваемого сигнала, задержанным на τ. Расстояние d до объекта определяется разницей частот F передаваемого и отраженного сигналов:

$$d = \frac{Fc}{2S}$$

где c – скорость света [2].

Одновременно для измерения скорости многочисленных объектов в FMCW радаре используется 2D – метод прямого преобразования Фурье (2D-FFT) [3].

Постановка задачи

Посредством предлагаемой системы тестирования провести измерения АЧХ передающих трактов ИС производство фирмы ADI в диапазоне частот 76–77 ГГц. Используя предлагаемый способ тестирования, показать возможность измерения разницы в фазовых набегах сигнала в линиях передачи ИС с помощью одноканального анализатора, в то время, как при использовании других методов измерения необходимо использовать 2 анализатора, что уже представляет из себя большие расходы. С целью определения степени точности предлагаемого метода провести его сравнение с взаимно корреляционным методом. Предоставить полученные результаты тестирования ИС фирме-производителю для сравнения с ожидаемыми результатами. Ожидаемые результаты: неравномерность АЧХ составляет ±1 дБ, а фазовый сдвиг между передающими путями ±3°.

Сравнение предлагаемого метода измерения разницы в фазовых набегах сигнала в двух линиях передачи с методом взаимной корреляции

Блок-схема измерительной системы при использовании метода взаимной корреляции будет иметь вид, отображенный на Рис. 3 [4]. Для измерения разницы в фазовых набегах между сигналами генератора 1 и генератора 2, необходимо их подсоединить, соответственно, к анализатору 1 и анализатору 2. Из этого следует, что необходимо использовать 2 анализатора. Эти анализаторы должны будут использовать единый гетеродин, в противном случае – прервется когерентный

режим работы анализаторов, что, в свою очередь, приведет к неточностям в измерениях.

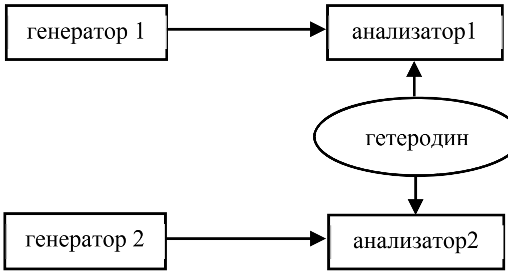


Рис. 3. Блок-схема взаимно корреляционного метода измерения разницы в фазовых набегах сигнала между двумя передающими путями.

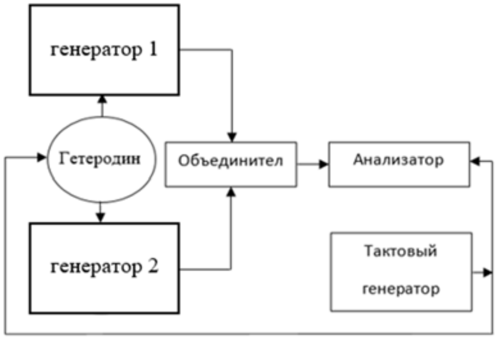


Рис. 4. Блок-схема предлагаемого метода измерения разницы в фазовых набегах сигнала между двумя передающими путями.

Блок-диаграмма предлагаемой системы тестирования показана на Рис. 4. В данной системе анализатор и генераторы используют единый тактовый генератор, с помощью которого обеспечивается когерентный режим работы системы. Для измерения разницы в фазовых набегах сигнала, необходимо обеспечить продолжительную работу генераторов. Для реализации данной задачи с помощью анализатора

принимается исходящий сигнал генератора 1, после чего данный канал закрывается и открывается канал генератора 2. Разница мгновенных значений фаз принимаемых сигналов с генератора 1 и генератора 2 выдает значение разницы в фазовых набегах сигнала между генераторами.

Результаты исследования

На Рис. 5 представлена система тестирования. Основные управляемые узлы объединены в приборе Chassis NI PXIe-1085. PXIe-8880 контроллер контролирует ZCU-102 Xilinx Ultrascale+ платформу, которая, в свою очередь, является контролирующим звеном для ИС. NI PXIe-6674T является источником тактового сигнала для ИС, NI PXIe-5840 и mmRH-3608. С помощью NI PXIe-5840 и mmRH-3608 калиброванных частотных преобразователей возможно выполнять точные измерения.

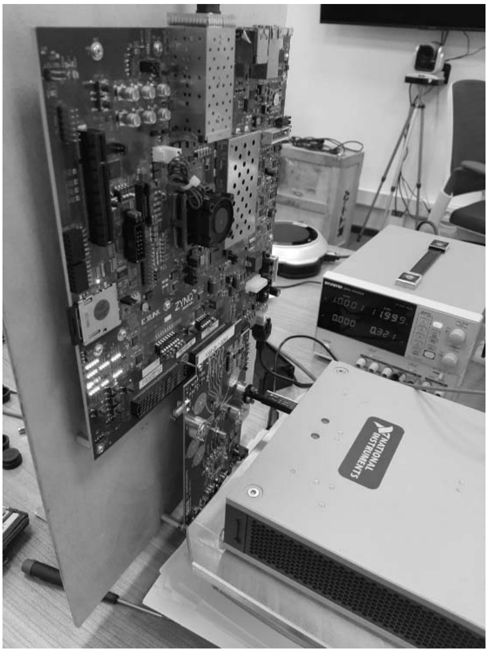


Рис. 5. Система тестирования.

На Рис. 6 приведены полученные результаты АЧХ передающих трактов ИС при частоте 76–77 ГГц.

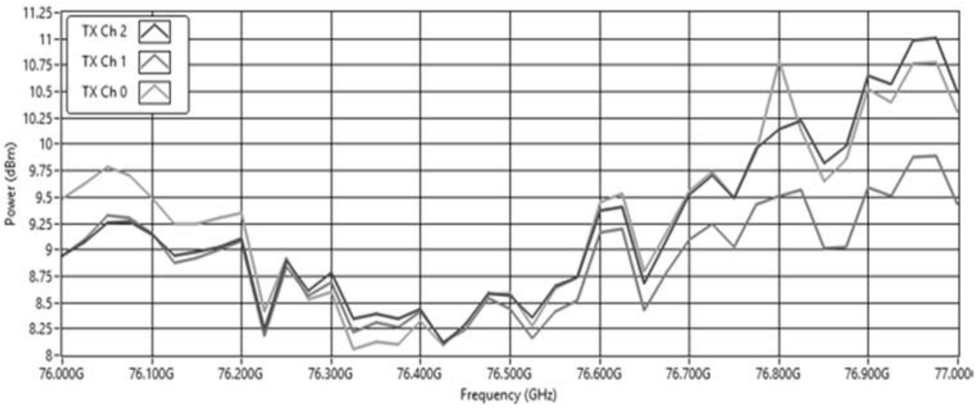


Рис. 6. АЧХ передающих трактов ИС в частотном диапазоне 76–77 ГГц.

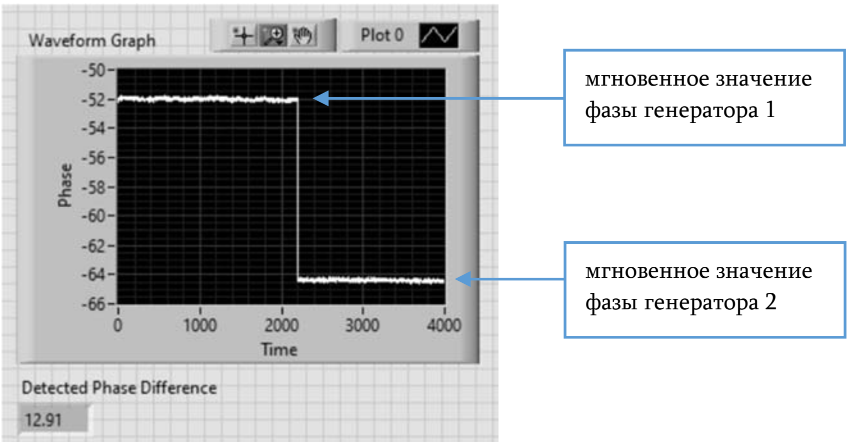


Рис. 7. Разница в фазовых набегах сигнала между двумя передающими путями измеренная предлагаемым методом.

Для удостоверения точности метода измерения разницы в фазовых набегах сигнала были проведены сравнительные расчеты на частоте 1 ГГц с помощью предлагаемого и корреляционного методов. На Рис. 7 и Рис. 8 показаны результаты, полученные с помощью вышеуказанных методов. Результаты измерений показали идентичность методов, так как в обоих случаях было зафиксировано одинаковое значение разницы в фазовых набегах сигнала, которое составляет 12,91° с точностью 0,07°. Следовательно, предлагаемый метод можно использовать для тестирования ИС.

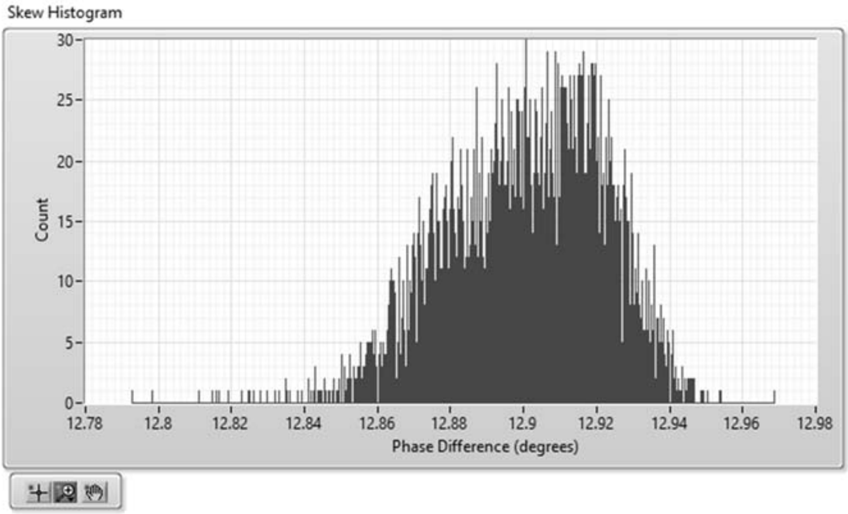


Рис. 8. Разница в фазовых набегах сигнала между двумя передающими путями измеренная взаимно корреляционным методом.

На Рис. 9 показана разница в фазовых набегах сигнала между передающими путями ИС, измеренная предлагаемым методом. Как видно, значение разницы в фазовых набегах сигнала не превосходит 2,69°, что рассчитывается как разница между мгновенным значением

фазы сигнала второго передающего тракта и мгновенным значением фазы сигнала первого передающего тракта ИС.

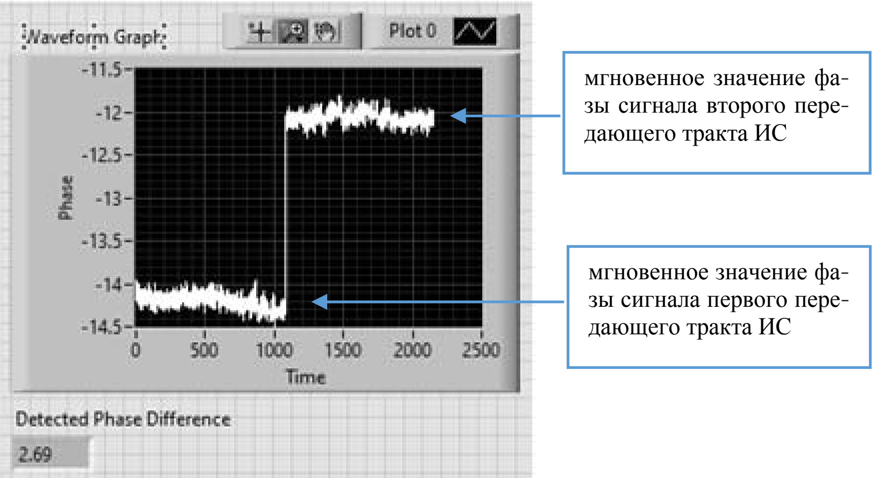


Рис. 9. Фазовый сдвиг между двумя передающими путями ИС.

Заключение

Протестирована ИС автомобильного радара, предоставленная фирмой-производителем “Analog Devices International”. Контролирующим звеном ИС являлась ZCU-102 Xilinx Ultrascale+ платформа, а в качестве тактового генератора использован NI PXIe-6674T. Прием необходимых частот был обеспечен векторными приемопередатчиками NI PXIe-5840 и mmRH-3608. Предложен метод измерения фазовых набегов сигнала между передающими путями, который дает возможность проводить измерения с использованием одного анализатора. Проведено сравнение предлагаемого метода измерения с известным взаимнокорреляционным методом для определения степени точности предложенного метода. В ходе тестирования измерены АЧХ передающих трактов ИС и сделаны выводы о том, что неравномерность АЧХ превышает ожидаемое отклонение в 1 дБ, а фазовый набег сигнала между путями ИС не превосходит 2,69°.

ЛИТЕРАТУРА

1. *Winkler, V.* Range Doppler Detection for automotive FMCW Radars// IEEE. 2007.166p.
2. *Iovescu, C., Rao, S.* The fundamentals of millimeter wave sensors // http://www.ti.com/lit/wp/spyy005/spyy005.pdf
3. *Song, M., Lim, J., Shin, D-J.* The velocity and range detection using the 2D-FFT scheme for automotive radars// IEEE International Conference on Network Infrastructure and Digital.2014.
4. *Liu, Y.-Z., & Zhao, B.* Phase-shift correlation method for accurate phase difference estimation in range finder //https://www.ncbi.nlm.nih.gov/pubmed/25967339 ?fbclid=IwAR0d7ZbvYPqDEdZQ6VSAJ9n_iQRKLVanFAurdxZZs02NwGRG2 ioA7-RIdNY

TESTING OF 77GHz FREQUENCY MODULATED CONTINUOUS WAVE AUTOMOTIVE RADAR'S INTEGRATED CIRCUIT

L. Movsisyan, G. Tsaturyan, S. Antonyan

ABSTRACT

The FMCW principle is widely used in automotive radar systems. The idea behind the FMCW is to create a linear frequency signal. The decision to remove the object is made on the basis of the frequency difference between the generated and reflected signals from the object. Information processed from several generated signals with linearly varying frequency is used to determine the speed uniquely [1]. The article proposes testing system that makes possible to do scalar and vector measurements in the frequency range of 76–77 GHz. The radar integrated circuit (IC) manufactured by Analog Devices International (ADI) was tested. Testing was carried out in order to provide the manufacturer with the technical characteristics of the IC to compare them with the expected. As a result of testing the IC, the amplitude-frequency response of the transmitting paths were obtained. There is also proposed a test system which will give an ability to measure phase differences of the signal in the transmission lines of the IC. The advantage of the proposed testing method is that measurements can be carried out using a single-channel analyzer with sharing same clock for the analyzer and IC.

Keywords: Testing of an integrated circuit of automotive radar, FMCW radar, Signal phase difference measurements by a single-channel analyzer.

УДК621.3.049.77

Поступила: 25.05.2020г.
Сдана на рецензию: 08.05.2020г.
Подписана к печати: 15.05.2020г.

LOW INPUT CAPACITANCE DYNAMIC LATCH COMPARATOR FOR HIGH SPEED OPERATION

H. Aghayan[1], D. Manukyan[1], M. Grigoryan[2]

[1]*Yerevan State University faculty of Radiophysics, Department of VLSI Design*
[2]*Synopsys Armenia Educational Department*

haik.aghayan@gmail.com, manukyan.davit6139@gmail.com, manvelg@synopsys.com

ABSTRACT

The paper presents high speed double-tail dynamic latch comparator with low input capacitance which allows the preamplifier to drive a high frequency signal. The main idea is to add additional transistors in parallel with input transistors. Circuits are designed with SAED 14nm technology and are simulated with Synopsys HSpice simulation tool. The speed of the comparator is increased by 57.8%.

Keywords: comparator, dynamic latch, single-tail dynamic latch, double-tail dynamic latch, over corner variation, low input capacitance, high speed.

Introduction. Comparators are one of the most frequently used blocks in integrated circuits(IC). They present themselves as a simple one bit analog to digital converters which compare two voltages or two currents and give a digital output. Comparators are used in all ADC applications and performance of ADC mostly depends on comparator performance. Also comparators are used in high speed data communication interfaces, where

data is transferred by analog differential signal and there is need to compare two voltages and obtain a full scale digital signal. They are used in memory sense amplifiers too. There exist two types of comparators: non-clocked and clocked. Non-clocked comparators are amplifiers with a very high gain thanks to which their outputs reach their highest value even with small voltage difference at input nodes. Non-clocked comparators are slower, because it is very hard to build a high-speed and high-gain comparator. They also consume static power, which does not satisfy the high-speed and low-power requirements of today's application. Today's high-speed data communication interfaces require comparators with high accuracy and low propagation delay. Clocked comparators use strong positive feedback to increase the small difference between input signals due to which it demands reset after each comparison, because values of voltages generated by feedback tend to remain. In the reset phase the positive feedback turns off which allows resetting output values of the comparator. Reset and comparison phases are controlled by clock signal.

Besides dynamic circuits containing regenerative latch which represents the decision making circuit of comparator, comparators also consist of a pre-amplifier and output buffer. Output buffers keep their previous values in reset stage and buffer output values of decision making circuit in comparison stage. Usually they are made from conventional Set-Reset latch, from self-biased differential amplifier or simple flip-flop. This article does not focus on output buffers. The pre-amplifier amplifies the input signal to increase the sensitivity of the comparator; also the pre-amplifier works as a buffer and fixes input common mode of the decision making circuit. Even if the circuit designer does not need to increase the sensitivity of decision making circuit pre-amplifiers exist, because usually signals are buffered many times in integrated circuits. Because of that, the impact of the decision making circuit on the pre-amplifier cannot be neglected. Such an impact is called kickback noise. Reducing kickback noise is one of the purposes of this article. The three-stage diagram of the comparator is shown in Figure 1.

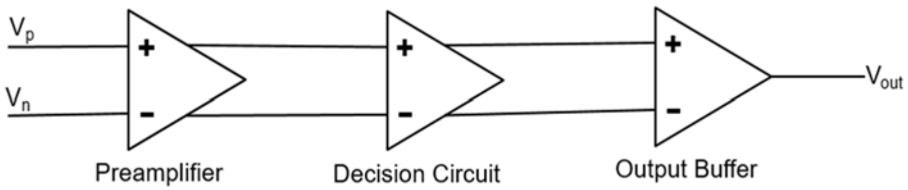


Fig. 1. 3 Stages of comparator.

Conventional topologies. The core of the clocked comparators is dynamic latched circuits. There are two common types of dynamic latched comparators` single-tail and double-tail comparators. Conventional single-tail dynamic latch is shown in Figure 2. Double-tail is shown in Figure 3.

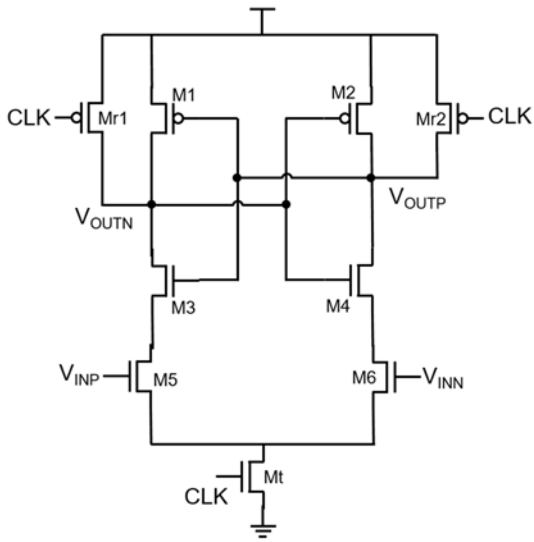


Fig. 2. Conventional single-tail dynamic latch comparator.

Single-tail dynamic latch. When CLK=0, transistors Mr1 and Mr2 are open connecting Voutn and Voutp to VDD. Due to values of Voutn and

Voutp, resetting to high voltage is done. This stage is called reset stage. After the reset stage, when CLK=1, transistors Mr1 and Mr2 are closed and transistor Mt is open. Due to high values of nodes Outn and Outp, transistors M3 and M4 are open. Decreasing rate of voltage of Outn depends on the current flowing through transistor M5 and decreasing rate of voltage Outp depends on the current flowing through transistor M6. If voltage at node of INP is greater than voltage at INN, the current flowing through transistor M6 is greater than the current flowing through transistor M5 due to which Voutn decreases faster. When Voutn is low enough, transistor M3 begins to close and transistor M1 begins to open which pulls up Voutn. That means that after the comparison stage if $V_{INP}>V_{INN}$, $V_{OUTP}=1$ $V_{OUTN}=0$.

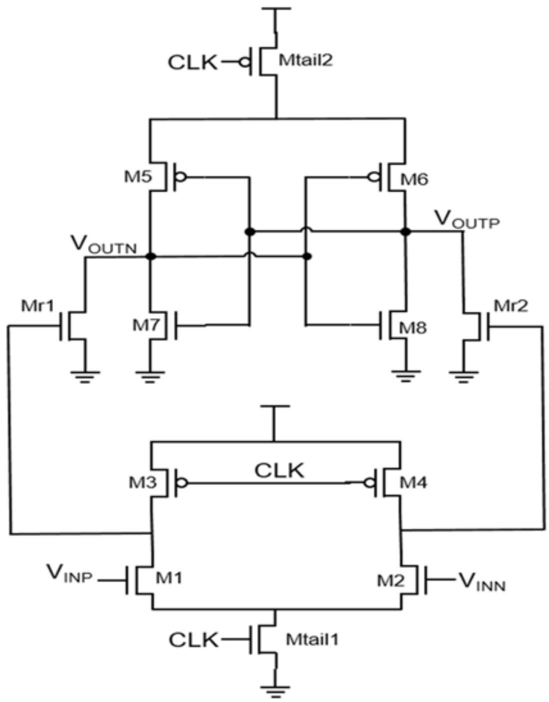


Fig. 3. Conventional double-tail dynamic latch comparator.

Double-Tail dynamic latch. There are also double-tail comparators. A conventional double-tail comparator is shown in Figure 2. When CLK=0, transistors M3 and M4 are open and transistors Mtail1 and Mtail2 are closed. Due to that voltages at gates ofMr1 and Mr2 are becoming equal to VDD, which opens transistors MR1 and MR2 and Outp and Outn are resetto the ground. When CLK=1, transistors Mtail1 and Mtail2 are open and transistors M3 and M4 are closed. Due to that gate capacitances of Mr2 and Mr1 begin to discharge when they are discharged enough to close transistors MR1 and MR2 regenerative latch is triggered. Voltages at outputs of regenerative latch depend on which transistor closed first due to which if V_{INP} is higher than V_{INN}, transistor MR2 closes first and V_{OUTP} becomes high after the regeneration process V_{OUTP}=1 and V_{OUTN}=1. If voltage at node INN is higher after the regeneration stage, V_{OUTN}=1 and V_{OUTP}=0.

There already exist many types of single and double-tail comparators. In Reference [1] comparisons of some comparators have been conducted. Reference [2] presents a low-offset and high-load drivability dynamic latched comparator, which is reached by adding inverters drains of input transistors and gates of regenerative latch. In Reference [3] the speed of regenerative latch is enhanced by adding additional transistors in latch circuit. Reference [4] mentions a two-stage dynamic latch comparator with enhanced speed and reduced power consumption which is reached by adding two cross-coupled transistor loads and stacking switches in input stage. In reference [6] a low-power high-speed dynamic latched comparator is implemented with NAND latch in 90nm technology. As mentioned above, comparators are widely used in ADC architectures. Reference [7] addresses a low-offset comparator for high-speed ADCs. Reference [8] shows the use of comparator in SAR ADC architectures. Reference [9] presents a comparator for asynchronous SAR ADC and Reference [10] shows a comparator for Flash ADCs architectures which was improved by enhancing positive feedback with additional transistors.

In both cases the overall propagation delay consists of two delays: timerequired for the regenerative latch to trigger $t_{discharge}$ and timerequired to generate rail-to-rail voltage levels for regenerative latch$_{latch}$.

$$t_d = t_{discharge} + t_{latch}$$

Time $t_{discharge}$ depends on the resistance of input transistors and tail transistor and capacitances which must discharge until regenerative latch triggers. Time t_{latch} depends on the transconductance of transistors that the regenerative latch contains.

Reference 5 presents some calculations of delay time comparator. Here are the results:

$$t_{discharge} \cong \frac{2C_L|V_{thp}|}{I_{tail}}$$

$$t_{latch} = \frac{C_L}{g_{m,eff}} \times ln\left(\frac{\Delta V_{OUT}}{\Delta V_0}\right)$$

$$\Delta V_0 = |V_{thp}|\left(1 - \frac{I_2}{I_1}\right)$$

Where C_L is capacitance at output node, V_{thp} is the threshold voltage of p-type transistor, $g_{m,eff}$ is the effective transconductance of back-to-back inverters M5-M8, I_1 and I_2 are currents flowing through input transistors, ΔV_{OUT} is voltage between output nodes at time $t_{discharge}+t_{latch}$ and ΔV_0 is voltage between output nodes at time $t_{discharge}$. The difference between single-tail and double-tail comparators is that for the single-tail in $t_{discharge}$ and t_{latch} equations C_L is the same quantity, but for the double-tail comparator in $t_{discharge}$ equation C_L is gate capacitance of Mr1 and Mr2.

In case of single-tail dynamic latched comparator decreasing them is opposite problems, because the transconductance of regenerative latch increases when their sizes increase, but when sizes increase capacitances also increase and discharge time is also increased. But for the case of double-tail comparator decreasing $t_{discharge}$ and $t_{latch}$is not opposite problems, because discharge time depends on capacitances of MR1 and MR2 and resistances of input transistors and tail transistor; latch time depends on parameters of transistors M7, M8, M9 and M10. Due to that propagation delay can be minimized without trade-offs between discharge and latch

delays. Also to obtain same speed, single-tail dynamic latch must discharge faster than double-tail, because gate area of MR1 and MR2 can be smaller, which decreases kickback noise.

It can be deduced that the double-tail dynamic latched comparator is more suitable for low input load applications than the single-tail comparator. The following presents another topology of the double-tail comparator which is a small load for the preamplifier thanks to which it can operate with more high-frequency signals and generate low kickback noise.

Proposed comparator. The scheme of the proposed comparator is shown in Figure 4.

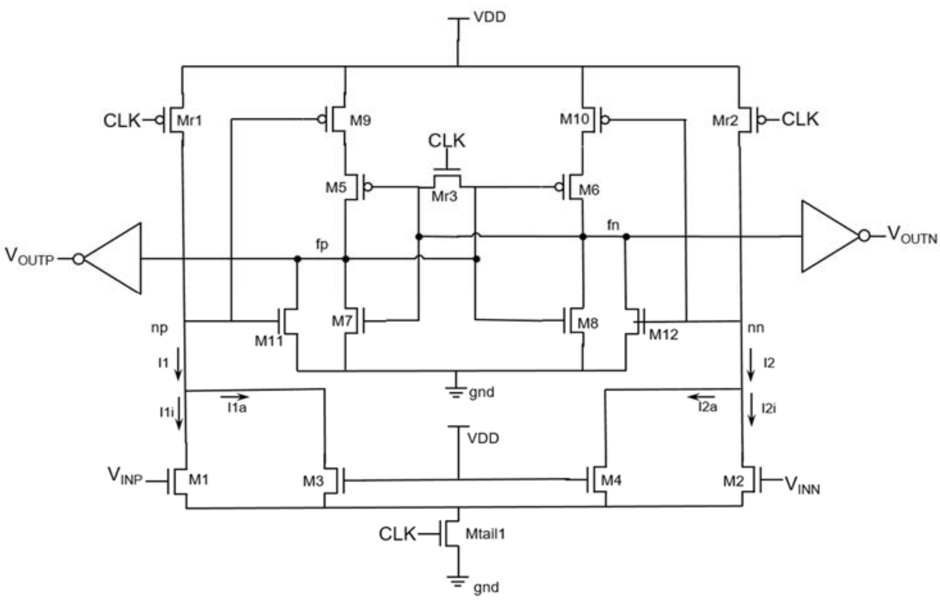


Fig. 4. Proposed double-tail dynamic latch comparator.

This comparator is an improved version of the double-tail dynamic latch comparator. Instead of transistor Mtail2 transistors M9 and M10are used. As mentioned earlier during the reset phasevol tages at nodes np and nn increase which closes M9 and M10 which disconnects the regenerative

latch from VDD. In case of a conventional double-tail dynamic latched comparator the following function was implemented with transistor Mtail2. Transistor Mr3 connects nodes fp and fn which helps to reduce the accumulative offset. The accumulative offset acquires, because after comparison stage one of node fp and fn has a high voltage value and the other one has a low voltage value. In the reset stage the voltage at the node which had a high voltage value decreases quickly; therefore, due to charge injection, the voltage at another node slightly decreases which produces offset. The purpose of transistors M3 and M4 is to increase the comparator's speed and decrease the load for the preamplifier.

Simulations and Results. Simulations are done with Synopsys HS pice simulation tool. Circuits are designed with SAED 14nm Fin FET technology. Waveforms are edited with Synopsys CS cope viewer. VDD is set to 0.9V.

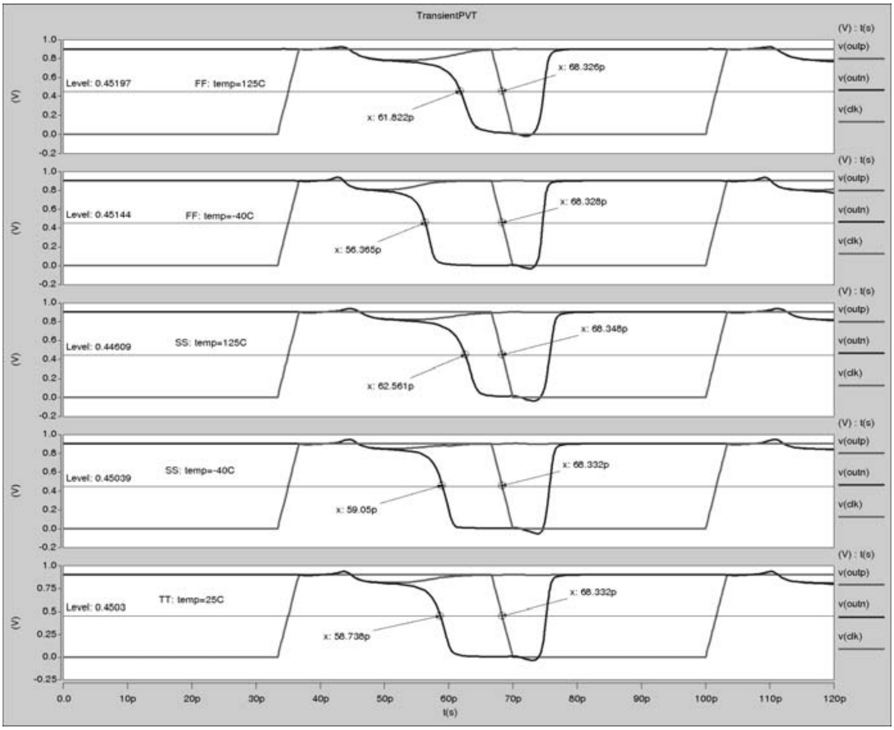


Fig. 5. Over corner variation of the proposed comparator.

To get information about how fast a comparator is, it must be tested at its worst corner. Figure 5 shows the operation of a comparator of different corners. Input voltage difference is 4mv, and input common mode is 0.7V. Clock frequency is set to 15GHz. Graphs show time when the clock and negative output signals cross VDD/2. The comparator must generate proper output in comparison time. Due to that there is shown the time when the comparison stage is over and the time when the output is valid. It can be seen that the worst corner is SS temp=125C.

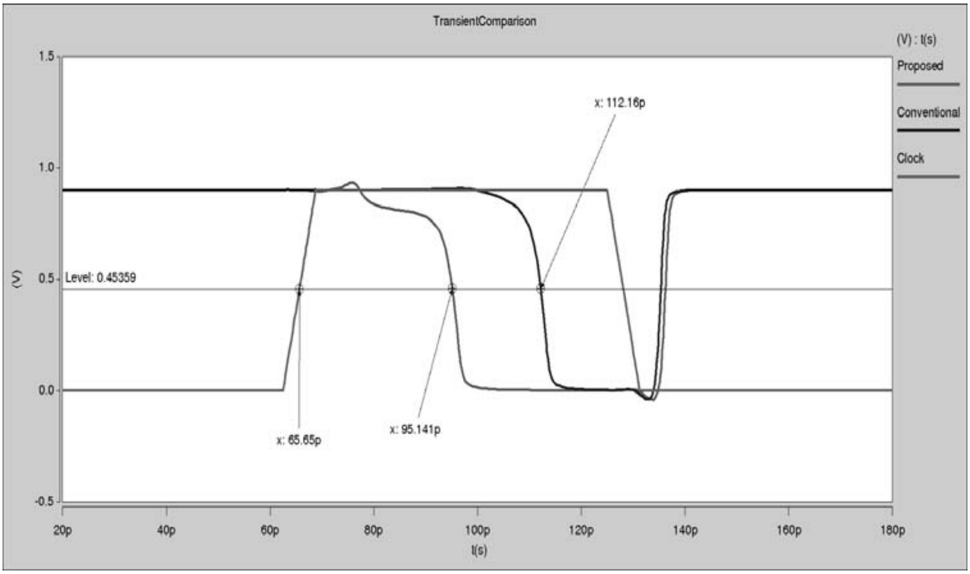


Fig. 6. Comparison of the proposed and conventional comparators.

Figure 6 shows the comparison of the conventional comparator and the proposed comparator. To get the comparison sizes of input right, the transistors are same in both cases. Input voltage difference and common mode are the same too. The clock frequency is set to 8GHz.

It can be seen that propagation delay for the proposed comparator is 29.46p and for the conventional comparator it is 46.49p which is 57.8% slower.

Conclusion.A simple method was implemented to decrease the input capacitance without affecting the operation speed of the comparator. The method is shown for the double-tail dynamic latch comparator, but it is also applicable for single-tail.

REFERENCES

1. *Moni D., Jisha P.* High Speed and low-power dynamic Latch comparator // International Conference on Devices, Circuits and Systems (ICDCS). 2012 IEEE.
2. *Jeon H., Kim Y.*A CMOS low-power low-offset and high-speed fully dynamic latched comparator // SOC Conference, IEEE International.
3. *Jain R., Dubey A., Varshney V., Nagaria R.* Design of low-power high-speed double-tail dynamic CMOS comparator using novel latch structure // Conference on Electrical Computer and Electronics (UPCON). 2017 IEEE.
4. *Varshney V., Kumar A., Dubey A., Singh P., Nagaria R.*A High-Speed Energy-Efficient CMOS Dynamic Latch Comparator for Low-Voltage Applications // Conference on Electrical Computer and Electronics (UPCON). 2019 IEEE.
5. *Prasanthi B., Pushpalatha P.* Design of Low-Voltage and Low-Power inverter based Double-tail Comparator // International journal of engineering Research and General Science Volume 2, Issue 5. August-September 2014.
6. *Rabbi F., Das S., Hossain Q., Pathan N.* Design of a Low-Power Ultra High Speed Dynamic Latched Comparator in 90-nm CMOS Technology // International Conference on Computer, Communication, Chemical, Material and Electronic Engineering (IC4ME2). 2018 IEEE.
7. *Yongheng G., Wei C., Tiejun L., Zongmin W.*A Novel 1GSPS Low offset Comparator for high speed ADC // Fifth International Joint Conference on INC, IMS and IDC. 2009.
8. *Yu. L., Zhang J., Wang L.*A 12-bit Fully Differential SAR ADC with Dynamic Latch Comparator for Portable Physiological Monitoring Applications // 4th International Conference on Biomedical Engineering and Informatics (BMEI). 2011.

9. *Bekal A., Joshi R., Goswami M., Singh B., R. and Srivatsava A.* An improved Dynamic Latch Based Comparator for 8-bit Asynchronous SAR ADC // Computer Society Annual Symposium on VLSI. 2015 IEEE.
10. *Kazemina S., Shino O., Haghighi E., Hadidi K.* Improved Single-Stage Kickback-Rejected Comparator for High Speed and Low Noise Flash ADC.

КОМПАРАТОР С НИЗКОЙ ВХОДНОЙ ЕМКОСТЬЮ И С ДИНАМИЧЕСКИМ ТРИГЕРОМ ДЛЯ ВЫСОКОСКОРОСТНОЙ РАБОТЫ

А.А. Агаян, Д.А. Манукян, М. Григорян

АННОТАЦИЯ

В данной статье представлен высокоскоростной, или двухкорпусный, динамический компаратор с низкой входной емкостью, позволяющий предусилителю управлять высокочастотным сигналом. Основная идея заключается в добавлении дополнительных транзисторов параллельно с входными транзисторами. Схемы спроектированы с использованием технологии SAED 14nm и моделируются с помощью инструмента моделирования Synopsys HSpice. Скорость компаратора увеличена на 57,8%.

Ключевые слова: компаратор, динамическая защелка, динамическая защелка с одним корпусом, динамическая защелка с двумя корпусами, вариация между процессами, низкая входная емкость, высокая скорость.

УДК 531.8

Поступила: 28.04.2020г.
Сдана на рецензию: 30.04.2020г.
Подписана к печати: 15.05.2020г.

KINEMATIC AND DYNAMIC ANALYSIS OF PARALLEL DELTA MICROMANIPULATOR

H. Galoyan

Department of Mechanical Engineering and Machine Science

hrayr.galoyan@gmail.com

ABSTRACT

This paper presents the design process, kinematic and dynamic analysis of 3DOF parallel Delta micromanipulator. Micromanipulators are used in microsurgery, microbiology, microelectronic and other fields which need high precision. They convert human motions into output links or work with previously programmed coordinates.

Most of existing Delta micromanipulators are designed with bending piezoelectric actuators or rotary electric motors. It is well known that bending piezoelectric actuators provide large displacement but low holding force. Rotary electric motors are capable of providing both large displacement and high holding torque but they are less precise compared to piezoelectric actuators. The Delta micromanipulator presented in this paper is designed with piezoelectric linear actuators which have 300 nm accuracy and 350 mm travel range which is quite competitive with aforementioned options.

Also, most of existing Delta micromanipulators use traditional joints which have issues such as lubrication, backlash, friction, corrosion, and pollution. Unlike them, the presented Delta micromanipulator is designed with Butterfly flexure pivots which have advantageous mechanical characteristics such as ± 20° deflection angle and 1.54 Nm/radians angular stiffness.

Keywords: Delta micromanipulator, flexure pivot, flexural hinge, kinematics, dynamics.

1. Introduction

The main advantages of the designed Linear Delta or Prismatic-Input Delta micromanipulator over other types are its high accuracy, payload and acceleration. The robot's base is mounted above the workspace and all the actuators are located on it. From the base, three middle jointed arms extend. The ends of these arms are connected to a small triangular platform. Actuation of the input links will move the triangular platform along the X, Y or Z directions. Three inputs are driven by three linear-sliding prismatic joints instead of three revolute joints of more popular Revolute-Input Delta manipulators. This design change simplifies the kinematics equations, and there are neither sines nor cosines required as in the revolute-input case. Each arm consists of one linear actuator, links and 2 pairs of 2DOF (or 3DOF) joints. The kinematic diagram of Delta manipulator (Fig. 1) is presented below.

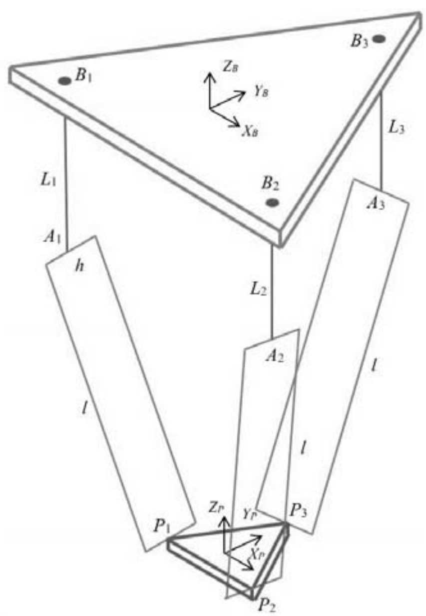


Fig. 1. Kinematic diagram of Delta manipulator.

2. Design of micromanipulator

2.1. Flexure pivots

Flexure pivots are essential components of micromanipulators due to their high accuracy and easy operation. They are made by various techniques: computer numerical control (CNC) milling, laser machining, additive manufacturing, chemical etching, electrical discharge machining (EDM), etc. The key stipulation is the high accuracy of machining [1].

Butterfly flexure pivots (Fig. 2) [2], which are used in micromanipulator arms, are 1DOF joints, so each arm consists of 4 flexure pivots, 2 of which are coupled (Fig. 3).Various design modifications (Fig. 4) of Butterfly flexure pivot have been developed towards reaching desirable stiffness of "Butterfly" flexure pivot. The selected model has advantageous mechanical characteristics such as ± 20° deflection angle, 1.54 Nm/radians angular stiffness, and the 751 MPa maximal stress in blades for a ±20° stroke.

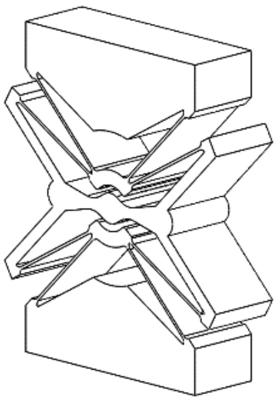


Fig. 2. Butterfly flexure pivot.

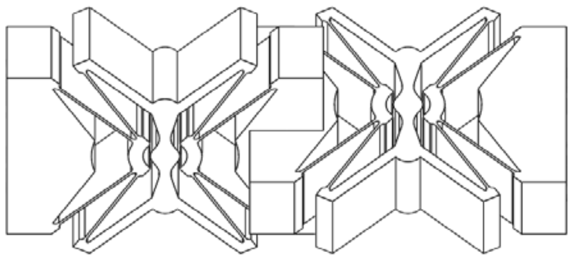


Fig. 3. Coupled Butterfly flexure pivots.

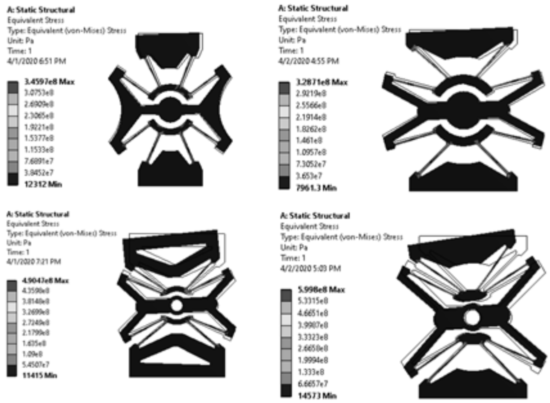


Fig. 4. Modified Butterfly pivots.

2.2. Linear actuators

Linear actuators are the fundamental element of micromanipulators. The presented "PICMA N–422" piezoelectric linear actuator [3] (Fig. 5) has been chosen for its superb features. It works with a step-by-step moving principle by means of which the flexible rod moves by the stator with 300 nm steps. The overall travel range is 35 mm.



Fig. 5. "PICMA N-422" piezoelectric linear actuator.

2.3 Arm design and assembly

The arm of micromanipulator (Fig. 6) has been designed with the aforementioned 2 components: Butterfly flexure pivots and "PICMA N-422" piezoelectric linear actuator. Onwards, micromanipulator's

assembling process has been implemented with three previously designed arms. Two triangle shaped frames have been designed in order to unite actuators and make the system more stable. The overall dimensions of the micromanipulator are 125x125x105 mm.

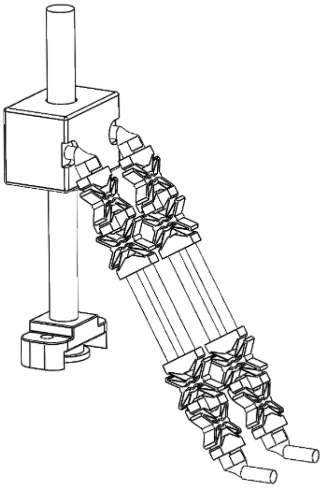


Fig. 6. Arm of micromanipulator.

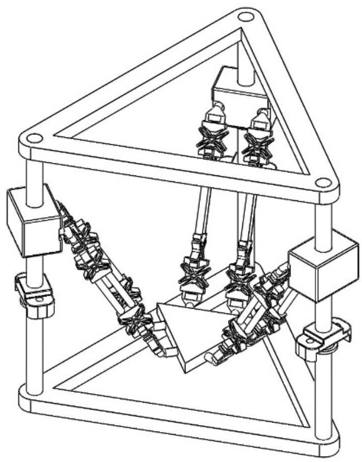


Fig. 7. Assembled micromanipulator.

3. Kinematic analysis

The forward position kinematics (FPK) solution for parallel robots [4] is generally very difficult. It requires the solution of multiple coupled nonlinear algebraic equations, from the three constraint equations applied to the vector loop-closure equations. Multiple valid solutions generally result. Thanks to the translation-only motion of the 3DOF Delta manipulator, there is a straightforward analytical solution for which the correct solution set is easily chosen. Since $L = \{L_1 L_2 L_3\}^T$ are given, we calculate the three absolute vector knee points using ${}^{B}A_i = {}^{B}B_i + {}^{B}L_i$, $i = 1, 2, 3$. Referring to the prismatic-input Delta manipulator FPK diagram below, since we know that the moving platform orientation is constant, always

horizontal with $[{}^{B}_{P}R] = [I_3]$, we define three virtual sphere centers ${}^{B}A_{iv} = {}^{B}A_i - {}^{P}P_i$, *i = 1, 2, 3:*

$$ {}^{B}A_{1v} = \begin{Bmatrix} -\frac{s_B}{2} + \frac{s_p}{2} \\ -W_B + w_P \\ -L_1 \end{Bmatrix} \; {}^{B}A_{2v} = \begin{Bmatrix} \frac{s_B}{2} - \frac{s_p}{2} \\ -W_B + w_P \\ -L_2 \end{Bmatrix} \; {}^{B}A_{3v} = \begin{Bmatrix} 0 \\ U_B - u_P \\ -L_3 \end{Bmatrix} \quad (1) $$

and then the prismatic-input Delta Robot FPK solution is the intersection point of three known spheres. Let a sphere be referred as a vector center point {c} and scalar radius r, ({c}, r). Therefore, the FPK unknown point $\{{}^{B}P_P\}$ is the intersection of the three known spheres:

$$ (\{{}^{B}A_{1v}\}, l)(\{{}^{B}A_{2v}\}, l)(\{{}^{B}A_{3v}\}, l) \quad (2) $$

Symbol meanings are described in Table 1, Fig. 7 and Fig. 8.

Table 1.

Symbol meanings.

Name	Meaning
s_b	base equilateral triangle side
w_b	planar distance from {0} to near base side
u_b	planar distance from {0} to a base vertex
H	frame height
S_b	P joints (Bi) equilateral triangle side
W_B	same as w_b, for P joints equilateral triangle
U_B	same as u_b, for P joints equilateral triangle
s_P	platform equilateral triangle side
w_P	planar distance from {P} to near platform side
u_P	planar distance from {P} to a platform vertex
L_{min}	*i* = 1,2,3 minimum prismatic joints lengths

L_{max}	i = 1,2,3 maximum prismatic joints lengths
l	lower legs parallelogram length
h	lower legs parallelogram width

The FPK solution x y z is for the moving platform geometric center. When the desired control point is offset from the center, a further transformation is required after, to implement the FPK solution:

$$[{}^{B}_{N}T] = [{}^{B}_{P}T][{}^{P}_{N}T] \tag{3}$$

where

$$[{}^{P}_{N}T] = \begin{bmatrix} 1 & 00 & O_X \\ 0 & 10 & O_Y \\ 0 & 01 & 0 \\ 0 & 00 & 1 \end{bmatrix} \tag{4}$$

By virtue of FPK method, the workspace of micromanipulator has been definedwhich is 37000 mm^3.

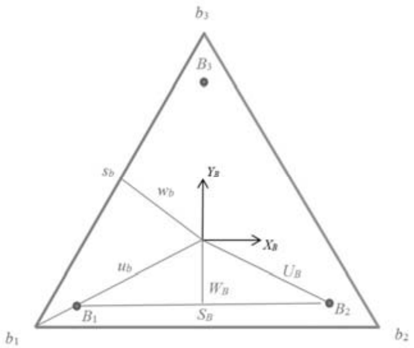


Fig. 7. Fixed base details.

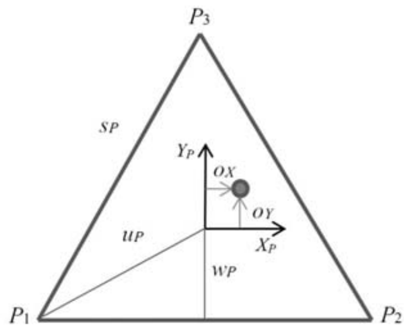


Fig. 8. Moving platform details.

4. Dynamic analysis

Dynamic analysis of Delta micromanipulator has been carried out by directly inputting its model from SOLIDWORKS [5] into ANSYS [6]. Micromanipulator's moving platform poses its utmost position at the±20°

deflection angle of flexure pivots. Hence, the maximal deflection angle has been given to the flexure pivots. Afterwards, maximal stress (Fig. 9) and displacement of arm components have been determinated via finite element analysis (FEA). The maximal stress in blades of flexure pivotsis 751 MPa and the displacement of moving platform (maximal) is ±20.09mm.

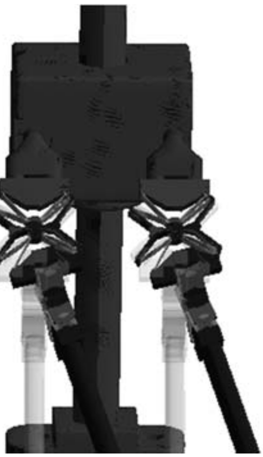


Fig. 9. Maximal stress at utmost position.



Fig. 10. Deformation at utmost position.

The maximal ±18.78mm displacement of moving platform asserts that the workspace analysis is plausible because of its cylindrical shape, the radius of which is equal to maximal displacement of moving platform and the height is equal to linear actuator's travel range (35 mm).Also, the optimal payload has been carried out via FEA, with results of 4.27 N.

5. Conclusion

To conclude, 3DOF parallel Delta micromanipulator has been designed with flexure pivots and piezoelectric linear actuators. Kinematic and dynamic analysis has been implemented in order to determinate the

workspace of micromanipulator, optimal payload and stress in hinges. Quite competitive results have been attained such as 37000mm^3 workspace and 435g optimal payload.

REFERENCES

1. *Jain, V.* Micromanufacturing Processes, 55–113, 2017.
2. *Henein, S. et. al.* Flexure Pivot for Aerospace Mechanisms, Proceedings of the 10-th ESMATS, ESA SP-524, 2003.
3. https://www.physikinstrumente.com/en/products/linear-actuators/piezomike-for-long-term-stability/n-422-linear-actuator-with-pishift-piezomotor-1000130/#description
4. *Robert L. Williams.* The Delta Parallel Robot: Kinematics Solutions, Ohio University, 2016.
5. https://www.solidworks.com/
6. https://www.ansys.com/

КИНЕМАТИЧЕСКИЙ И ДИНАМИЧЕСКИЙ АНАЛИЗ ПАРАЛЛЕЛЬНОГО МИКРОМАНИПУЛЯТОРА ДЕЛЬТА

Г. Галоян

АННОТАЦИЯ

В данной статье представлен процесс проектирования, кинематический и динамический анализ параллельного микроманипулятора Дельта с тремя степенями свободы. Микроманипуляторы используются в микрохирургии, микробиологии, микроэлектронике и в других областях, которые требуют высокой точности. Они преобразуют движения человека в выходные звенья или работают с ранее запрограммированными координатами.

Большинство существующих микроманипуляторов Дельта имеют изгибные пьезоэлектрические приводы или вращающиеся электродвигатели. Известно, что изгибные пьезоэлектрические приводы обеспечивают большое смещение, но низкую удерживающую силу. Электродвигатели способны обеспечивать как большое смещение, так и высокий удерживающий момент, но они менее точ-

ны по сравнению с пьезоэлектрическими приводами. Микроманипулятор Дельта, представленный в этой статье, разработан с пьезоэлектрическими линейными приводами, которые имеют точность 300 нм и диапазон перемещения 350 мм, что вполне конкурирует с вышеупомянутыми вариантами.

Кроме того, большинство существующих микроманипуляторов Дельта используют традиционные шарниры, которые имеют такие проблемы, как необходимость смазки, люфт, трение, коррозия и загрязнение. В отличие от традиционных шарниров, представленный микроманипулятор Дельта разработан с упругими шарнирами типа бабочка, которые имеют весьма положительные механические характеристики – такие, как угол отклонения ± 20 ° и угловая жесткость 1,54 Нм/радиан.

Ключевые слова: Дельта-микроманипулятор, упругий шарнир, кинематика, динамика.

УДК 621.382

Поступила: 23.04.2020г.
Сдана на рецензию: 11.05.2020г.
Подписана к печати: 18.05.2020г.

VIX CORRELATION IMPROVEMENT BETWEEN SPICE AND IBIS USING DUTY CYCLE

H. Vardanyan, S. Ghukasyan

National Polytechnic University of Armenia

vardanya@synopsys.com, ghukasya@synopsys.com

ABSTRACT

Nowadays the role of IBIS model has increased as it has started to provide more information about I/O. So, to know if IBIS model is generated correctly and shows all the information we need, we must establish correlation between the generated IBIS model and SPICE model, as SPICE model is always a golden reference because of its high accuracy. And after establishing the correlation there are some major key parameters that must be the same for IBIS and SPICE models or at least deviate from each other in a specified range. The major key parameters are VOH, VOL, $Vcross$, slew rate for both rising and falling waveforms. In case of VOH and VOL it is simpler to correct these values, because in most cases the deviation comes from a wrong setup or from using different libraries. But for the other parameters it is not simple because it can relate to something else, which cannot be corrected without interference from outside. In this paper a method of optimizing the Vix_ratio (which relates to$Vcross$) between IBIS and SPICE models using duty-cycle difference is discussed. This supposed method is a completely new approach, and, in this paper, it will become obvious that with this method we can reach our required Vix_ratio value with great precision and ease. The proposed method will increase the precision.

Keywords: IBIS,Vix_ratio, SPICE, correlation, duty cycle.

Introduction

Input/output Buffer Information Specification (IBIS) is a file which includes information about input/output buffers. Since the 1990s there have been few standards of making the IBIS file which differ from each other by voltage vs. time (Vt) and current vs. voltage (Iv) tables. During the development of these standards a few types of IBIS models have appeared for different usages. IBIS-AMI models run in a special-purpose SerDes channel simulator, not in a SPICE-like simulator, and consist of two text files (*.ibs and*.ami) plus a platform-specific machine code executable file (*.dllon Windows,*.so on Linux) [1]. IBIS-AMI support statistical and so-called time-domain channel simulations, and three types of IC model ("impulse-only," "GetWave-only," and "dual mode"). The advantage of IBIS model is also its simulation speed. That said, when the customer has the IBIS models for TX and if the difference between the IBIS and SPICE is within an acceptable range, the simulation of TXRX macro becomes many times faster. And as we know the first company that has the first good results becomes number one in the market. So from a business point of view the IBIS model becomes crucial. Nowadays the most usable IBIS model is the traditional one, which includes 16 Iv, Vt and It tables for each case. And all these 16 simulations are done for all cases (the IBIS model can include up to 3 cases).

The simulations are:

- C_comp (If)*
- C_comp_pullup (If)*
- C_comp_pulldown (If)*
- Clamp (Iv)
- Pullup (Iv)
- Pulldown (Iv)
- ISSO_PU (Iv)
- ISSO_PD (Iv)
- Rise_gnd (Vt)
- Rise_gnd_compcur (It)

- Rise_sup (Vt)
- Rise_sup_compcur (It)
- Fall_gnd (Vt)
- Fall_gnd_compcur (It)
- Fall_sup (Vt)
- Fall_sup_compcur (It)

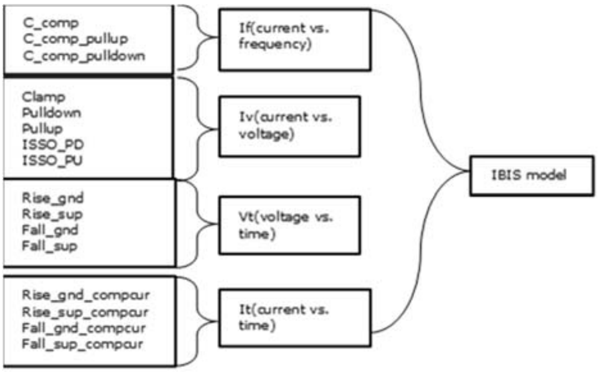


Fig. 1. Simulations and their types for IBIS model.

The first three simulations are AC simulations and are used to calculate the output, pullup and pulldown capacitances by performing an AC or frequency sweep analysis of the buffer. Clamp simulation shows the ESD diodes' behavior on the output. Pullup simulation shows how much current flows through pullup section when the pulldown section is in tristate, and for the pulldown simulation the same is done when the pullup section is in tristate. ISSO_PU simulation is done to show the power supply noise influence on the output, and, for that purpose, the power supply is being swept from 0 to 2*VDD and the output current is being calculated. ISSO_PD is almost the same as ISSO_PU but this shows the ground net noise influence on the output and the ground net's value is swept from -VDD to VDD [2]. All 4 Vt simulations are done to have information about the driver's rising and falling behaviors, and the It waveforms are to know

the current during rising and falling. But both rising and falling simulations are done for two cases:

- With 50 Ohms termination to the ground,
- With 50 Ohms termination to the supply

and respectively the current simulations are done for those 2 cases.

For this paper will use the traditional IBIS standard which will be 5.1 standard. As mentioned above, the usage of IBIS model gives an opportunity to take the information about TX that is needed from the IBIS model without having different test benches. That being said, with one tes tbench the user can have all the information about TX, while in case of SPICE the user must have different test benches for different cases.

Correlation improvement methodology. For differential signals there are 2 cross point values:

- When the rising edge of the truesignal crosses the falling edge of thecomplementary signal,
- When the falling edge of the true signal crosses the rising edge of thecomplementary signal.

After calculating those values, we must have Vref,Vswing values in order to calculate the Vix_diff_ratioparameter. This parameter will show how much the Vcrossvalue differs from Vref (by percentage).

$$Vix\ \ _{ratio_{com}} = \frac{Vref - Vcross_{com}}{Vswing} * 100\%$$

$$Vix\ \ _{ratio_{true}} = \frac{Vref - Vcross_{true}}{Vswing} * 100\%$$

After calculating $Vix\ \ _{ratio_{true}}$ and $Vix\ \ _{ratio_{com}}$ for SPICE we must calculate those values for IBIS too.

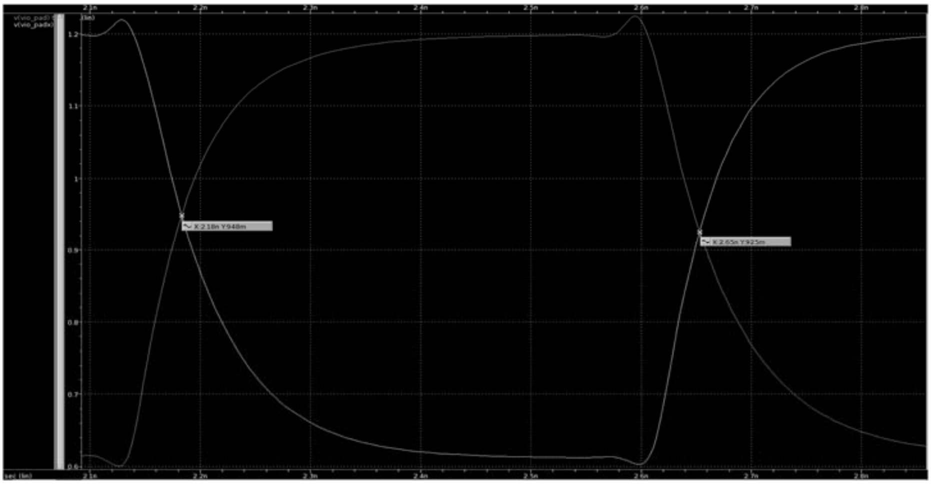


Fig. 2.Vcross values for SPICE.

Fig. 2 shows the Vcross values of SPICE for both true and complementary signals. For SPICE we have948mV for a true signal and 925mV for a complementary signal. For the same case without improvement for IBIS we have 950mV for both true and complementary signals. For getting these waveforms below the mentioned test bench was used.

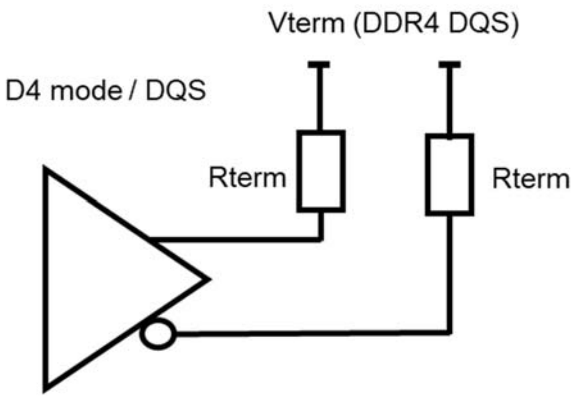


Fig. 3. Test bench used for the paper.

Fig. 3 shows the test bench that was used for doing the validation. From the results we can see that the difference between Vcross values of IBI Sand SPICE of the true signal matche a chother, but for the complementary signal the values do not match so well [3]. So, we must moderate the IBIS model so that the values match the complementary signal too. We thus propose a new method which will use the duty cycle difference between signals of SPICE and IBIS. To use this method, we need to calculate the duty cycle values of IBIS and SPICE for both true and complementary signals. After calculating those values, we calculate the difference between those value sand that difference will show how much the IBIS must be moderated. And by moderating the IBIS model we understand shifting, rising or falling edge. For this case we have values mentioned in Fig. 4.

		DCD (%)													
		True	Comp	Vcross (mV)		Vswing (mV)	Vref (mV)	Vix_RATIO (%)		Delta (%)		Delta_DCD		Shift	
Model	SPICE	50.8	50.8	948	925	588	909	-6.6	-2.7	0.34	4.25	0.2	1.2	1.25	7.5
	IBIS	51	52	950	950	588	909	-6.9	-6.9						

Fig. 4. Required parameters before moderating IBIS.

From Fig. 4 we can see that the difference between IBIS and SPICE is also visible from Delta_DCD, which is the difference between IBIS and SPICE duty cycle values. The Delta parameter is our required value to optimize, which is equal to Vix_ratio_spice – Vix_ratio_ibis [4]. After having the Delta_DCD we can calculate how much and in which direction the waveform must be shifted. The value depends on how much the frequency is, as the Shift parameter equals to

$$\text{Shift} = \text{Delta_DCD} * \text{Per}/100$$

And when we get a positive value, we must shift the wave forms to the right, and if the value is negative to the left. But depending on which signal must be moderated we have to do the shifting only for that signal. It means if you get a positive or negative value for a true signal the rising wave form must be shifted to the right or to left, and if the complementary signal is needed to be adjusted, the falling wave form must be shifted. This is because IBIS standard model is a single-ended model, and the rising wave form for the complementary signal is the falling wave form of the true signal. And note that by shifting the rising (falling) wave form for the complementary signal the results of the true signal will change also. But there is a way to not have an effect on the true signal, and it is using 2 different IBIS models, one for the true signal and one for the complementary signal, and adjusting them separately [5].

For shifting the IBIS model wave forms a script has been created with python language, for which you give the type of the wave form (rising or falling), the case (min, max, type), mode l name a san input argument and it will shift the IBIS model's wave forms accordingly.

Simulation results. By considering the results in Fig. 4 and taking the steps mentioned in the previous chapter, we get the results mentioned in Fig. 5.

		DCD (%)													
		True	Comp	Vcross (mV)		Vswing (mV)	Vref (mV)	Vix_RATIO (%)		Delta (%)		Delta_DCD		Shift	
Model	SPICE	50.8	50.8	948	925	588	909	-6.6	-2.7	3.06	0.85	0.2	0.2	1.25	1.25
	IBIS	51	52	930	930	588	909	-3.6	-3.6						

Fig. 5. Results after adjusting IBIS.

From Fig. 5 we can see that the Delta values have changed due to shifting the IBIS model. We can see also that not only did the Delta value for the complementary signal become better but the results of the true signal changed also (due to having one IBIS model for both signals).

Conclusion

This paper discusses a method of improving the Vix correlation between SPICE and IBIS using the duty cycle difference. With this method it is possible to have the desired Vix correlation. By taking into account how important it is to have a better correlation, this method gives an opportunity to optimize the IBIS model and meet customers' requirements. This method has already been used in Synopsys DDR team (where the authors work), and the improved IBIS models have been delivered to a specific customer, which had had its specific margin for SPICE and IBIS difference.

REFERENCES

1. *Chu X., Hwang C., Fan J.and. Li Y.* Analytic Calculation of Jitter Induced by Power and Ground Noise Based on IBIS I/V Curve, in IEEE Transactions on Electromagnetic Compatibility, vol. 60, no. 2, April 2018. PP. 468–477.
2. *Varma A., Steer M. and Franzon P.* Developing Improved IO Buffer Behavioral Modeling Methodology Based on IBIS, 2006 IEEE Electrical Performance of Electronic Packaging, Scottsdale, AZ, 2006. PP. 69–72.
3. *Schutt-Ainé J., Liu P., Tan J. and Varma A.* IBIS Simulation Using the Latency Insertion Method (LIM),in IEEE Transactions on Components, Packaging and Manufacturing Technology, vol. 3, no. 7, July 2013, PP. 1228–1236.
4. *Pulici P. et al.* A Modified IBIS Model Aimed at Signal Integrity Analysis of Systems in Package, in IEEE Transactions on Circuits and Systems I: Regular Papers, vol. 55, no. 7, Aug. 2008. PP. 1921–1928.
5. *Nandakumar G., Patel N., Reddy R. and Kothandaraman M.* Application of Douglas-Peucker algorithm to generate compact but accurate IBIS models,18th International Conference on VLSI Design held jointly with 4th International Conference on Embedded Systems Design, Kolkata, India, 2005. PP. 757–761.

УЛУЧШЕНИЕ КОРРЕЛЯЦИИ VIX МЕЖДУ SPICE И IBIS С ИСПОЛЬЗОВАНИЕМ РАБОЧЕГО ЦИКЛА

А.В. Варданян, С.А. Гукасян

В настоящее время роль модели IBIS возросла, поскольку она стала предоставлять больше информации о вводе/выводе. Таким образом, чтобы знать, правильно ли сгенерирована модель IBIS и показана ли вся необходимая информация, мы должны сделать корреляцию между сгенерированной моделью IBIS и моделью SPICE, поскольку модель SPICE всегда является золотым эталоном из-за ее высокой точности. И после выполнения корреляции есть некоторые основные ключевые параметры, которые должны быть одинаковыми для модели IBIS и SPICE или, по крайней мере, отклоняться друг от друга в указанном диапазоне. Основными ключевыми параметрами являются VOH, VOL, Vcross, скорость нарастания как для восходящих, так и для падающих сигналов. В случае VOH и VOL эти значения проще исправить, поскольку в большинстве случаев отклонение происходит из-за неправильной настройки или использования разных библиотек. Но для других параметров это не просто, потому что это может относиться к чему-то другому, что не может быть исправлено без вмешательства извне. В этой статье обсуждается метод оптимизации Vix_ratio (который относится к Vcross) между моделями IBIS и SPICE с использованием разности рабочих циклов. Этот предлагаемый метод является совершенно новым подходом, и статья ясно показывает, что с помощью этого метода мы можем легче достичь требуемого значения Vix_ratio с большой точностью. Предлагаемый способ позволит повысить точность.

Ключевые слова: IBIS, Vix_ratio, SPICE, корреляция, рабочий цикл.

УДК621.3.049.779

Поступила: 27.04.2020г.
Сдана на рецензию: 08.05.2020г.
Подписана к печати: 15.05.2020г.

HYSTERESIS IMPROVEMENT METHOD IN MIPI D-PHY LOW-POWER RECEIVER

A. Mkhitaryan[1], H. Grigoryan[1], H. Margaryan[2], V. Hovhannisyan[1], M. Grigoryan[1], M. Grigoryan[1], H. Kirakosyan[1], H. Kostanyan[1]

[1]National Polytechnic University of Armenia,
[2]Yerevan State University

marthur@synopsys.com, hgrigo@synopsys.com, hmargar@synopsys.com, vardan@aragatsltd.am, manvelg@synopsys.com, mushegg@synopsys.com, hkirako@synopsys.com, hakobk@synopsys.com

ABSTRACT

Hysteresis improvement method of low-power receiver in MIPI D-PHY architectures has been proposed in this paper. Technical specifications of modern integrated circuits require 4.5 sigma Monte Carlo coverage of the blocks. Comparison between the existing and proposed schematics has shown big improvements of the hysteresis. The solutions proposed in the paper provide a possibility to cover more than 4.5 sigma range without violating the 25mV technical specification of the low-power receiver hysteresis. The circuit has been designed with SAED14 nm FinFet technology, meets the technical requirements of modern integrated circuits, does not result in power consumption increase. The required area increase for proposed improvements is neglect table.

Keywords: low-power receiver, hysteresis, noise immunity, Monte Carlo.

Introduction

In MIPI D-PHY products the low-power receiver is an un-terminated, single-ended receiver circuit [1–2]. There are several operation modes and the low-power receiver is used to detect the low-power state on each pin. For high noise immunity the receiver should filter out noise pulses and radio frequency interference. To realize the above-mentioned requirements in actual designs the specifications provided in table 1 are required to be met [1]. VIH and VIL are the input voltage levels at which the low-power receiver should detect the high and low states of the input signal correspondingly. To be able to reject the spikes at the input signals the hysteresis of the receiver should be not less than 25mV.

Table. 1

Low-power receiver main specifications.

Parameter Name	Parameter Description	Min	Max
V_{IH} (mV)	Logic 1 input voltage	880	-
V_{IL} (mV)	Logic 0 input voltage	-	550
V_{HSYT} (mV)	Input hysteresis	25	-
P_{lp} (uW)	Power consumption	-	50

Problem description and proposed solution. The main challenging parameter while designing the block is the input hysteresis. To organize this, the circuit switching points from 1 to 0 and from 0 to 1 should be different. Below is presented the widely used lower-power receiver schematic view with integrated hysteresis circuit (fig.1) [3–5]. The hysteresis procedure is implemented by the M3 and M4 transistors which counteract the M6 and M7 transistors during the switching of the outputs from 1 to 0 and actuate the output transition from 0 to 1.

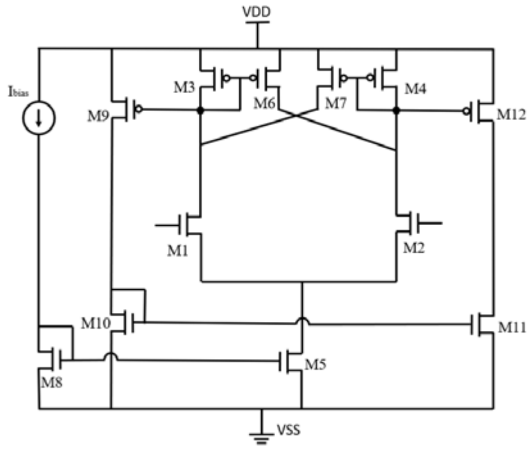


Fig. 1. Low-power receiver with integrated hysteresis circuit.

HSpice simulation results [6] of the circuit designed by SAED14nm FinFet technology [7] have shown 90mV hysteresis for the low-power receiver (Fig. 2).It is known that CMOS technology is not consistent and the deviation causes variation of transistors' parameters resulting in degradations of their parameters. Meanwhile the manufactured integrated circuits (IC) should meet the technical specifications in at least 4.5 sigma Monte-Carlo range [8].So, the purpose of the paper is to design the low-power receiver to be functional in the mentioned range without violating the specifications.

To meet the above-mentioned requirement Monte Carlo Spice simulation has been performed for the designed low-power receiver circuit. As shown in the waveforms, the hysteresis varies from 5mV to 92mV and in lower bounds it violates the 25mV specification (fig. 3). Meanwhile the hysteresis variation is extra big which impacts the transient results.

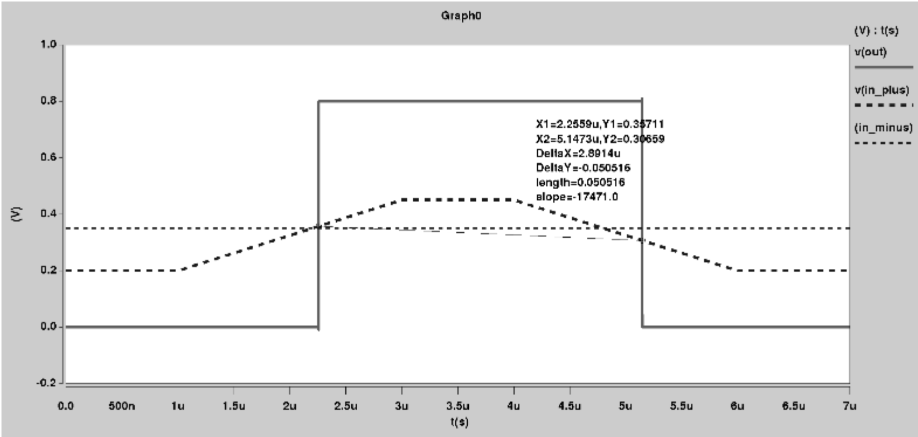


Fig. 2. Low-Power receiver hysteresis results.

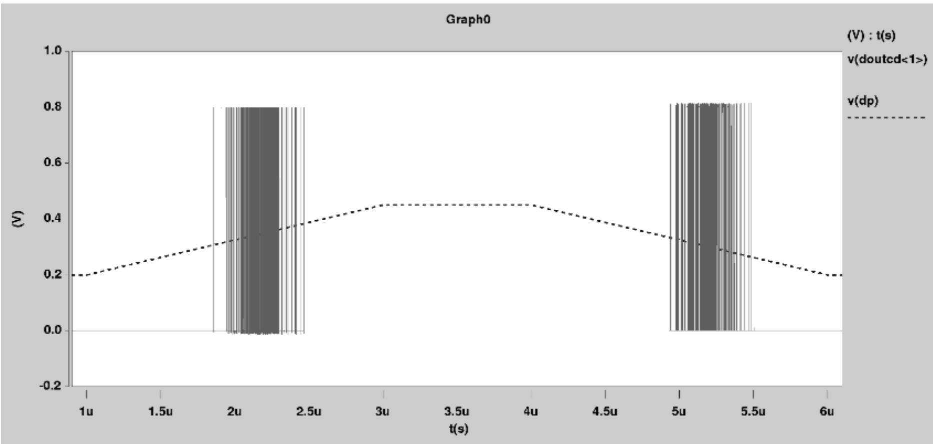


Fig. 3. Low-power receiver Monte Carlo simulation results.

Monte Carlo simulation summary is provided by Q-Q plot (Fig.4). It shows that with current architecture block is able to meet the 25mV hysteresis spec only in 2 Sigma.

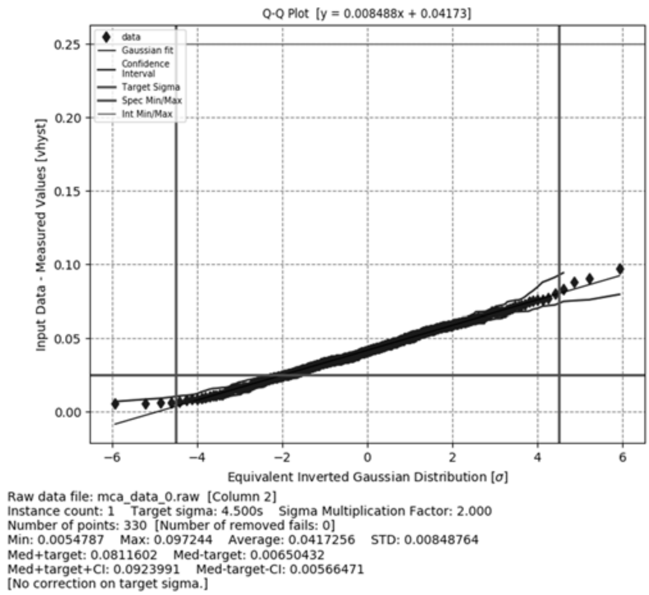


Fig. 4. Q-Q plot received from Monte Carlo simulation of current architecture.

To solve the above-mentioned problem several trials have been performed while they were even not able to provide required hysteresis results or caused violations of the remaining important specifications such as V_{IL} or V_{IH}. To solve the problem the new architecture of low-power receiver has been proposed (Fig. 5).

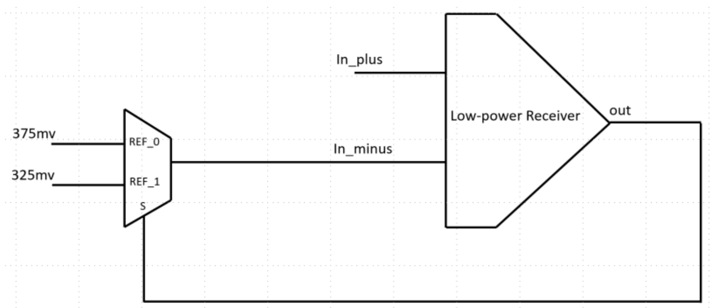


Fig. 5. Low-power receiver proposed architecture.

In this circuit the hysteresis was realized by analog multiplexer instead of integrated transistors. Initially the reference voltage was constant 350mV: such kind of stable reference voltage generation is usually done by bandgap voltage reference circuits. The feedback between the receiver output and input has been organized so that when the output is 1, the reference voltage on the negative 'In_minus' node stands at 25mV less i.e. 325mV. So less than 325mV is required to be applied to the positive input of the receiver to switch it from 1 to 0. And if the output of the receiver is 0, the 375mV reference is applied to the negative input, hence bigger than 375mV is required to switch it from 0 to 1. In schematic implementation of the proposed architecture the M3 and M4 transistors have been removed and the analog multiplexer has been designed (Fig. 6).

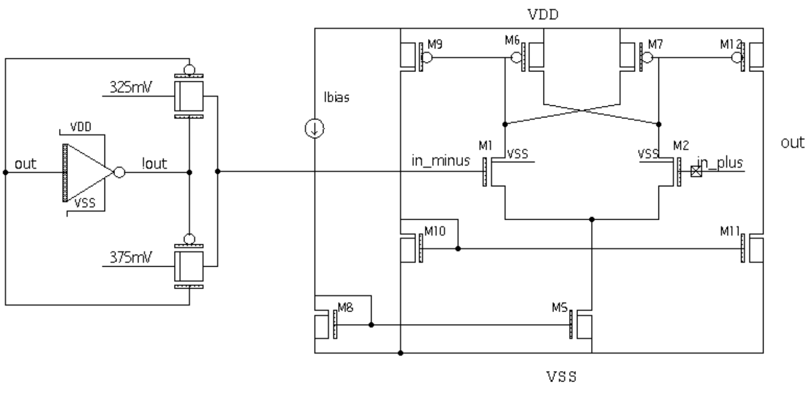


Fig.6. Schematic design of proposed circuit.

Simulation results have shown big improvements in the results (Fig. 7). Minimum achieved hysteresis is 60mVin 4.5 sigma Monte Carlo variation range.

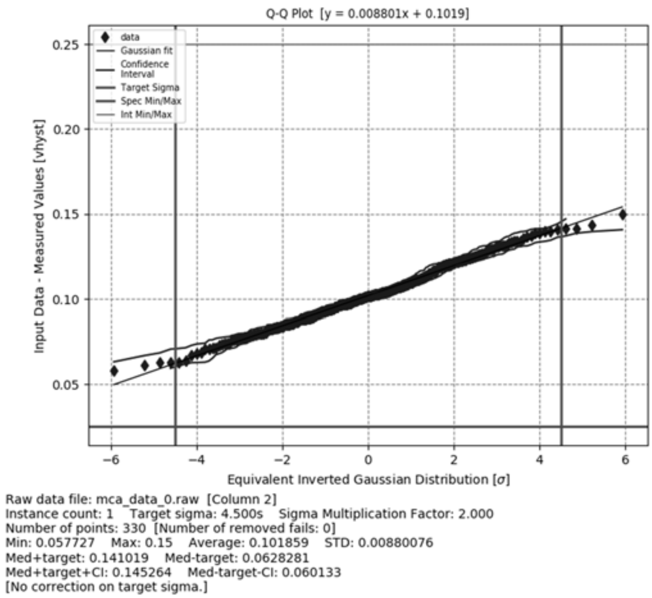


Fig. 7. Q-Q plot received from Monte Carlo simulation of proposed architecture.

Results

4.5 sigma Monte Carlo Spice simulating results are presented in Table 2. The proposed architecture improved the V_{IH} and V_{IL} parameters; meanwhile it was possible to meet the hysteresis spec with a big margin. The area increase due to the extra cells is neglectable comparing with the low-power receiver area. Based on the results the problem can be marked as solved.

Table 2.

Proposed low-power receiver simulation results.

Parameter Name	Specification		Simulation results			
			Existing circuit		Proposed circuit	
	Min	Max	Min	Max	Min	Max
V_{IH} (mV)	880	-	885	1200	920	1200

V_{IL} (mV)	-	550	0	540	0	500
V_{HSYT} (mV)	25	-	5.6	92	60	145
P_{lp} (uW)	-	50	10	40	10	40

Conclusion

The hysteresis improvement method in MIPID-PHY low-power receiver is proposed in this paper. The feedback loop organized between the output and the input of the receiver has improved the hysteresis Monte Carlo simulation results. The analog multiplexer was used as a hysteresis provider cell. HSPICE simulation results of the designer low-power receiver have shown 45.4mV improvement of the hysteresis by keeping it in the range of technical specification. The logic 1 and logic 0 input voltages also have been improved by 40mV. The proposed method does not result in power consumption increase. The required area on semiconductor surface is neglectable compared to the low-power receiver area.

REFERENCES

1. *Harrant M., Nirmaier T., Kirscher J., Grimm C.* Monte Carlo based post-silicon verification considering automotive application variances. // Proceedings of the 2013 9-th Conference on Ph.D. Research in Microelectronics and Electronics (PRIME). Villach, 2013. PP. 165–168.
2. *HSpice Reference Manual*, Synopsys Inc. 2019. 846p.
3. *Specification for D-PHY, MIPI alliance*. 2015.143p.
4. *Khanfir L., Mouïne J.* Programmable Clock Delay for Hysteresis Adjustment in Dynamic Comparators // 2018 30-th International Conference on microelectronics (ICM). Sousse, Tunisia, 2018. PP. 264–267.
5. *Kim B., Lee S., Kim D., Cho K.* Design of a D-PHY chip for mobile display interface supporting MIPI standard // 2012 IEEE International Conference on Consumer Electronics (ICCE). Las Vegas, NV, 2012. PP. 660–661.
6. *Melikyan V., Martirosyan M., Piliposyan G.* 14nm Educational Design Kit: Capabilities, Deployment and Future, Small Systems Simulation Symposium, 2018.

7. *Nanda S., Panda A., Moganti G.* A novel design of a high speed hysteresis-based comparator in 90-nm CMOS technology *// 2015 International Conference on Information Processing (ICIP).* Pune, 2015. PP. 388–391.
8. *Tao J., Wang Y., Xing J.* A comparator with flexible programming of the hysteresis. // 2010 International Conference on Anti-Counterfeiting, Security and Identification.Chengdu, 2010. PP. 105–107.

МЕТОД УЛУЧШЕНИЯ ГИСТЕРЕЗИСА ПРИЕМНИКА С НИЗКОЙ ЭНЕРГОПОТРЕБЛЯЕМОСТЬЮ ДЛЯ АРХИТЕКТУРЫ MIPI D-PHY

А.Х. Мхитарян, А.Т. Григорян, А.В. Маргарян,
В.Д. Оганнисян, М.Т. Григорян, М.Т. Григорян
А. Г. Киракосян, А.Т. Костанян

АННОТАЦИЯ

В данной статье предложен метод улучшения гистерезиса приемника с низкой энергопотребляемостью, используемого в архитектуре MIPI D-PHY. Одним из требований, предъявляемых к современным интегральным схемам, является необходимость обеспечения бесперебойной работы в области доверительного интервала 4.5 сигма. Результаты моделирования как уже существующих, так и предлагаемых схем доказывают высокую эффективность данного метода. В результате применения предлагаемых методом решений стало возможным обеспечение значения гистерезиса более чем 25мВ, что является требованием технического задания. Схема спроектирована по технологическому процессу SAED 14 nm FinFet, соответствует современным требованиям проектировки интегральных схем, не увеличивает энергопотребление, увеличение площади занимаемой схемой на полупроводниковом кристалле незначительно.

Ключевые слова: низкая энергоподребляемость, приемник, гистерезис, шумоустойчивость, Монте Карло.

БИОЛОГИЯ

УДК 502(479):06

Поступила: 10.04.2020г.
Сдана на рецензию: 11.04.2020г.
Подписана к печати: 15.04.2020г.

МОРФО-ЭКОЛОГИЧЕСКИЕ ОСОБЕННОСТИ ЛЕСНЫХ МЫШЕЙ (MURIDAE: *APODEMUS*) ФАУНЫ АРМЕНИИ

В.Б. Азарян

Российско-Армянский университет

valentina.azaryan@rau.am

АННОТАЦИЯ

В данной статье описаны экологические особенности и проведен анализ морфометрических показателей трех видов лесных мышей, населяющих территорию Республики Армения. Морфологическая оценка представителей лесных мышей (Muridae: *Apodemus*) является методом первичной характеристики и определения видов, преимущественно, в ходе полевых работ. Имеет место выраженная видовая и географическая изменчивость видов *Apodemus* фауны Армении.

Ключевые слова: морфология, экология, *Apodemus*, фауна, Армения.

Введение. Западнопалеарктические лесные мыши рода *Apodemus* Kaup, 1829 sensu lato представлены в фауне Армении тремя видами, а именно: *Apodemus ponticus* (Sviridenko, 1936) – Кавказская мышь, *Apodemus uralensis* (Pallas, 1811) – малая лесная мышь (Уральская мышь) и *Apodemus witherbyi* (Thomas, 1902) – степная мышь. Лесные мыши были отмечены и исследованы во всех регионах Республики Армения [1–4], что указывает на их практически повсеместное распространение. Однако морфологическая характеристика, изучение экологии лесных мышей и их распространение до сих пор носят неполный характер – в силу морфологической дифференциации видов, отсутствия полных и четких определительных показателей, сложности видовой идентификации и наличием широкого спектра экологических особенностей.

В данной статье приводится морфологическая оценка трех видов лесных мышей рода *Apodemus* с описанием их экологических особенностей.

Материалы и методы. В ходе научных экспедиций для изучения морфо-экологических особенностей были выбраны как площадки длительного мониторинга, так и точки периодических отловов. Животные были пойманы с использованием живоловушек методом ловушко-линий, который является стандартным методом, широко применяемым в разнообразных биотопах [5, 6]. В нашем случае ловушки были расставлены в количестве от 15–40 штук по одной линии. Каждая ловушка была заполнена приманкой и расставлена в ареале изучаемого биотопа. Они были расставлены в вечернее время и расставлялись на дистанции 5 метров друг от друга по линии. Места для ловушек были выбраны в соответствии с наиболее возможными местами отлова животных. Ловушки проверялись несколько раз за ночь. Обычно данный метод был использован в течение 2–3 дней по каждому исследуемому биотопу. В качестве приманки применялись корочки хлеба, смоченные в подсолнечном масле и семена злаков.

В статье приведены следующие четыре морфологических признака грызунов: длина тела, длина хвоста, длина задней ступни, высота

уха. Для оценки экологических особенностей видов были описаны биотопические предпочтения, проанализирован рацион питания, рассмотрены аспекты размножения.

В ходе полевых работ были пойманы и подвергнуты морфометрическим измерениям, в целом, 93 особи лесных мышей, соответственно, 32 особи *Apodemus uralensis*, 15 особей *Apodemus witherbyi* и 46 особей *Apodemus ponticus.*

Результаты и обсуждение. Результаты проведенных морфометрических измерений были задокументированы и представлены в Таблице 1 с расчетом для каждого параметра средней и ошибки средней и коэффициента вариации, соответственно.

Таблица 1.

Морфометрические показатели трех видов лесных мышей рода *Apodemus* фауны Армении.

Морфологический признак	*Apodemus uralensis* N = 32	*Apodemus witherbyi* N = 15	*Apodemus ponticus* N = 46
Длина тела (ДТ)	88.84 +- 0.81 83-100 5%	94.8+-0.99 87-101 4%	88.13+-0.51 83-95 4%
Длина хвоста (ДХ)	90+-0.98 83-107 6%	101.2+-1.16 90-110 5%	97.4+-0.79 89-105 5%
Длина задней ступни (ДЗС)	20.8+-0.25 19-23 7%	21.67+-0.43 20-23 5%	22.33+-0.15 20-25 7%
Высота уха (ВУ)	15,06+-0.23 14-16 9%	15.2+-0.42 14-17 6%	16.43+-0.13 15-20 10%

Примечание. Для каждого параметра верхняя строка средняя и ошибка среднего, средняя строка размах значений, нижняя – коэффициент вариации.

Интерпретируя и сопоставляя полученные значения первичных морфометрических параметров видов лесных мышей, населяющих территорию Армении, сразу можно заметить четкое обособление представителей *Apodemus ponticus* кавказской мыши как обладающих наиболее длинными ступнями и максимальной высотой уха, что дает возможность более точной диагностики данного вида.

В вопросе длины хвоста, оценивая значения данной характеристики по видам, стало возможным указывать, как достаточно четкий определительный признак, относительную длину хвоста представителей вида *Apodemus witherbyi*, отличающий их от представителей других видов. У *Apodemus witherbyi* относительная длина хвоста оказалась больше длины тела. Длина хвоста двух других видов – *Apodemus uralensis* и *Apodemus ponticus* соизмерима с длиной тела.

Что касается окраски меха, то она имеет тенденцию к сильной вариации – в зависимости от местности заселения лесных мышей. Цветовой диапазон варьируется от ярких тонов до светло-бурых или до темно-бурых окрасов. Наблюдается корреляция окраски – в зависимости от типа ландшафтной зоны, также от типов насаждений, эскпозиции склонов и кормов.

Необходимо отметить, что наличие и форма горлового пятна лесных мышей рода *Apodemus* может иметь весомый дифференциальный характер. Горловое пятно встречалось в различной конфигурации, к примеру, эллипс, мазок, неправильный круг, следы. Наличие его, в той или иной форме, было отмечено у двух видов мышей: *Apodemus witherbyi* и *Apodemus ponticus*, в отличие от вида *Apodemus uralensis*, у которого мы зарегистрировали полное отсутствие горлового пятна. Окраска горлового (грудного) пятна может варьировать от бело-оранжевого до ярко желтого – в зависимости от времени года и места поимки.

Описание экологических особенностей представителей лесных мышей рода *Apodemus* начнем с описания биотопических предпочтений этих грызунов в условиях различных климатических зон, почвен-

ных покровов и растительности. Для наблюдений и отлова лесных мышей были определены следующие типы биотопов: степи, заросли кустарников, сельско-хозяйственные поля, луга, леса и лесополосы.

Представители *Apodemus uralensis* были пойманы нами практически во всех типах биотопов, что указывает об эврибионтности данного вида в фауне Армении. Этот вид обладает высокой экологической пластичностью, населяет преимущественно лесные биотопы и заросли кустарников. Является характерным обитателем широколиственных и смешанных лесов и избегает затененных биотопов, предпочитая вырубки, кустарниковые заросли.

Лесные мыши вида *Apodemus witherbyi* населяют преимущественно степи, леса и лесополосы. В отличие от вышеуказанной малой лесной мыши, этот вид грызунов выбирает относительно крупные зрелые лесополосы (к примеру, марзы (области) Лори и Тавуш). Является эвритопным таксоном в силу района распространения. В ходе наблюдений была выявлена характерная сезонная миграция данных грызунов, в связи с истощением кормовой базы в определенные времена года.

Apodemus ponticus – кавказская лесная мышь, является характерным обитателем смешанных лесов, предпочитает кустарниковые заросли, иногда селится и в горах. Может поселяться в жилых и хозяйственных постройках, что, конечно, бывает характерно в зимнее время. Считается, что представители данного вида лесных мышей специфично приспособлены к обитанию в древесно-кустарниковых биотопах и затененных лесных массивах, тем самым, представляясь выраженным стенобионтом.

Кормовой базой для лесных мышей служат, преимущественно, семена. Также в основе их рациона могут быть вегетативные и генеративные части растений, грибы, животная пища. Если говорить о предпочтениях в составе рациона питания представителей различных видов лесных мышей, в большей или меньшей степени, заметно преобладание зерновых, и так можно составить следующую очередность: *Apodemus ponticus* – наиболее зерноядный вид, затем идет *Apodemus uralensis*, после *Apodemus witherbyi*. Предпочтения отдаются сначала

крупным семенам таких деревьев, как дуб, абрикос, яблони и груши и др. В качестве животной пищи следует отметить клопов, прямокрылых, личинки жуков и бабочек.

В качестве растительной пищи могут быть вегетативные и генеративные части растений. Растительная пища в рационе лесных мышей обеспечивает данных грызунов углеводами, минеральными веществами и др.

Рацион питания лесных мышей выделяется своей сезонностью, значительно изменяющийся в условиях смен времен года. В целом, каждый вид имеет характерную сезонную динамику рациона, что бывает связано с их биотопическими предпочтениями. Так, *Apodemus ponticus* зарекомендовал себя в качестве преимущественно семеноеда, в противоположность *Apodemus witherbyi*, которая переходит на потребление растительной пищи весной и на повышение присутствия животного корма осенью.

Размножение лесных мышей имеет такие особенности, как сезонность, величина выводка и количество генераций в год. В течение наших наблюдений была выявлена тенденция к началу периода размножения *Apodemus uralensis* в марте, продолжающаяся до октября. Размножение *Apodemus witherbyi* начиналось в феврале и продолжалось вплоть до декабря месяца. Напротив, представители вида *Apodemus ponticus* отличаются относительно короткой продолжительностью периода размножения, примерно, с конца марта – начала апреля и до начала октября. Беременность протекает в среднем от 22 до 25 дней. Размер выводка, как правило, от 4 до 8 детенышей, в зависимости от конкретного вида лесных мышей. Наименьший показатель количества детенышей был зарегистрирован у представителей *Apodemus ponticus*. Детеныши первого помета могут приступить к размножению в том же году. Половозрелости представители всех видов лесных мышей достигают в возрасте 45–55 дней.

Заключение. Исходя из полученных данных, стало возможным сделать следующие выводы. Самым мелким видом лесных мышей фауны Армении является *Apodemus uralensis* – малая лесная (уральская)

мышь. Вид характеризуется отличительно низкими ушами и короткими ступнями. Следующая, *Apodemus ponticus* – кавказская мышь, по размерам незначительно превосходит представителей малой лесной мыши, отличаясь длиной хвоста, однако выделяясь максимальным значением длины задней ступни. *Apodemus witherbyi* – степная мышь по длине тела крупнее двух предыдущих видов лесных мышей, выделяясь максимальным значением длины хвоста, в среднем, среди всех трех видов.

Биотоп со степной растительностью заселен видом *Apodemus witherbyi*, лесные биотопы для *Apodemus ponticus*, и, соответственно, лесополосы, леса и заросли кустарников характерны для обитания *Apodemus uralensis*. Для представителей всех видов лесных мышей характерно заготавливание запасов в норах. Сезон размножения этих грызунов начинается с февраля и может продлится вплоть до декабря.

ЛИТЕРАТУРА

1. *Папов Г.Ю.* Эколого-фаунистические исследования и высотное распространение некоторых мелких млекопитающих Армении. Ер., 2003.
2. *Suzuki, H., Filippucci, M.G., Chelomina, G.N., Sato, J.J., Serizawa, K. and Nevo, E.* 2008. A biogeographic view of *Apodemus* in Asia and Europe inferred from nuclear and mitochondrial gene sequences. Biochemical Genetics, 46 (5–6). P. 329.
3. *Hayrapetyan, T., Aslanyan, A., Papov, G.Y. and Ghazaryan, A.* 2014. New data on small mammals (Insectivora, Chiroptera, Rodents) in southern part of Armenia. *Chemistry and Biology*, (2). PP. 43–47.
4. *Balasanyan, V., Yavruyan, E., Somerová, B., Abramjan, A., Landova, E., Munclinger, P. and Frynta, D.* 2018. High diversity of mtDNA haplotypes confirms syntopic occurrence of two field mouse species *Apodemus uralensis* and *A. witherbyi* (Muridae: *Apodemus*) in Armenia. Russian Journa lof Genetics, 54 (6). PP. 687–697.
5. *Шнитников В.Н.* Постановка работ по изучению экологии млекопитающих // Краеведение. 1929. Т. 6, Вып. 4. СС. 193–220.
6. *Калабухов Н.И., Раевский В.В.* Методика изучения некоторых вопросов экологии мышевидных грызунов // Вести, микробиологии, эпидемиологии и паразитологии. 1933. Т. 12. Вып. 1.

MORPHO-ECOLOGICAL FEATURES OF WOOD MICE (MURIDAE: *APODEMUS*) OF THE FAUNA OF ARMENIA

V. Azaryan

ABSTRACT

The morphologicale valuation of woodmice (Muridae: *Apodemus*) is a method of primary characterization and determination of species, mainly during field work. There is a strong species and geographical variability of *Apodemus* species of the fauna of Armenia. This article describes the ecological features and analyzes the morphometric markers of the three species of wood mice inhabiting the territory of the Republic of Armenia.

Keywords: morphology, ecology, *Apodemus*, fauna, Armenia.

СВЕДЕНИЯ ОБ АВТОРАХ

Агаян А.А.	студент четвертого курса по специальности «Радиофизика и электроника», инженер в ЗАО «Синопсис Армения»
Азарян В.Б.	ассистент кафедры медицинской биохимии и биотехнологии РАУ
Антонян С.В.	студент четвертого курса факультета радиотехники и систем связи НПУА
Берберян А.Х.	к.ф.-м.н., научный сотрудник Института механики НАН РА
Варданян А.В.	студент второго курса магистратуры по специальности «Микроэлектронные схемы и системы» НПУА, инженер в ЗАО «Синопсис Армения»
Галоян Г.	студент второго курса магистратуры по специальности «Приборостроение» НПУА
Галстян Г.В.	студент второго курса магистратуры факультета информатики и прикладной математики ЕГУ
Гараков В.Б.	к.ф.-м.н., старший научный сотрудник Института механики НАН РА
Григорян А.Т.	студент первого курса магистратуры по специальности «Микроэлектронные схемы и системы» НПУА, инженер в ЗАО «Синопсис Армения»
Григорян М.Т.	студент первого курса магистратуры по специальности «Микроэлектронные схемы и системы» НПУА, инженер в ЗАО «Синопсис Армения»
Григорян М.Т.	студент второго курса магистратуры по специальности «Микроэлектронные схемы и системы» НПУА, инженер в ЗАО «Синопсис Армения»
Гукасян С. А.	студент второго курса магистратуры по специальности «Микроэлектронные схемы и системы» НПУА, инженер в ЗАО «Синопсис Армения»
Давидов С.С.	к.ф.-м.н., доцент кафедры алгебры и геометрии ЕГУ

Даллакян Г.	к.ф.-м.н., доцент кафедры математики и математического моделирования РАУ
Димитру Д.	доцент, университет им. Спиру Харета, Бухарест
Киракосян А.Г.	студент первого курса магистратуры по специальности «Микроэлектронные схемы и системы» НПУА, инженер в ЗАО «Синопсис Армения»
Костанян А.Г.	студент второго курса магистратуры по специальности «Микроэлектронные схемы и системы» НПУА, инженер в ЗАО «Синопсис Армения»
Манукян Д.А.	студент четвертого курса по специальности «Радиофизика и электроника», инженер в ЗАО «Синопсис Армения»
Маргарян А.В.	студент магистратуры второго курса по специальности «Радиофизика и электроника» ЕГУ, инженер в ЗАО «Синопсис Армения»
Мовсисян Л.Р.	к.т.н., доцент кафедры радиоустройств НПУА
Мхитарян А.Х.	к.т.н., менеджер в ЗАО «Синопсис Армения»
Оганнисян В.Д.	студент третьего курса факультета энергетики и электротехники НПУА, инженер в “Aragats” LTD
Степанян А.Г.	студент четвертого курса Института информационных и телекоммуникационных технологий НПУА
Хачатрян Г.А.	к.ф.-м.н., сотрудник лаборатории YerevaNN факультета информатики и прикладной математики ЕГУ
Цатурян Г.А.	студент четвертого курса факультета радиотехники и систем связи НПУА
Шахназарян Д.А.	аспирант второго года обучения по специальности «Алгебра и теория чисел ЕГУ

СОДЕРЖАНИЕ

Главный редактор РНИ – *М.Э. Авакян*
Корректор – *Н.И. Маргарян*
Компьютерная верстка – *А.Г. Антонян*

Адрес Редакции научных изданий
Российско-Армянского
университета:

0051, г. Ереван, ул. Овсепа Эмина, 123
тел./факс: (+374 10) 27-70-52 (внутр. 42-02)
e-mail: redaction.rau@gmail.com

Заказ № 17
Подписано к печати 20.05.2020г.
Формат 70x100$^{1}/_{16}$. Бумага офсетная № 1.
Объем 7.25 усл. п.л. Тираж 100 экз.